Physics Reports 1000 (2023) 1–57

Contents lists available at ScienceDirect

Physics Reports

journal homepage: www.elsevier.com/locate/physrep

Coherence resonance in neural networks: Theory and experiments

Alexander N. Pisarchik [a,*], Alexander E. Hramov [b,c,d]

[a] Center for Biomedical Technology, Universidad Politécnica de Madrid, Campus Montegancedo, 28223 Pozuelo de Alarcón, Spain
[b] Baltic Center for Neurotechnology and Artificial Intelligence, Immanuel Kant Baltic Federal University, A. Nevskogo Str. 14, 236016 Kaliningrad, Russia
[c] Research Institute of Neuroscience, Samara State Medical University, Gagarina Str. 18, 443079 Samara, Russia
[d] Engineering School of Information Technologies, Telecommunications and Control Systems, Ural Federal University, Mira Str. 19, 620002 Ekaterinburg, Russia

ARTICLE INFO

Article history:
Received 7 November 2022
Accepted 29 November 2022
Available online xxxx
Editor: Itamar Procaccia

Keywords:
Brain
Brain–computer interface (BCI)
Chimeras
Coherence
Complex networks
Dynamical systems
Electroencephalogram (EEG)
Magnetoencephalogram (MEG)
Mathematical models
Neural models
Neural networks
Noise
Nonlinear dynamics
Perception
Psychometric function
Stochastic dynamics

ABSTRACT

The paper is devoted to the review of the coherence resonance phenomenon in excitable neural networks. In particular, we explain how coherence can be measured and how noise affects neural activity. According to our research, intrinsic brain noise, which affects neural activity at the microscopic level, has a positive effect at the macroscopic level related to brain connectivity. Namely, it coordinates responses of different brain areas and forces their interaction to efficiently process sensory information. We find that brain noise can be altered as a result of attention and cognitive training to optimize the efficiency of information processing. Numerous experimental and theoretical studies provide substantial evidence for beneficial effects of internal brain noise on cognitive performance. Furthermore, coherence resonance in the brain response to a cognitive task not only increases neural activity in certain brain areas, but also provides pathways for neural communication between distant brain areas. In addition, the study of coherent resonance allows finding optimal parameters for better performance and efficient control of brain–computer interfaces.

Contents

---

[*] Corresponding author.
E-mail address: alexander.pisarchik@ctb.upm.es (A.N. Pisarchik).

https://doi.org/10.1016/j.physrep.2022.11.004
0370-1573/

---

1. Introduction

The emergence of order from irregular motion is one of the greatest mysteries of the universe. In his famous book "Order Out of Chaos" the Belgium–Russian physical chemist, Nobel-Prize winner Ilya Prigogine argued that dynamical systems far from equilibrium, with high energy consumption, can exhibit a high degree of order [1]. However, since all of his thinking was mostly philosophical and mathematical, some scholars have criticized his view on the order formation, stating that such evolution is the result of manipulation on paper or on a computer, but in real life it does not exist. Since the end of the 20th century, the study of the mechanisms underlying the formation of order from noise and chaos has been an important task for researchers in various fields of science, because knowledge of these mechanisms can help us understand the principles of self-organization of matter.

Generally, adding noise to a system makes its dynamics more unpredictable. However, in some cases, the order resonates with the noise level. This means that there is a certain noise intensity at which the motion is most coherent. Such a phenomenon, known as *coherence resonance* (CR), was discovered in stochastic systems where regularity (or coherence) maximizes at a certain value of the noise intensity noise near a saddle–node bifurcation on the invariant circle [2] or near a supercritical Andronov–Hopf bifurcation [3]. Some scientists [4] call this phenomenon *stochastic coherence* (SR) [5]. It should be noted that SR is a particular case of CR in periodically driven systems, which occurs either in bistable [6] or excitable systems near the excitation threshold [3,7,8]. The appearance of CR and SR is illustrated in Fig. 1.

Both CR and SR are observed in the presence of additive external or/and internal noise of a certain intensity, which enhances the coherence (or order) of the output signal of the analyzed system. The coherence (or regularity) measure is characterized by a typical function with a maximum observed at a certain (optimal) noise intensity.

Coherence resonance is a common phenomenon in many natural systems. It was originally discovered in the excitable FitzHugh–Nagumo neuron model [3], where the resonance-like behavior occurs in the degree of regularity (or measure of

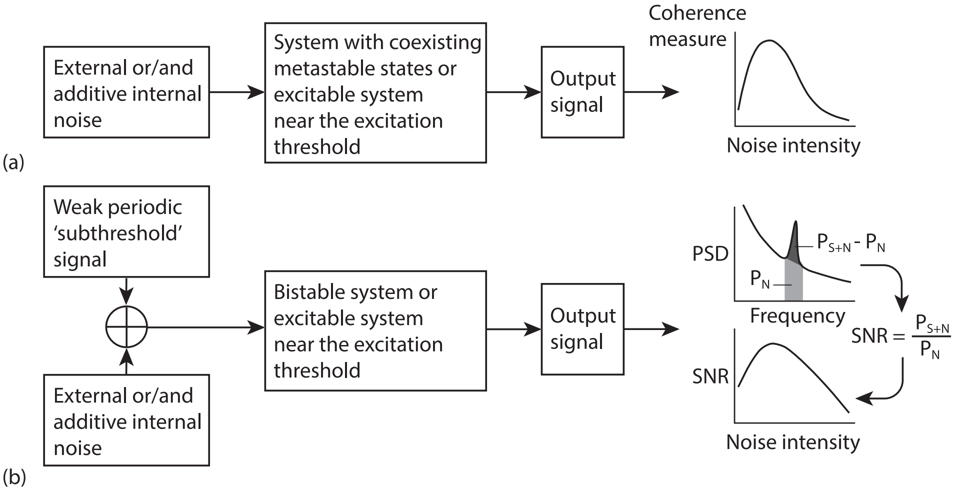

Fig. 1. (a) Coherence resonance is a measure of the coherence of a noisy dynamical system, which maximizes at a certain level of additive external or/and internal noise. (b) Stochastic resonance is observed when a weak subthreshold periodic external signal is assumed to be the input to a bistable or excitable dynamical system such that its presence cannot be ascertained from the system's response in the absence of noise. Stochastic resonance allows us to detect statistically the weak input periodic signal with quality measured by the output signal-to-noise ratio (SNR), based on the spectral composition (power spectral density (PSD)) of the system output signal. SNR is defined as the power difference between the noisy signal (P_{S+N}) and noise itself (P_N) (in dB) or as the ratio of the signal and noise amplitudes (in absolute values), which exhibits a maximum as the noise intensity is varied.

coherence) of noise-induced oscillations, which leads to an optimal response in terms of regularity of excited oscillations for a certain noise power. The resonance effect appears because noise induces a new time scale in spiking dynamics when the noise intensity exceeds the activation threshold. On the other hand, noise has no effect on the deviation of the time excursion. Therefore, there exists an optimal noise intensity at which the spikes appear more regular. CR depends on the nature of noise and reveals in the inter-event or interspike intervals of the time series or the characteristic correlation time to resonance scale. CR has a large characteristic correlation time, and peaks in the time series exhibit strong synchronization.

It should be noted that some neurophysiologists use the term "stochastic resonance" instead of "coherent resonance" when studying brain dynamics or human behavior. We recall that SR implies the existence of a periodic signal in a noisy bistable or an excitable system, as distinct form CR which does not requires any periodic signal. The enhanced coherence of the output signal can be measured with SNR calculated from the power spectral density of the system output. Typically, the dependence of SNR on the noise intensity exhibits a single peak (see Fig. 1(b)). However, many experiments with living organisms and especially with humans in processing sensory information do not assume the presence of any external periodic signal.

As distinct from conventional CR, SR is observed in a bistable or excitable system in the presence of a periodic signal. The mechanism of SR is quite simple and can be illustrated with the following example. Consider the motion of a particle in a symmetric bistable potential well $U(x)$ under the influence of a weak periodic signal. The amplitude of this 'subthreshold' periodic signal is small enough to exclude the particle's crossing of the barrier in the absence of noise. Such a system has two time scales due to both the particle wandering in the vicinity of one of the equilibrium states (intrinsic dynamics) and transitions from one well to another (global dynamics). The latter time scale is know as the activated time T_K required for the phase trajectory to escape from one stable equilibrium to another. In the case of white noise and parabolic potential wells, the activation time obeys the Arrhenius law depending on noise intensity, i.e., $T_K \propto \exp(\varDelta/D^2)$, where $\varDelta$ is the potential barrier depth, and D is the noise amplitude. In the presence of a periodic signal, the potential barrier is periodically modulated and the transition probability between them will also become a periodic function, and the output signals will contain a periodic component. The latter will be registered in the power spectrum as a peak at the modulation frequency and its odd harmonics (in the case of a symmetric potential). In the case of fixed parameters of system and an external periodic signal, the activation time according to the Arrhenius law will depend only on the noise intensity. For small noise $D^2 \ll \varDelta$, the transition time is very large and significantly exceeds the period of the external modulation signal. At high noise intensity $D^2 \gg \varDelta$ during the period of modulation, the system will make with high probability several global transitions. By varying the noise intensity, it is possible to provide a regime in which the average transition time through the barrier will be close to the modulation period of the signal. SR is usually identified as the maximum of the signal-to-noise ratio (SNR) dependence on the noise intensity.

Thus, by varying the noise level it is possible to tune the stochastic bistable system to the mode of maximum amplification of the modulation signal and SNR. Numerous theoretical and experimental studies evidenced the phenomenon of SR in different models and real-life systems. A weak 'subthreshold' periodic signal entered to a nonlinear dynamical system cannot be inferred from the system response in the absence of additive noise (see Fig. 1(b)). The existence of SR allows to detect the input periodic signal by measuring the SNR from the power spectral density (PSD) of the output signal, which exhibits a peak (P_{S+N}) in the background noise (P_N), as illustrated in Fig. 1(b). Typically, the SNR has a single maximum as the noise intensity changes within certain limits. Further in this review, we will not describe classical SR, since it has been covered in many review papers (see, e.g., [9–13]).

Unlike SR, which assumes the presence of a periodic signal, CR takes place in autonomous excitable systems, i.e., under purely noise excitation or under the influence of endogenous noise without any periodic driving signal. A comprehensive review of noise effects in excitable systems was published in 2004 [14]. Since then, many new interesting experimental and theoretical results have been obtained, in particular, in neural networks. CR was extensively studied in different networks formed by coupled neural oscillators, such as Rulkov maps [7], integrate-and-fire [15,16], Izhikevich [17], FitzHugh–Nagumo [4,18–25], Morris–Lecar [26–29], Hindmarsh–Rose [16], and Hodgkin–Huxley [8,30–37] models, and evidenced experimentally in cultures of dissociated neuronal cells [38] and distributed cortical neural network during sensory information processing [8]. CR was observed in neural networks of different topology, including globally coupled [7,8,16,24,38–40], locally coupled [24], randomly connected [17,41], small-world [42,43], scale-free [33], Newman–Watts [34], ring [21,23,44], multiplex networks [23,25,45], as well as influencer networks of phase oscillators [46]. It was also found that CR is robust to average network degree [33].

On the other hand, there are many papers devoted to CR in non-excitable networks. In particular, a similar resonance behavior was observed in multistable systems. The underlying mechanism of the former type of CR is associated with subcritical and supercritical Hopf bifurcations [47] and time-delayed feedback [48–50], as well as with a saddle–node bifurcation of a pair of (stable and unstable) periodic orbits [51]. The fundamental aspects of this phenomenon were studied in detail by Zakharova et al. [52].

In addition to neural models, CR was found in electrochemical system [53], optical systems [54,55] including lasers [47,54–59], energy harvesting system [60,61], financial market [62,63], microwave device [64], semiconductors [65,66], electronic circuits [27,67–70], thermoacoustics [71], plasma [72], chemical reactions [73–76], electrochemical system [77], optically trapped atoms [78], carbon nanotubes [79], and acoustic energy harvester [80]. It should be noted that sometimes an opposite resonant effect occurs, i.e., coherence minimizes at a certain noise level. Such so-called *anticoherence resonance* was observed in excitable systems with time-delayed feedback or under positive feedback [24,25,62,81–83].

There are a huge number of papers related to the study of CR. Therefore, in this paper we will restrict our consideration to the most important, in our opinion, achievements on the study of CR in excitable neural networks. The rest of the paper is organized as follows. In Section 2 we describe the most popular measures of CR. Then, in Section 3 we consider some neural network models where CR was detected. In Section 4 we review the most important results on CR in spatially distributed neural networks. In Section 5 we focus on experimental approaches to brain noise estimation in the context of CR observation in brain cortical networks. Special attention is given to controlling CR in the brain neural network and brain–computer interfaces, which we describe in Section 6. Finally, the review is summarized in Section 7.

2. Popular coherence measures

Let us start our consideration with the most popular measures of the coherence in excitable and multistable systems. For quantitative estimation of the coherence, the following characteristics of the system dynamics can be used:

- normalized autocorrelation function,
- correlation time,
- normalized standard deviation (NSD) of peak or spike amplitude (amplitude coherence),
- NSD of interpeak or interspike interval (ISI) (Fano-factor) (time coherence),
- probability distribution of ISI,
- dominant spectral component (spectral coherence),
- signal-to-noise ratio (SNR) determined from a power spectrum,
- similarity function.

The above measures can be used to characterize coherence in both solitary systems and complex networks. In addition, there are also measures that are applied to complex networks only. They are

- entropy,
- statistical complexity,
- connectivity (topological coherence),
- Kuramoto order parameters,
- strength of incoherence,
- χ^2-parameter,
- adaptive coherence measure,
- linear spatial cross-correlation (spatiotemporal coherence),
- structure function (spatial coherence),
- effective diffusion coefficient (see Fig. 2).

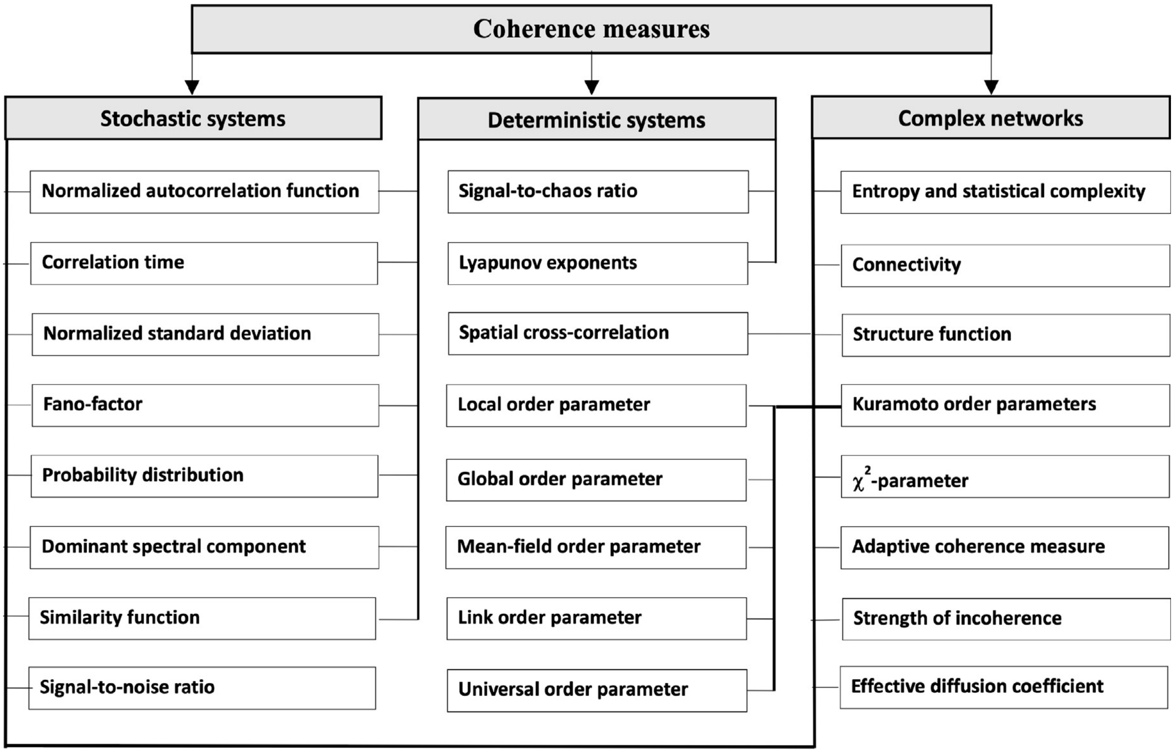

Fig. 2. Coherence measures in solitary stochastic systems, chaotic systems, and complex networks.

Furthermore, the following two measures are used to characterize deterministic coherence resonance in chaotic systems only:

- signal-to-chaos ratio (SCR),
- Lyapunov exponents.

All coherence measures are systematized in Fig. 2. The existence of a maximum in the dependence of one of these quantities on the noise intensity indicates the presence of CR, and a minimum indicates the presence of anticoherence resonance. We do not exclude the use in the future other values to measure the coherence.

Consider now how the coherence measures are determined.

2.1. Normalized autocorrelation function

The normalized autocorrelation function is defined as

$$C(\tau)=\frac{\left\langle\tilde{x}(t)\tilde{x}(t+\tau)\right\rangle}{\left\langle\tilde{x}^2\right\rangle}, \tag{1}$$

where x is a measurable system variable, $\langle x\rangle$ is its time average, $\tilde{x}=x-\langle x\rangle$, and τ is a time lag.

The higher $C(\tau)$, the better the coherence.

2.2. Correlation time

The characteristic correlation time is defined as

$$\tau_c=\int_{t_0}^{t_{max}} C^2(t)dt, \tag{2}$$

where t_0 is the duration of transient processes, and t_{max} is the duration of the time series.

The larger τ_c, the better the coherence. The presence of a maximum in the dependence of C or τ_c on the noise intensity means the existence of CR.

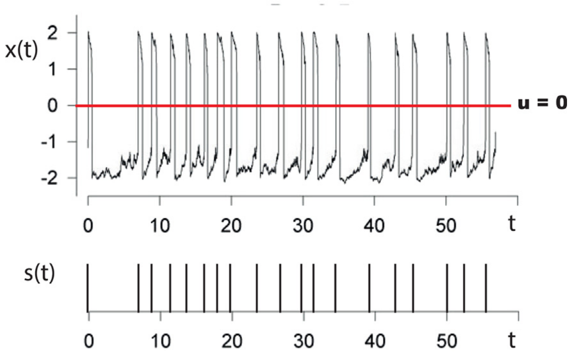

Fig. 3. Time series of the FitzHugh–Nagumo model Eq. (60) driven by noise with parameters $a = 1$, $\varepsilon = 10^{-3}$, and noise amplitude $D = 0.5$. To identify spike times T_m, the threshold value $u = 0$ is introduced (red horizontal line), and spike time is recognized whenever $x(t)$ variable crosses the threshold value $u = 0$ from below. As a result, we construct the δ-like spike sequence $s(t)$ given by Eq. (51).

2.3. Amplitude coherence

Amplitude coherence is measured as standard deviation σ_A of peak amplitude A_p normalized to average amplitude $\langle A_p \rangle$. For a network of oscillators, this value is defined as

$$R_A = \frac{\sigma_A}{\langle \bar{A_p} \rangle}, \quad \sigma_A = \sqrt{\langle \bar{A_p^2} \rangle - \langle \bar{A_p} \rangle^2}, \tag{3}$$

where the overbar indicates the mean value over the nodes.

The amplitude CR occurs when R_a has a minimum with respect to the noise intensity. The inverse value R_A^{-1} reflects the regularity of the amplitude variation.

2.4. Time coherence (Fano-factor)

Similarly, time coherence is defined as standard deviation σ_T of interpeak intervals t_p normalized to the average interpeak interval $\langle t_p \rangle$. This value known as "jitter" is defined as follows

$$R_T = \frac{\sigma_T}{\langle \bar{t_p} \rangle}, \quad \sigma_T = \sqrt{\langle \bar{t_p^2} \rangle - \langle \bar{t_p} \rangle^2}. \tag{4}$$

When jitter R_T reaches its minimum value with respect to the noise amplitude, we are dealing with coherence resonance. The inverse value R_T^{-1} characterizes the regularity of the oscillation phase.

In the case of spiking neurons, time coherence is often characterized by *Fano-factor* defined as standard deviation of the interspike interval (ISI) normalized to the average ISI [84]:

$$\eta = \frac{\sigma}{\langle T \rangle}, \quad \sigma^2 = \Big\langle \Delta T_m - \langle \Delta T \rangle \Big\rangle^2, \tag{5}$$

where $\Delta T_m = T_{m+1} - T_m$ $(m = 1, \ldots, M)$ is the interspike interval (ISI), $\langle T \rangle = T_l / M$ (T_l and M being the length of the spike train and the cluster size, respectively) is the average ISI, and $\eta = 1$ corresponds to Poisson processes.

Since a typical neuron does not have a hard threshold, we artificially identify a spike as being emitted whenever some variable characterizing the neuron's dynamics crosses the threshold value u for confidence from below. Thus, we ignore all subthreshold oscillations. Fig. 3 illustrates this approach for the FitzHugh–Nagumo neuron model (see Section 3.1 for details).

The definition given by Eq. (5) is limited to a single neuron. For a neuronal network, the normalized standard deviation of the average ISI can be evaluated as follows [21]

$$R = \frac{\sqrt{\overline{\langle \Delta T^2 \rangle} - \overline{\langle \Delta T \rangle^2}}}{\overline{\langle \Delta T \rangle}}, \tag{6}$$

where the overbar $\overline{\langle \cdot \rangle}$ indicates the additional average over all network nodes.

In several papers [18,57,74,85–87], a decrease in the Fano-factor are attributed to increasing coherence, meaning that all intervals are distributed in a narrower region towards the average value, and CR is characterized by a pronounced minimum in the dependence of η (for a single neuron) or R (for a neuronal network) on the noise intensity. However, as was shown in other papers [84,88], the Fano-factor is not a sufficient criterion for increasing coherence. Therefore, we recommend using not one, but several different coherence measures when studying dynamics of stochastic systems.

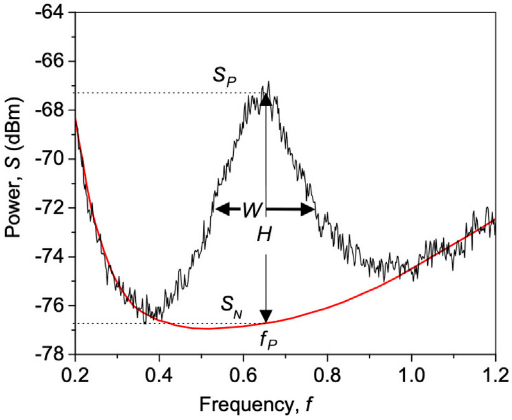

Fig. 4. Determining the degree of coherence from the power spectrum in a stochastic or a chaotic system.

2.5. Probability distribution

The coherence of an oscillatory system over different time scales can be measured by analyzing the probability distribution. For example, in the case of bursting or spiking neurons, interspike or interburst intervals are distributed in different time intervals. The half-width at half-height (HWHH) of each distribution can provide information about the system coherence in the corresponding time scale.

For a network of oscillators, the sharpness of the distribution characterizes temporal coherence measured as [89]

$$R_e = \frac{T_e}{\sigma_T} \int_{(1-\alpha)T_e}^{(1+\alpha)T_e} P(\bar{t_p}) d\bar{t_p}, \tag{7}$$

where $P(\bar{t_p})$ is the probability density of interpeak intervals $\bar{t_p}$.

In bistable systems, the residence time distribution and the first excursion probability serves as a measure of coherence. The probability of time periods the system spends in the vicinity of one of the metastable states is the indicator of stability and quality of the system coherence.

2.6. Degree of coherence

The degree of coherence is determined from the power spectrum as a signal-to-noise ratio (SNR). Although SNR is typically used to evaluate stochastic resonance in periodically forced systems, this value is also applied to quantitatively characterize the coherence of stochastic and chaotic systems in the absence of external modulation. SNR is derived as the ratio of dominant spectral component S_P to spectral intensity S_N of background noise at dominant frequency f_P:

$$\mathrm{SNR} = \frac{2S_P}{S_N(f_P)}, \quad S_P = \lim_{\Delta f \to 0} \int_{f_P-\Delta f}^{f_P+\Delta f} S(f) df. \tag{8}$$

The factor of 2 appears because of power spectral density symmetry $S(f) = S(-f)$.

If the power spectrum is calculated in a semilog scale (in dBm), the SNR measured in dBm is defined as the peak height H, i.e., the difference between spectral powers S_P and S_N (see Fig. 4):

$$H(\mathrm{dBm}) = S_P - S_N. \tag{9}$$

The degree of coherence β is determined as the product of the peak height H to its quality factor Q as [2]

$$\beta = HQ, \quad Q = f_P/W, \tag{10}$$

where W is the full-width at half-height measured with respect to S_N.

Assuming the following scaling laws for W and H with respect to noise intensity D [90]:

$$W \propto W_0 + D, \quad H \propto 1 - \mathrm{e}^{-\alpha D}, \tag{11}$$

with W_0 and α being constants, we obtain that the degree of coherence β obeys the following scaling relation

$$\beta \propto \frac{1 - \exp(-\alpha D)}{W_0 + D}. \tag{12}$$

One can see from Eq. (12) that there is the optimal noise intensity at which β has a maximum value.

2.7. Signal-to-chaos ratio

Similar to the SNR in stochastic systems, signal-to-chaos ratio (SCR) is used to characterize deterministic coherence resonance in chaotic systems. Namely, the SCR is defined as the ratio of the spectral component S_P at the dominant frequency f_P to the full-width at half-height W:

$$\mathrm{SCR} = \frac{S_P}{W}. \tag{13}$$

The higher the SCR, the stronger the coherence.

2.8. Spectral coherence

In a network of N coupled oscillators, the total spectral power S_T of all oscillators at the dominant frequency f_P is higher when the network is synchronized. Therefore, S_T can serve as a measure of the network spectral coherence:

$$S_T = \sum_{i=1}^{N} S_i(f_P), \quad i = 1, 2, \ldots, N. \tag{14}$$

2.9. Similarity function

The coherence of a system of coupled oscillators is related to their synchronization [91], which can be characterized by a similarity function. The similarity function $\mathcal{S}_{ij}$ of x_i and x_j variables of i and j oscillators can be calculated as

$$\mathcal{S}_{ij}^2(\tau) = \frac{\left\langle \left[x_j(t) - x_i(t+\tau)\right]^2 \right\rangle}{\sqrt{\langle x_j(t)^2\rangle \langle x_i(t)^2\rangle}}, \tag{15}$$

where τ is the time lag between state vectors of the corresponding oscillators. The similarity function of a network of N coupled oscillators can be calculated as

$$\mathcal{S}(\tau) = \sum_{i\in N}\sum_{j\in N} \mathcal{S}_{ij}(\tau), \;\; i \neq j. \tag{16}$$

The value of the minimum of the similarity function $\delta = \min_\tau \mathcal{S}(\tau)$ is related to lag synchronization. The presence of extrema in the dependence of δ on the control parameter means that coherence or anticoherence resonance occurs in the system.

The lower the minimum of the similarity function, the higher the coherence.

2.10. Entropy

Since entropy is a measure of network uncertainty or heterogeneity, it can obviously be used to quantify coherence. In other words, the entropy measures the diversity of link distribution $\mathbf{q} = (q(1), \ldots, q(i), \ldots, q(N))$. There are different types of entropy. One of them is the Shannon entropy which for complex networks is defined as [92]

$$H(\mathbf{q}) = -\sum_{k=1}^{N} q(k) \ln(q(k)), \tag{17}$$

where $q(k)$ is the remaining degree, i.e., the number of links leaving the node, given by

$$q(k) = \frac{(k+1)P_{k+1}}{\langle k\rangle} \tag{18}$$

where P_k is the degree distribution, i.e., the probability of having a node with k links, and $\langle k\rangle = \sum_k kP_k$ is the mean degree.

For the majority of complex networks, the degree distribution obeys the following scaling relation

$$P_k \sim k^{-\gamma} f(k/\xi) \tag{19}$$

with scaling exponent γ and function $f(k/\xi)$ which introduces a sharp cutoff at characteristic scale $\xi < k$.

However, the above definition of the Shannon entropy does not take into account the network topology. Therefore, this definition was extended to so-called *topological Shannon entropy*, which for the case of a simple undirected network is derived as [93]

$$H = -\sum_{i<j}^{N} p_{ij} \ln p_{ij}, \tag{20}$$

where p_{ij} is the probability of connection between i and j nodes.

2.11. Statistical complexity

Statistical complexity is related to the distance to the uniform distribution P_e, and hence it can serve as a measure of the network coherence. First, we calculate the probability distribution $P = \{p_j; j = 1, \dots, M\}$ with M being the number of possible states of the network. Then, we compute the Shannon information measure $S[P] = -\sum_{j=1}^{M} p_j \ln(p_j)$ and maximum permutation entropy $S_{max} = H[P_e] = \ln M$ for the uniform probability distribution $P_e = (1/M, \dots, 1/M)$. After that, we obtain the statistical complexity measure as [94]

$$\mathfrak{C}[P] = \overline{H}[P]\, Q_J[P], \tag{21}$$

where $\overline{H} = S[P]/S_{max}$ is the normalized Shannon entropy and $Q_J[P, P_e]$ is the disequilibrium derived by

$$Q_J[P] = Q_0\, \mathfrak{J}[P, P_e], \tag{22}$$

with normalization constant

$$Q_0 = -2\left\{\frac{M+1}{M}\ln(M+1) - 2\ln(2M) + \ln M\right\}^{-1}, \tag{23}$$

and Jensen–Shannon divergence $\mathfrak{J}[P, P_e]$ that measures the similarity between two probability distributions (P and P_e), given by

$$\mathfrak{J}[P, P_e] = S[(P + P_e)/2] - \frac{S[P] + S[P_e]}{2}. \tag{24}$$

The higher the statistical complexity, the better the coherence.

So far, this measure was only used to characterize stochastic resonance [94–98], but not coherence resonance.

2.12. Topological coherence

When we are dealing with a complex network, it is important to evaluate its topological coherence, which is determined by the number of links connecting the network nodes. In this context, we assume that the network topology is more consistent when more nodes interact. This is especially attractive when we are dealing with neuronal networks like the human brain. Brain communication is critical to information processing and analysis. At the same time, the number of connections between individual brain areas and their strengths can be determined as the presence of the temporal correlation between time series of electrical/magnetic activity (EEG/MEG signals) or deoxygenated blood levels (BOLD signals) in the brain regions of interest (see Section 4.4).

2.13. Kuramoto order parameters

The Kuramoto order parameter was introduced to measure phase coherence in the network of N Kuramoto oscillators with natural frequencies ω and harmonic coupling, given by

$$\dot{\theta}_j = \omega_j + K\sum_{n=1}^{N} A_{j,n}\sin(\theta_n - \theta_j), \quad j, n = 1, 2, \dots, N, \tag{25}$$

where K is the coupling strength between the oscillators, $A_{n,j} \in \{0, 1\}$ is the adjacency matrix describing which nodes interact with which other nodes, and θ_n is the angle for each phase of the nth element determined as

$$\theta_n(t) = 2\pi\left(m_n + \frac{t - t_{m-1,n}}{t_{m,n} - t_{m-1,n}}\right), \tag{26}$$

where $t_{m,n}$ is the time when the mth spike of the nth element occurs.

In case of all-to-all coupling, the *complex Kuramoto order parameter* $r(t)$ quantifies phase synchronization of a set of oscillators using the difference of phase-space vectors of all N elements [99,100]

$$r(t)e^{i\psi(t)} = \frac{1}{N}\sum_{n=1}^{N} e^{i\theta_n(t)}, \tag{27}$$

where $\psi(t)$ describes the average phase of all oscillators and $r(t)$ reflects the degree of phase coherence.

The phase ordering measure is the long-term average of the *absolute order parameter*

$$r_K^2(t) = \left\langle \left| r(t)e^{i\psi(t)} \right|^2 \right\rangle_t = \left\langle \frac{1}{N^2}\sum_{j,n=1}^{N} e^{i(\theta_j - \theta_n)} \right\rangle_t, \tag{28}$$

which measures the average of the phase difference of all pairs of oscillators. If the oscillators are incoherent, the time average is zero and therefore $r = 0$. When some of the oscillators are partially phase-locked, the cosine of their phase differences becomes positive and does not disappear when averaged over time, and therefore $r > 0$.

It should be noted that the original order parameter given by Eq. (28) cannot be used for characterizing any interaction networks because its calculation requires well defined phases of the network elements. To calculate the order parameter, one has to compare the phases of two oscillators in a network that interact only indirectly through a possibly very long chain of intermediate oscillators.

To study the influence of the network topology on the phase coherence of all neighboring oscillators, several alternative definitions of the order parameter were introduced. One of them is the *local order parameter* for jth oscillator depicted as [101,102]

$$r_j = \left| \sum_{n=1}^{N} A_{j,n} \left\langle e^{i\theta_j} \right\rangle_t \right|. \tag{29}$$

Then, the *global order parameter* is easily defined as the average value of the local order parameters:

$$r_{net} = \frac{\sum_{n=1}^{N} r_n}{\sum_{n=1}^{N} k_n}, \tag{30}$$

where k_n is the degree of node n.

Another definition of the order parameter ignores the specific network topology in favor of representing network ensembles in a mean field to simplify analytical calculations [103,104]. Such a *mean-field order parameter* is calculated by weighting each node with its degree as

$$r_{mf} = \left\langle \left| \frac{\sum_{n=1}^{N} k_n e^{i\theta_n}}{\sum_{n=1}^{N} k_n} \right| \right\rangle_t. \tag{31}$$

This value measures globally averaged phase coherence, but fails to accurately represent the incoherent and partially phase locked state with respect to the actual network topology, especially for small networks.

Finally, to study synchronization analytically in mean-field network models, the *linked order parameter* is derived by restricting the order parameter to the network topology and only averaging over phase differences between directly connected nodes [105]:

$$r_{link} = \frac{1}{\sum_{n=1}^{N} k_n} \sum_{j,n=1}^{N} A_{j,n} \left| \left\langle e^{i(\theta_j - \theta_n)} \right\rangle_t \right|. \tag{32}$$

The above order parameters work well for related purposes, such as the analytical study of synchronization in mean-field network models. However, none of them reflect the entire transition to coherence, especially in smaller networks.

To describe the entire evolution of a complex network from an incoherent state to full synchronization, Schröder et al. [106] proposed the *universal order parameter* defined as

$$r_{uni} = \frac{1}{\sum_{n=1}^{N} k_n} \sum_{j,n=1}^{N} A_{j,n} \left\langle \cos(\theta_j - \theta_n) \right\rangle_t. \tag{33}$$

This parameter takes into account the network topology and consider only the phase difference between neighboring nodes. Unlike r_{link}, r_{uni} reduces to the original Kuramoto order parameter in Eq. (27) for all-to-all connected networks. This value reflects the degree of phase coherence in all synchronization stages.

The main drawback of the Kuramoto order parameters is that their calculations require well defined phases of the network elements. However, sometimes it is very difficult to measure these phases correctly, for example, in networks of spiking and bursting neurons which exhibit fast–slow relaxation dynamics, where phase perturbations are caused by neuronal interactions.

2.14. Strength of incoherence

The strength of incoherence is a statistical measure to characterize the coherence in complex networks of N coupled oscillators, given by [107]

$$\mathfrak{S} = 1 - \frac{1}{N} \sum_{n=1}^{N} \Theta(\delta - \sigma_x), \tag{34}$$

where $\Theta(.)$ is the Heaviside step function, δ is a predefined threshold, i.e., a certain percentage value of difference between the maximum and minimum values of the state variable $(x_n^{max} - x_n^{min})$.

The local standard deviation for every successive n number of oscillations, as

$$\sigma_x = \left\langle \sqrt{\frac{1}{N}\sum_{n=1}^{N}\Big(x_n - \langle x\rangle\Big)^2}\right\rangle_t, \quad \langle x\rangle = \frac{1}{N}\sum_{n=1}^{N} x_n(t). \tag{35}$$

The strength of incoherence takes values $\mathfrak{S} = 1$, $\mathfrak{S} = 0$, or $0 < \mathfrak{S} < 1$ for incoherent, coherent, or chimera states, respectively.

2.15. χ^2-parameter

Another measure of the coherence in a network of N oscillators is the χ^2-parameter defined as [108]

$$\chi^2 = \frac{\sigma_x^2}{\frac{1}{N}\sum_{n=1}^{N}\sigma_{x_n}^2}, \tag{36}$$

where $x_n(t)$ is the time series of nth oscillator in the representative time window. Here, σ_x^2 and $\sigma_{x_n}^2$ are, respectively, variances of average variable $\langle x(t)\rangle = \frac{1}{N}\sum_{n=1}^{N} x_n(t)$ and state variable of the nth oscillator, derived as

$$\sigma_x^2 = \big\langle x^2(t)\big\rangle_t - \big\langle x(t)\big\rangle_t^2, \quad \sigma_{x_n}^2 = \big\langle x_n^2(t)\big\rangle_t - \big\langle x_n(t)\big\rangle_t^2. \tag{37}$$

The χ^2-parameter takes values in [0, 1], $\chi^2 = 0$ corresponds to an asynchronous state, whereas $\chi^2 = 1$ means complete synchronization. For values $0 < \chi^2 < 1$, chimeric states can exist. The advantage of this parameter over the Kuramoto order parameter and the incoherence strength is that there is no need to calculate the phases of the oscillators. Although the χ^2-parameter is fairly easy to compute, it has the disadvantage that it does not allow automatic finding state space regions with distinct dynamical regimes.

A universal order parameter was introduced by Schöder et al. [106] to characterize synchrony in networks of phase oscillators, similar to the Kuramoto order parameter [109]. However, this parameter can also serve as a measure of the network coherence.

2.16. Adaptive coherence measure

To avoid the shortcomings of the above measures, Dogonasheva et al. [110] introduced so-called *adaptive coherence measure* that assumes the identification of coherent states with multiple synchronous clusters firing with time delays. The adaptive coherence measure is based on solving an optimization problem and defined as follows

$$R^2 = \max_{\mathbf{\Delta t}} \chi^2\Big(\Big[x_n(t - \Delta t_n)\Big]_{n=1}^{N}\Big), \tag{38}$$

where $\mathbf{\Delta t} = (\Delta t_1, \Delta t_2, \ldots, \Delta t_L)$ is a vector of the unique time lags.

The direct solution of Eq. (38) involves multivariate optimization that requires significant computational resources. However, there are alternative approaches [110] which simplify the optimization procedure.

2.17. Lyapunov exponents

The order or coherence in chaotic systems is characterized by Lyapunov exponents which reflect the sensitivity of the system to a small change in initial conditions, for instance, in periodic windows the Lyapunov exponents are negative, while in a chaotic regime the largest Lyapunov exponent is positive, while other exponents can be either negative or zero. Some of the exponents can take maximum or minimum values with respect to a control parameter, that indicate on the existence of deterministic coherence and anticoherence coherence resonances.

As an example, Fig. 5 shows the largest Lyapunov exponent of the system of three unidirectionally ring-coupled Rössler oscillators in the parameter space of mismatch Δ between their fundamental frequencies and coupling strength κ [111]. One can see that the largest Lyapunov exponent reaches minimum (up to zero for $\Delta \approx 0.25$) with respect to the coupling strength κ, when the frequency mismatch Δ is fixed. This means that chaos is transformed into a periodic motion for a certain coupling strength ($\kappa \approx 0.3$) and thus the dynamics becomes more coherent.

2.18. Spatiotemporal coherence

The regularity of spatial structures is characterized by linear spatial cross-correlation $\mathbb{S}$ [112,113]. For a 2D lattice of N coupled units, $\mathbb{S}$ is calculated for variable x_{ij}, where the subscript (ij) indicates that the network unit locates on the ith row and the jth column $(i, j = 1, \ldots, N)$, as the space and time average nearest-neighbor distance of all elements, normalized to the total spatial amplitude variance. Thus, $\mathbb{S}$ is defined as

$$\mathbb{S} = \left\langle \frac{\mathrm{Cov}(t)}{\mathrm{Var}(t)}\right\rangle_T, \tag{39}$$

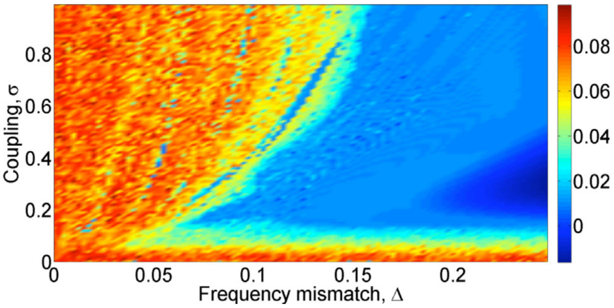

Fig. 5. Largest Lyapunov exponent (right color panel) of three ring-coupled Rössler oscillators in the (Δ, κ)-parameter space.

where the bracket $\langle\rangle_T$ denotes averaging over the total time T. Here,

$$\mathrm{Var}(t) = \frac{1}{N^2}\sum_{i,j}^{N}(x_{ij}-\bar{x})^2, \quad \bar{x} = \frac{1}{N^2}\sum_{i,j}^{N}x_{ij} \tag{40}$$

is the spatial variance at time t, and

$$\mathrm{Cov}(t) = \frac{1}{N^2}\sum_{i,j}^{N}\frac{1}{|\mathcal{N}_{ij}|}\sum_{b\in\mathcal{N}_{ij}}^{N}\left(x_{ij}-\bar{x}\right)\left(b-\bar{x}\right) \tag{41}$$

is the purely spatial auto-covariance of nearest neighbors with b consisting of all $|\mathcal{N}_{ij}| = 4$ elements of a von Neumann neighborhood $\mathcal{N}_{ij}$ at each lattice site x_{ij}.

Spatiotemporal coherence $\mathbb{S}$ is effective in analyzing nearest neighbor relationships in space and time. The larger the $\mathbb{S}$, the better the pattern coherence.

On the other hand, spatiotemporal coherence of a lattice of coupled elements can be characterized by the degree of phase and temporal synchronization. Phase synchronization of neighboring elements is measured as [91]

$$s_i = \sin^2\left(\frac{\phi_i-\phi_{i+1}}{2}\right), \tag{42}$$

where ϕ_i is the phase of the ith element determined as [114]

$$\phi_i = 2\pi\left(\frac{t-\tau_k}{\tau_{k+1}-\tau_k}+k\right), \tag{43}$$

with τ_k being the time of the kth peak.

The degree of phase synchronization in the network of coupled elements is defined as a spatiotemporal average of s_i over all time and all elements, as follows

$$\Phi = \lim_{T\to\infty}\frac{1}{T}\int_0^T\left(\frac{1}{N}\sum_{i=1}^{N}s_i\right)dt. \tag{44}$$

In a completely synchronized network $\Phi \approx 0$, and in a completely usynchronous network $\Phi \approx 0.5$.

As shown in Section 2.5, the temporal coherence is measured by jitter Eq. (4) and the probability distribution of the inter-peak intervals given by Eq. (7).

2.19. Spatial coherence

Spatial coherence is used to characterize spatial regularity of the system in the presence of noise, for example, in a d-dimensional lattice of locally coupled units. For this aim, the structure function can be defined as [115]

$$S(\mathbf{k},t) = \frac{\langle\hat{u}(\mathbf{k},t)\hat{u}(-\mathbf{k},t)\rangle}{V}, \tag{45}$$

where $\hat{u}(\mathbf{k},t)$ is the spatial Fourier transform of the vector field of one of the system variables of a particular unit i, V is the d-dimensional volume of the system, and $\langle\dots\rangle$ is an ensemble average over noise realizations.

In a system with spherical symmetry, the spherical average of the structural function can be calculated as

$$\bar{S}(k) = \int_{\Omega_k} S(\mathbf{k},t)d\Omega_k, \tag{46}$$

where $k = |\mathbf{k}|$ and Ω_k is a hyperspherical shell of radius k. If the function $\bar{S}(k)$ has a peak value $\bar{S}_P$ at $k = k_P$, spatial coherence can be estimated through SNR measured as the peak height (similar to Eq. (9))

$$H(\mathrm{dBm}) = \bar{S}_P - \bar{S}_N, \tag{47}$$

where $\bar{S}_N$ is the average level of background fluctuations at $k = k_P$. Spatial CR occurs if H has a maximum with respect to the noise level.

In a two-dimensional space, the structure function in Eq. (45) is simplified to [116]

$$S(k_x, k_y) = \frac{\langle H^2(k_x, k_y)\rangle}{Q}, \tag{48}$$

where $H(k_x, k_y)$ is the two-dimensional power spectrum of one of the system variables, say $V_{i,j}$ (the subscripts $i, j = 1, 2, \ldots, N$ denote each of the $N \times N$ coupled units in the network), at a certain time t and Q is the system area. In a system with circular symmetry, the circular average of the structure function can be found by Eq. (46) with $\mathbf{k} = (k_x, k_y)$, and Ω_k is a circular shell of radius $k = |\mathrm{k}|$. Finally, spatial coherence is characterized by SNR given by Eq. (47).

In addition, spatial coherence can be characterized by the normalized autocorrelation function in spatial domain $V_{i,j}$ defined as [117]

$$C(\xi, \nu) = \frac{\langle \tilde{V}_{i,j}\tilde{V}_{i+\xi,j+\nu}\rangle}{\tilde{V}^2_{i,j}}, \tag{49}$$

where $V_{i,j} = \langle V_{i,j} - \langle V_{i,j}\rangle\rangle$ is are the spatial average of the whole lattice at a particular time t, and ξ and ν are spatial lag variables measured as a change in position from the starting i and j values.

Similar to the temporal autocorrelation function (see Eq. (1)) which characterizes the temporal order, the spatial order can be characterized by spatial correlation length

$$\lambda = \sum_{i=0}^{N}\sum_{j=0}^{N} C^2(i, j), \tag{50}$$

where λ is calculated by averaging several realizations. Larger λ means higher spatial scale of the network ordered pattern and simpler spatial structure of spiral waves.

2.20. Effective diffusion coefficient

A spike train considered in the previous Section 2.4 can be represented as a sequence of δ-functions centered at spike times T_m, i.e.,

$$s(t) = \sum_m \delta(t - T_m). \tag{51}$$

The number of spikes in the time interval $[0, T]$, referred to as the spike count, can be obtained by integrating the spike train function in Eq. (51), i.e.,

$$n(T) = \int_0^T s(t)\, dt. \tag{52}$$

The spike count is a stochastic variable that undergoes diffusive spreading, so that its variance grows linearly in time. The slower this growth, the more coherent the corresponding spike sequence is, since for a purely periodic spike sequence, the variance $n(T)$ does not grow at all. The rate of the diffusive spreading is given by the effective diffusion constant [14]

$$D_{\mathrm{eff}} = \lim_{T\to\infty} \frac{\left\langle \left(n(T) - \langle n(T)\rangle \right)^2 \right\rangle}{2T}. \tag{53}$$

The calculation of D_{eff} is significantly simplified for renewal processes, providing the following relation [118]

$$D_{\mathrm{eff}} = \frac{\eta^2}{2\langle T\rangle} \propto \tau_c^{-1}, \tag{54}$$

where η is the Fano-factor given by Eq. (5) and τ_c is the characteristic correlation time defined by Eq. (2).

As in the case of the Fano-factor, the minimum in the dependence of the effective diffusion constant on the noise intensity evidences the existence of CR.

It should be noted that not all coherence measures defined above were used to characterize CR. In the next sections, we will review the most interesting, in our opinion, theoretical and experimental results on CR in excitable networks including the brain neural network.

3. Coherence resonance in neural network models

The concept of CR was introduced in relation to an excitable system under the influence of noise. In particular, Gang et al. [2] discovered the CR behavior in a simple two-dimensional model of a limit cycle oscillator near a saddle–node bifurcation in the dependence of SNR, calculated by Eq. (10), on the noise intensity. Since CR is induced by noise, it was first mentioned as "stochastic resonance without external periodic force" [2], then as "autonomous stochastic resonance" [10,119]. Pikovsky and Kurths [3] used the term "coherence resonance" to characterize noise-induced order of spikes in an excitable system. They found that near the excitation threshold, a certain level of noise makes the spiking dynamics more regular than for other noise intensities. Above the bifurcation threshold, a limit cycle arises, whereas below the threshold, self-oscillations appear in transients only, when the system relaxes to an equilibrium state. In such situations noise can temporarily raise the system above the bifurcation threshold and thereby induce the limit cycle. If the period of this cycle is much longer than the time scale over which it is triggered by noise, the ratio between the dispersion of the period and its mean is very small, and we deal with CR. Thus, by adjusting the noise intensity, we can optimize the degree of coherence.

3.1. Mechanism of coherence resonance in excitable systems

The mechanism of CR in excitable systems is well described by Muratov et al. [120] with a set of excitatory and recovery variables. The general excitable system contains a set of excitatory and recovery variables, denoted by u and v, respectively, whose dynamics is determined as

$$\begin{aligned} \dot{u} &= f(u, v) + \xi(t), \\ \dot{v} &= \alpha g(u, v), \end{aligned} \tag{55}$$

where f and g are nonlinear functions, $\alpha \ll 1$ is the time-scale ratio of slow u and fast v variables, and $\xi(t) = \sqrt{D}\eta(t)$ is white noise of amplitude D and normal distribution $\langle \eta(t)\eta(t') \rangle = \delta(t-t')$. In the absence of noise, the excited state exists in transients only, and the trajectory rapidly approaches the slow manifold of the recovery state, and then continues on the time scale α^{-1} along this manifold and passes into a globally attracted equilibrium.

In the presence of noise, the trajectory can leave the recovery state and go to the excited state. For weak noise $D \ll 1$, this process occurs at the Kramers rate [121] given as

$$K = \omega \exp\left(-\frac{\Delta V(v)}{D}\right) \ll 1, \tag{56}$$

where $\Delta V(v)$ is a v-dependent energy barrier that must be overcome to escape from the slow manifold, and ω is a characteristic frequency of the system. The escape to the excited state occurs mainly due to the deterministic part of the dynamics. After that, the trajectory comes back to the slow manifold of the recovery state. The trajectory then continues along the slow manifold until another escape occurs, and so on. At a certain noise amplitude, this process can be almost periodic resulting in CR when the time scales of the fast and slow variables are comparable.

Assuming that the energy barrier $\Delta V(v)$ decreases as the trajectory approaches the slow manifold, the escape rate K in Eq. (56) becomes higher when D is small. If $\alpha \to 0$, then

$$D \log \alpha^{-1} \to \beta, \tag{57}$$

where β is a constant. Following Eq. (57), the escape from the slow manifold will occur with unit probability at point $v = v^*$ on this manifold, where v^* obeys:

$$\Delta V(v^*) = \beta, \tag{58}$$

provided that this equation has a solution on the stable branch of the slow manifold. Indeed, before v reaches v^*, the slow recovery is much faster than the escape rate, so that the system does not have enough time to complete before reaching v^*. But once v passes v^*, the escape rate becomes much faster than the recovery motion. Thus, the coincidence of time scales implied by Eq. (128) is the underlying mechanism of CR.

Excitable dynamics can be considered as a motion of a particle in a potential well in the presence of dissipation [122]. In this case, the mathematical model of the excitable system can be represented in the following oscillatory form [123,124]:

$$\ddot{y} = \gamma \dot{y} + \frac{dU}{dy} = 0, \tag{59}$$

where γ characterizes the dissipation and U is a potential function. The mathematical paradigmatic model for this type of excitability is the FitzHugh–Nagumo (FHN) system given by

$$\begin{aligned} \varepsilon \dot{x} &= x - \frac{x^3}{3} - y, \\ \dot{y} &= x + a + D\xi(t), \end{aligned} \tag{60}$$

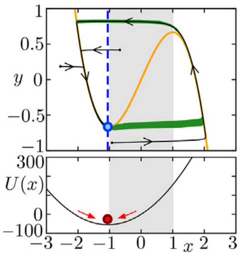

Fig. 6. (Upper panel) Phase-space trajectory and (lower panel) corresponding potential function of the FHN system in Eq. (60) in the excitable regime. The blue circle is the equilibrium point, the blue dashed line indicates the nullcline $\dot{y} = 0$, and the orange solid line shows the nullcline $\dot{x} = 0$. The green line is the trajectory driven by white Gaussian noise. The trajectories in the deterministic case ($\xi(t) = 0$) are indicated by black arrows. The red arrows show intra-well oscillations of a particle (red circle) in the absence of noise. The gray area corresponds to negative dissipation $\gamma(x) < 0$.

where ε is the parameter responsible for separation of slow and fast dynamics, $\xi(t)$ is the zero-mean white Gaussian noise with autocorrelation function $\langle \xi(t)\xi(t+\tau)\rangle = \delta(\tau)$, and D is the noise amplitude. The parameter a denotes oscillations, determined the nature of the equilibrium points and thus the excitability threshold of the FHN neuron. The system in Eq. (60) is in the excitable ($|a| > 1$) or in the oscillatory ($|a| < 1$) mode, and undergoes an Andronov–Hopf bifurcation when $a = 1$.

Writing the FHN model Eq. (60) in the oscillatory form of Eq. (59) of motion, we obtain

$$\varepsilon\ddot{x} + (x^2 - 1)\dot{x} + x + a = -D\xi(t) \tag{61}$$

with potential

$$U(x) = \frac{x^2}{2\varepsilon} + \frac{a}{\varepsilon}x \tag{62}$$

under dissipation

$$\gamma = \frac{x^2 - 1}{\varepsilon}. \tag{63}$$

For $|a| < 1$, the dissipation function $\gamma(x) < 0$ near the local minimum of the potential well. This means pumping energy, which destabilizes the equilibrium point and causes self-oscillations. The phase-space trajectory of the FHN system Eq. (61) in the excitable mode and the corresponding potential are shown in Fig. 6.

As stated above, noise $\xi(t)$ induces random switching from the region of stable equilibrium to the region of negative friction $\gamma(x)$. The drift of the phase point increases in the region of negative dissipation. If the pumping energy is sufficient, the phase-space trajectory forms a loop. Thus, both self-oscillatory excitation and excitability are associated with the presence of negative dissipation when a particle moves in a potential field. The motion along the loop is manifested as spikes in the $y(t)$ time series, as illustrated in Fig. 7. Weak noise results in rare spikes with variable interspike intervals, while stronger noise gives rise to more frequent spiking and increasing of the spiking regularity. A further increase in the noise intensity leads to the destruction of regularity. Thus, there is an optimal noise intensity corresponding to the most regular spiking and therefore higher system coherence.

Two measures of coherence such as Fano-factor η defined by Eq. (5) and effective diffusion coefficient D_{eff} given by Eq. (53) for the stochastic FHN system in Eq. (60) are shown in Fig. 8. For weak noise, the Fano-factor is close to 1 indicating that statistics of rarely occurring spikes is close to the Poisson distribution. With an increase in the noise amplitude, the Fano-factor decreases reaching its minimum at $D \approx 0.04$ and then increases again. The effective diffusion constant is minimal at the same noise amplitude $D \approx 0.04$, indicating that diffusive spreading of spike count is slowest for that noise amplitude.

There are also other self-oscillatory systems which operation is based on the same principle, for example, Van der Pol and Rayleigh systems, where the Andronov–Hopf bifurcation occurs, as well as excitable systems, where the transition to a self-oscillatory regime takes place in a saddle–node bifurcation, for example, the two-dimensional Hindmarsh–Rose neuron model [126].

Despite its apparent simplicity, the FHN model proved to be a useful tool for studying CR. The work of Pikovsky and Kurths [3] has prompted other researchers to continue investigation of CR in FHN [69,86,127–129], Hodgkin–Huxley [36,37,130,131], and other excitable systems numerically [68,83,90,132,133] and experimentally [67,69]. Meanwhile, investigation of CR was extended to complex networks of excitable units. In particular, CR was demonstrated in one-layer [18,19,21] and two-layer [25,45] networks of FHN oscillators coupled in various topologies including local, nonlocal, and global coupling [24], as well as in random and small-world networks of other nonlinear oscillators [7,33,40,42,134–136].

Similar to simple oscillatory systems, the coherence in complex networks is measured with the normalized autocorrelation function, characteristic correlation, jitter, and coherence factor defined by Eqs. (1)–(16) with the difference that the state variable x is replaced by the average value of the same variable of all N oscillators in the network.

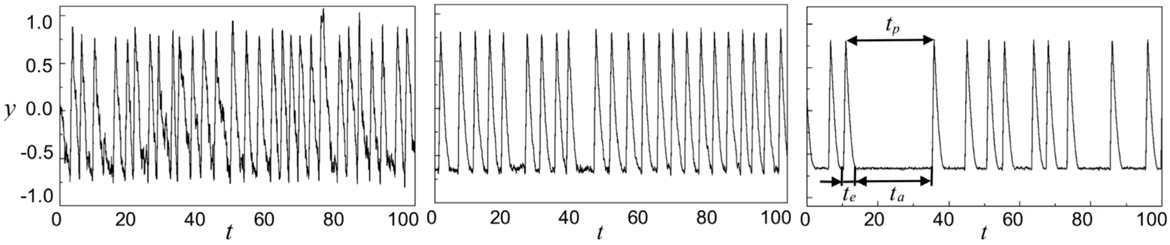

Fig. 7. Illustration of CR behavior in a noisy FitzHugh–Nagumo system. Time series of y variable for noise intensities (left) below resonance ($D < D_r$), (middle) at resonance ($D = D_r$), and (right) above resonance ($D > D_r$). The arrows show definitions of inter-peak interval t_p, activation time t_a, and pulse duration t_e, respectively.
Source: Based on data from [3].

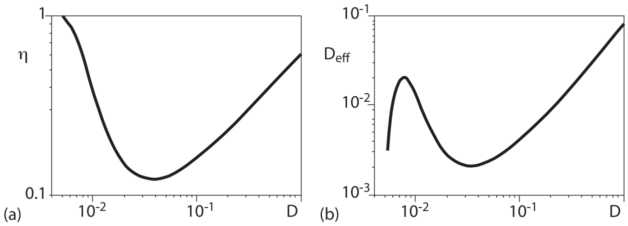

Fig. 8. (a) Fano-factor η and (b) effective diffusion coefficient D_{eff} of the spike count versus noise intensity D for the FHN neuron model with $a = 1.05$ and $\varepsilon = 10^{-3}$.
Source: Based on data from [125].

Let us start with a consideration of neuronal networks, where the most significant advances in the study of CR research have been obtained. The increased interest in mathematical modeling of neuronal networks significantly increased after neurobiological experiments with two electrically coupled neurons [137], in which various synchronous states were found. Numerous models were developed to simulate cooperative dynamics of coupled neurons. Some of them are based on iterative maps, others on ordinary differential equations. Depending on the coupling strength and synaptic delay time, connected neurons generate sequences of spikes and bursts that match in their timings with lag or anticipation [138].

Like all real systems, neural systems are subject to random perturbations. There are many sources of intrinsic neural noise. Among them, it is worth mentioning the quasi-random release of neurotransmitters by synapses, random synaptic input from other neurons, and random switching of ion channels [139]. Inherent neural noise plays an important role; it is needed for the good functioning of the nervous system in all levels of organization, from cells to the brain. Neural noise underlies important mechanisms of brain functionality and self-organization; it is important for signal detection and decision-making, preventing deadlocks [140–142]. Sometimes noise results in CR that can be beneficial for better neuronal network functionality.

3.2. Coherence resonance in a map-based neural network

We begin our consideration of CR in neuronal networks with a network of simple neuron-like systems modeled by the Rulkov map [143,144]. Although the Rulkov model does not provide a quantitative description of physiological processes in the membrane, it is capable of generating extremely complex and highly specific neural dynamics (silence, periodic spikes, and chaotic bursts), thereby largely reproducing most of the experimentally observed regimes [137], including spike adaptation, paths from silence to firing mediated by subthreshold oscillations, phase and antiphase synchronization, etc. Moreover, the Rulkov map is a very useful model for studying neural activity in large neuronal networks. In particular, Ferrari et al. [145] investigated bursting activity in a network of globally coupled Rulkov maps. The authors of the paper suggested to analyze the macroscopic signal of the whole network. Such an approach is very convenient when microscopic access to individual neurons is not possible, for example, to simulate experiments with neural cultures grown on a multielectrode matrix. The synchronized collective bursting activity of many neurons is associated with some pathological states, for instance, epilepsy [146–148] and migraine [149].

Here, we will show how the macroscopic approach can be applied to reveal mechanisms responsible for regularity of collective bursting dynamics. In particular, we will demonstrate how noise intensity, network size, and the number of stimulated neurons affect the network coherence. As a basic model we choose the Rulkov map [144]. Each neuron-like Rulkov element is described by the following system of equations with synaptic coupling

$$\begin{aligned} x_{n+1} &= f(x_n, x_{n-1}, y_n + \beta_n), \\ y_{n+1} &= y_n - \mu(x_n + 1) + \mu\sigma + \mu\sigma_n + \mu A^{\xi}\xi_n, \end{aligned} \tag{64}$$

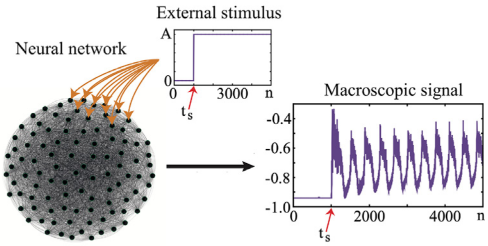

Fig. 9. Schematic representation of the research design. (Left) The external stimulus with amplitude A is applied at time t_s to excite Na neurons in the network of N neurons. (Right) Time series averaged over all neurons in the network.

where x and y are fast and slow variables associated with membrane potential and gating variables, respectively, α, σ and $\mu \in (0, 1]$ are parameters which regulate the system dynamics, ξ is Gaussian noise with zero mean and unity standard deviation, A^{ξ} is the noise amplitude, and f is a piecewise function defined as

$$f(x_n, x_{n-1}, y_n) = \begin{cases} \alpha/(1-x_n) + y_n, & \text{if } x_n \leq 0, \\ \alpha + y_n, & \text{if } 0 < x_n < \alpha + y_n \text{ and } x_{n-1} \leq 0, \\ -1, & \text{if } x_n \geq \alpha + y_n \text{ or } x_{n-1} > 0, \end{cases} \tag{65}$$

constructed in a way to reproduce different regimes of neuron-like activity, such as spiking, bursting and silent regimes. Here, β_n and σ_n are parameters related to external stimuli and defined as

$$\begin{aligned} \beta_n &= \beta^e I_n^{ext} + \beta^{syn} I_n^{syn}, \\ \sigma_n &= \sigma^e I_n^{ext} + \sigma^{syn} I_n^{syn}, \end{aligned} \tag{66}$$

where β^e and σ^e are coefficients used to balance the effect of external current I_n^{ext} defined as

$$I_n^{exp} = \begin{cases} 0, & n < t_s, \\ A, & n \geq t_s, \end{cases} \tag{67}$$

β^{syn} and σ^{syn} are coefficients of chemical synaptic coupling [150], and I_n^{syn} is a synaptic current given as

$$I_{n+1}^{syn} = \gamma I_n^{syn} - g_{syn} * \begin{cases} (x_n^{post} - x_{rp})/(1 + e^{-k(x_n^{post} - \theta)}), & \text{when } x_n^{pre} \geq \alpha + y_n^{pre} + \beta_n^{pre}, \\ 0, & \text{otherwise,} \end{cases} \tag{68}$$

where $g_{syn} \geq 0$ is the strength of synaptic coupling, $\theta = -1.55$ and $k = 50$ are synaptic parameters which stand for the synaptic threshold behavior. The super indices *pre* and *post* refer, respectively, to the presynaptic and postsynaptic variables, $\gamma \in [0, 1]$ is the synaptic relaxation time defining a portion of synaptic current preserved in the next iteration, and x_{rp} is a reversal potential determining the type of synapse, inhibitory or excitatory. The parameter values are chosen so that uncoupled neurons are in a resting state, namely, $\alpha = 3.65$, $\sigma = 0.06$ and $\mu = 0.0005$. We also assume $\beta^e = 0.133$, $\sigma^e = 1.0$, $\beta^{syn} = 0.1$, $\sigma^{syn} = 0.5$, and $x_{rp} = 0$.

Consider now a network of N globally coupled neurons with random coupling strength $g_{syn} \in [0, 1]$ and relaxation time $\gamma \in [0, 0.5]$. The network design is presented in Fig. 9. The macroscopic signal is the averaged time series of all network neurons. The research design reflects a perception process, for example, visual perception, when a stimulus is detected by a small number of neurons, for instance, in the retina, and then the signal is transmitted to a larger neuronal network, such as occipital cortex. The macroscopic signal from the large neuronal network can be detected using different brain techniques, such as electroencephalography (EEG), magnetoencephalography (MEG), positron emission tomography (PET), functional magnetic resonance imaging (fMRI), etc.

Initially, without external stimulation and in the absence of noise, all neurons are in a silence regime. Then, at the time moment t_s the external stimulus in the form of a rectangular pulse with amplitude A is applied to a small neural network of Na neurons to excite them. The neurons from the small network are coupled to the neurons from the larger network. Because of the random coupling strength, some neurons from the large network are excited, while the others remain in a silence regime. The analysis of the averaged signal from all network neurons allows us to reveal macroscopic dynamics representing the global network behavior.

The macroscopic signal shown in the right-hand panel of Fig. 9 exhibits the time series of the fast variable x averaged over all network neurons:

$$x_{avr}(t) = \frac{1}{N} \sum_{i=1}^{N} x_i(t), \tag{69}$$

where i is an index of neuron, $N = 100$ is the number of neurons in the network.

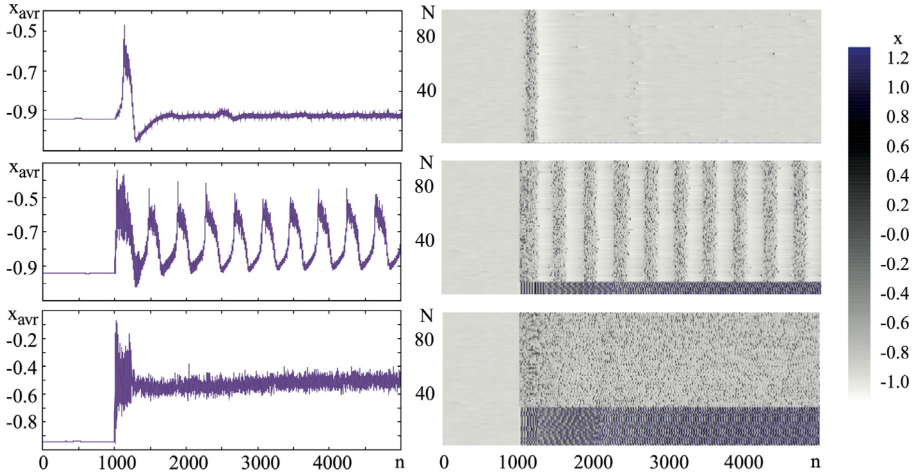

Fig. 10. Time series of (left column) average membrane potential and (right column) membrane potential of all neurons in the network of $N = 100$ neurons, when the stimulus with amplitude $A = 1$ is applied to (upper row) $Na = 1$, (middle row) $Na = 10$, and (lower row) $Na = 30$ neurons. $A^{\xi} = 0.1$. The vertical dark stripes for $Na = 10$ form a periodic structure, thus indicating the regularity in the inter-spike intervals (ISI) unlike cases of $Na = 1$ and $Na = 30$, when the network dynamics is completely incoherent.

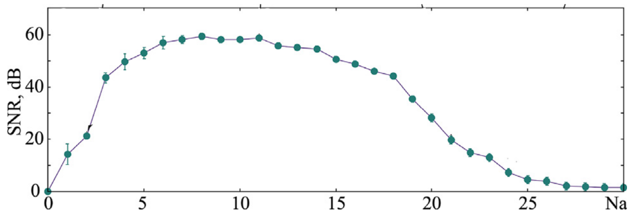

Fig. 11. Coherence resonance in terms of signal-to-noise ratio (SNR) versus the number of stimulated neurons Na at $A^{\xi} = 0.1$ and $A = 1$ for the network of $N = 100$ neurons.

Fig. 10 represents the time series of x_{avr} (left panels) and the membrane potentials of all network neurons (right column) for different sizes of the small network. One can see that there is an optimal network size (middle row), when the macroscopic signal is more regular, i.e., the network dynamics is more coherent.

Network coherence is measured using signal-to-noise ratio (SNR) obtained from the power spectrum of x_{avr}. The maximum power S_P appears at the average frequency f_P of spiking neurons. While S_P reflects the contribution of the regular behavior, the noise mainly affects the background component P_N at the same frequency f_P [90,151,152]. The SNR is calculated at the dominant frequency f_P using Eq. (9).

Fig. 11 shows the dependence of SNR on the number of stimulated neurons Na. As Na is increased, SNR first increases rapidly at small values of Na, reaching its maximum at Na between 6 and 11, and then gradually decreases to 0. This means that the network coherence is resonant in relation to the number of excited neurons. Since each neuron contributes to the overall noise in the neural network, this dependence indicates the presence of CR.

This result confirms previous foundings [19,153] that coherence depends on the network size, and that there is an optimal number of coupled units for which the network coherence maximizes.

On the other hand, CR can be derived from time series by measuring the degree of incoherence calculated as

$$H = \frac{1}{N}\sum_{i=1}^{N} h_i^2 - \left(\frac{1}{N}\sum_{i=1}^{N} h_i\right)^2, \quad h_i = \sqrt{\frac{1}{M - m_0 + 1}\sum_{m=m_0}^{M} R_m(i)}, \tag{70}$$

where R_m is interspike interval (ISI) between mth and $(m+1)$-th spike, M is the number of spikes ($m = 1, 2, \ldots, M$), and m_0 is the number of transient spikes.

The degree of incoherence as a function of the noise amplitude is shown in Fig. 12. One can see that as A^{ξ} is increased, H first decreases and then gradually increases. Thus, at a certain noise level, the degree of incoherence H reaches its minimum value, thus exhibiting coherence resonance.

The existence of CR was also found in networks of physiologically relevant models. In the next section we will show how this resonance manifests itself in the network of Hodgkin–Huxley (HH) neurons, and how it is measured.

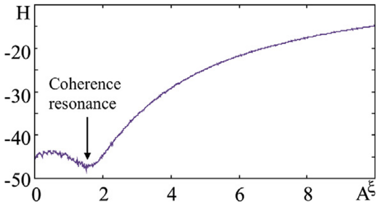

Fig. 12. Degree of incoherence H versus noise amplitude A^ξ. Coherence resonance occurs at $A^\xi \approx 1.5$. $A = 1.0$.

3.3. Coherence resonance in a network of Hodgkin–Huxley neurons

Similar to the neural network of Rulkov maps, we consider here a two-layer network of connected HH neurons, to simulate the process of visual perception in the neural network of the brain. The network contains small and large subnetworks with $N^{ex} = 5$ and $N = 50$ neurons, respectively, representing the visual area of the thalamus and visual cortex (see Fig. 13). Within each subnetwork all elements are connected to each other with probability $p = 0.3$ of making a one-way connection between a neuron from the first network to a neuron from the second. An external stimulus is simulated by applying an external current of constant amplitude A to all N^{ex} neurons from the first network connected to all neurons of the second layer unidirectionally. Every neuron was subjected to its own zero-mean white Gaussian noise. We study the effect of the external stimulus on the dynamics of neurons in the second layer.

The time evolution of the transmembrane potential of each HH neuron is described by the following differential equations [154]

$$\begin{aligned} C_m \dot{V}_i = &- g_{Na}^{max} m^3 h (V_i - V_{Na}) - g_K^{max} n^4 (V_i - V_K) - \\ &- g_L^{max}(V_i - V_L) + I_i^{ext} + I_i^{syn}, \end{aligned} \tag{71}$$

$$\dot{x}_i = \alpha_{x_i}(V_i)(1 - x_i) - \beta_{x_i}(V_i) x_i + \xi_{x_i}(t), \quad x = m, n, h, \tag{72}$$

where $C_m = 1$ μF/cm^3 is the capacity of the cell membrane, I^{ext} is the external bias current (in μA/cm^2) injected into every neuron of the small network, V is the membrane potential (in mV) of ith neuron ($i = 1, \ldots, N$), $g_{Na}^{max} = 120$ mS/cm^2, $g_K^{max} = 36$ mS/cm^2, and $g_L^{max} = 0.3$ mS/cm^2 respectively denote maximal sodium, potassium and leakage conductances, when all ion channels are open, $V_{Na} = 50$ mV, $V_K = -77$ mV and $V_L = -54.4$ mV are reversal potentials for sodium, potassium and leak channels, respectively, m, n, and h represent mean ratios of open gates of specific ion channels, n^4 and m^3h are mean portions of open potassium and sodium ion channels within a membrane patch, $\alpha_x(V)$ and $\beta_x(V)$ are rate functions given as [155]

$$\begin{aligned} \alpha_{m_i}(V_i) &= \frac{0.1(25 - V_i)}{\exp[(25 - V_i)/10] - 1}, \\ \beta_{m_i}(V_i) &= 4\exp(-V_i/18), \\ \alpha_{h_i}(V_i) &= 0.07\exp(-V_i/20), \\ \beta_{h_i}(V_i) &= \frac{1}{1 + \exp[(30 - V_i)/10]}, \\ \alpha_{n_i}(V_i) &= \frac{0.01(10 - V_i)}{\exp[(10 - V_i)/10] - 1}, \\ \beta_{n_i}(V_i) &= 0.125\exp(-V_i/80). \end{aligned} \tag{73}$$

The term $\xi_x(t)$ in Eq. (72) denotes independent zero-mean Gaussian white noise sources with autocorrelation functions defined by [156]

$$\begin{aligned} \left\langle \xi_{m_i}(t) \xi_{m_i}(t') \right\rangle &= \frac{2\alpha_{m_i}\beta_{m_i}}{M_{Na}(\alpha_{m_i} + \beta_{m_i})} \delta(T - T'), \\ \left\langle \xi_{h_i}(t) \xi_{h_i}(t') \right\rangle &= \frac{2\alpha_{h_i}\beta_{h_i}}{M_{Na}(\alpha_{h_i} + \beta_{h_i})} \delta(T - T'), \\ \left\langle \xi_{n_i}(t) \xi_{n_i}(t') \right\rangle &= \frac{2\alpha_{n_i}\beta_{n_i}}{M_K(\alpha_{n_i} + \beta_{n_i})} \delta(T - T'), \end{aligned} \tag{74}$$

where N_{Na} and N_K denote the total number of sodium and potassium channels within a membrane patch, calculated as $N_{Na} = \rho_{Na} S$ and $N_K = \rho_K S$ with $\rho_{Na} = 60$ μm^2 and $\rho_K = 18$ μm^2 being sodium and potassium channel densities, respectively, and $S = 10^{-S^{pow}}$ is the membrane patch area of each neuron (S^{pow} being the noise level).

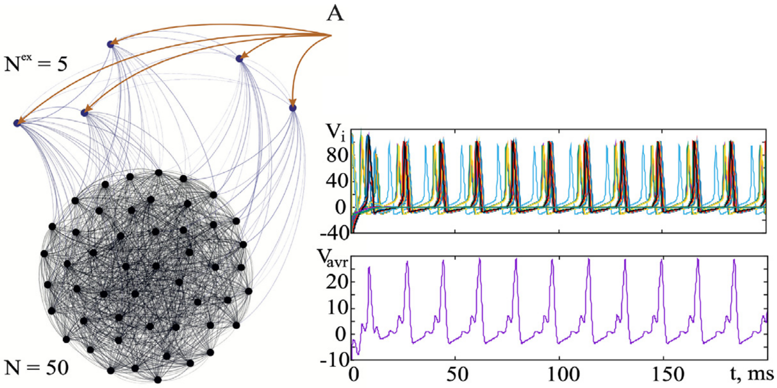

Fig. 13. Network design. The external stimulus with amplitude A is applied to $N^{ex}=5$ neurons from the small network, connected to all neurons from the large network with probability $p=0.3$. Every neuron is subjected to its own Gaussian noise. V_i and V_{avr} are average signals of all neurons from small and large networks calculated with Eq. (76).

The coupling is realized via chemical synapses with total synaptic current I_i^{syn} in the following form [157]:

$$I_i^{syn} = \sum_{j\in neigh(i)} g_c\alpha(t-t_0^j)(E_{rev}-V_i), \tag{75}$$

where $\alpha(t)=\exp(-t/\tau_{syn})\Theta(t)$ ($\Theta(t)$ being the Heaviside step function and $\tau_{syn}=3\,\text{ms}$) describes the temporal evolution of the synaptic conductance, g_c is the maximal conductance of the synaptic channel, and t_0^j is the time at which presynaptic neuron j fires.

Numerical calculations of Eqs. (71)–(74) were performed using the fourth-order Runge–Kutta algorithm with a fixed integration time step $\Delta t = 10\,\mu\text{s}$. The times series of the average macroscopic signal over all neurons

$$V_{avr} = \frac{1}{N}\sum_{i=1}^{N} V_i \tag{76}$$

is shown in Fig. 13.

The system coherence is derived by calculating SNR from the power spectrum obtained by the Fourier transformation

$$E(f) = \frac{1}{2\pi}\int_{-\infty}^{\infty} x(t)\exp^{-i2\pi/t}\,dt. \tag{77}$$

The maximum power $S_P = E_P^2$ in the power spectrum appears at the average frequency of spiking neurons f_P. Therefore, this spectral component reflects the contribution of a regular behavior, while noise contributes mainly to the background component $S_N = E_N^2$ at the same frequency (see Fig. 4). The degree of coherence is measured from the power spectra according to Eq. (9). In addition, the coherence is calculated as the characteristic correlation time defined by Eq. (2).

The two-dimensional diagram of the characteristic correlation time and noise intensity on the external stimulus amplitude is presented in Fig. 14. One can see the area of strong coherence (the tongue with large τ_c).

In Fig. 15 we plot the dependences of SNR and τ_c on I_{ext} at $\xi = 0.1$. One can see the existence of the coherence resonance with respect to the external current. While for a small amplitude of the external stimulus, all neurons are in a silent mode (black area in Fig. 15), an increase in the stimulus amplitude leads to increasing both the SNR and characteristic correlation time. However, for $I_{ex} > 10$, the both values decrease, so that the coherence has a resonant character.

Fig. 16 shows the dependence of τ_c on the noise intensity S^{pow} for different external signal amplitudes I^{ext}. In the absence of noise (purple curve in the left graph in Fig. 16), below the excitation threshold ($I^{ext} < 6.8\ \mu\text{A/cm}^2$) all neurons are in a silent regime and $\tau_c \approx 0$. Whereas above the excitation threshold ($I^{ext} > 6.8\ \mu\text{A/cm}^2$), the neurons switch to a spiking regime. As I^{ext} is increased, the correlation time τ_c grows, i.e., coherence is improved. The introduction of low-amplitude noise ($S^{pow}=0.1$, red curve) reduces network coherence. At the same time, the qualitative network behavior remains similar, i.e., coherence monotonically improves as I^{ext} is increased. However, stronger noise ($1.9 < S^{pow} < 2.3$) changes the network behavior so that the dependence of τ_c on I^{ext} behaves non-monotonically; it has a maximum at a certain value of I^{ext}. This means the existence of CR in the neural network, i.e., there are optimal noise amplitude and external current at which the average spiking behavior is more regular. Stronger noise ($S^{pow} > 2.3$) causes coherence collapse and CR does not appear.

The time series and probability distribution function (PDF) of ISI are presented on the right-hand side of Fig. 16) in the absence (upper panels) and presence (lower panels) of external noise. The network coherence is estimated via PDF; the

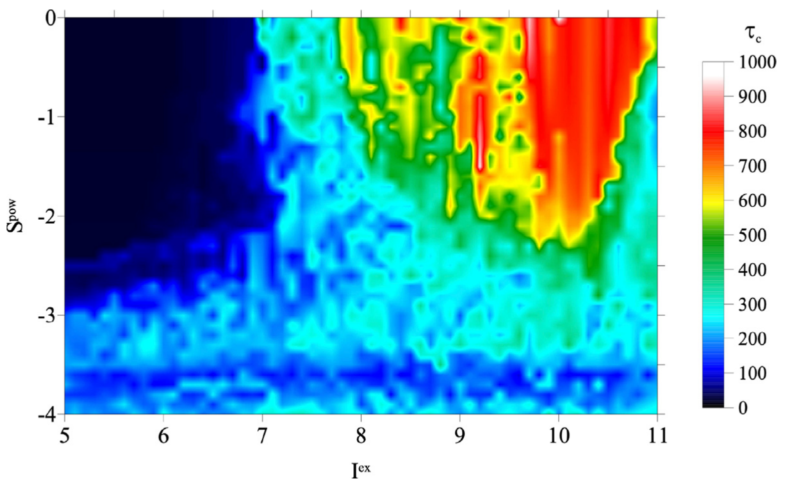

Fig. 14. Characteristic correlation time τ versus external stimulus I_{ext} and noise value $S^{pow} = -\log \xi$.

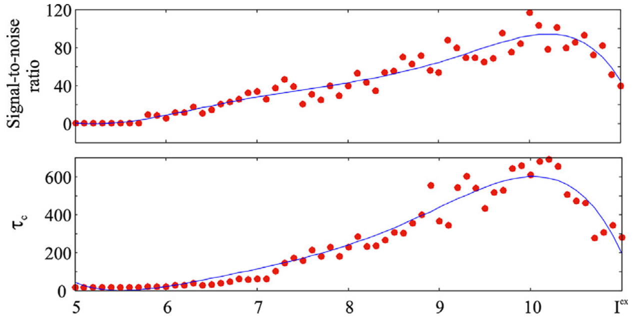

Fig. 15. SNR and characteristic correlation time from external stimulus amplitude (points) at $\xi = 0.1$. The lines are approximated dependencies by the 6th-order polynomial.

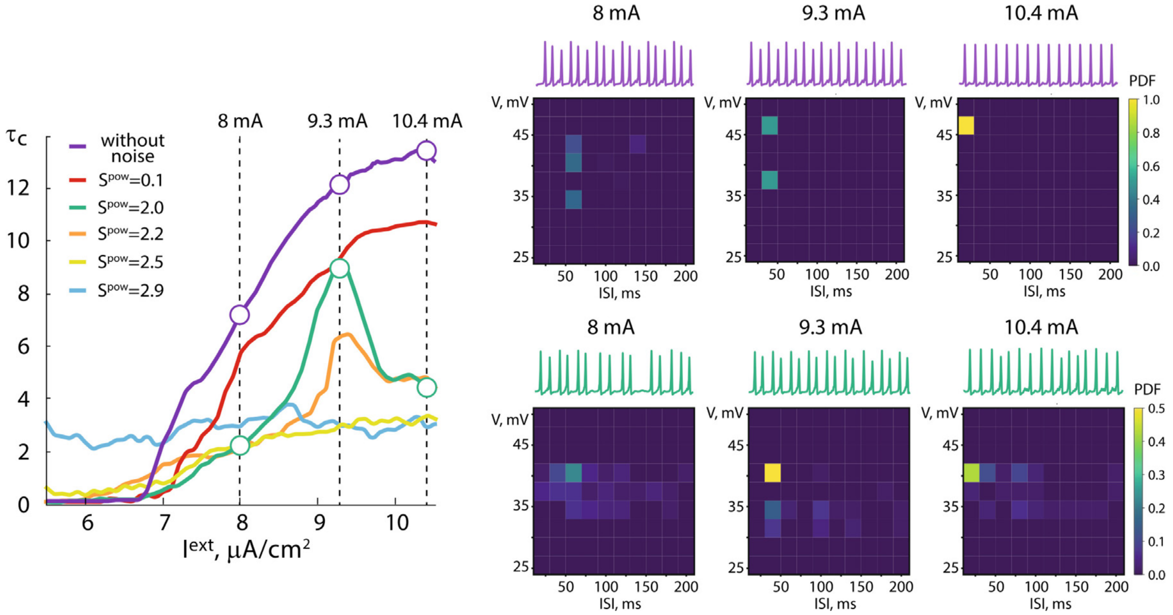

Fig. 16. Coherence resonance in the network of Hodgkin–Huxley neurons. Correlation time τ_c versus the external signal intensity I^{ext} in the absence (purple curve) and in the presence of intrinsic noise for different values of the noise intensity S^{pow}. (Right) Macroscopic activity of the model cortical network: (upper traces) time series and (squares) probability distribution function (PDF) (color scale) of ISI under increasing I^{ext} in the absence (upper row) and in the presence (lower row) of intrinsic noise for different I^{ext}.

higher the PDF peak, the better the regularity. The diagrams illustrate the network behavior for three values of the external stimulus amplitude I^{ext}: slightly above the excitation threshold ($8\,\mu$A/cm^2), at the optimal amplitude corresponding to maximum τ_c ($9.3\,\mu$A/cm^2), and above the optimal amplitude ($10.4\,\mu$A/cm^2). In the absence of intrinsic noise (upper row), an increase in I^{ext} causes the transition from a slightly incoherent collective behavior (at $I^{ext} = 8\,\mu$A/cm^2) to regular spikes (at $I^{ext} = 10.4\,\mu$A/cm^2) characterized by homogeneity of both the spike amplitude and ISI. The introduction of noise crucially changes the collective behavior in the neural network. As seen from the lower raw, both ISI and spike amplitude are strongly heterogeneous at small ($I^{ext} = 8\,\mu$A/cm^2) and large ($I^{ext} = 10.4\,\mu$A/cm^2) amplitudes with maximum PDF at 0.22 and 0.41, respectively, whereas the most regular dynamics occurs at the intermediate stimulus amplitude ($I^{ext} = 9.3\,\mu$A/cm^2), where the highest PDF maximum (0.5) appears. Thus, there exist optimal values of the noise amplitude and I^{ext} for coherent network dynamics.

Multiple CR was also detected in networks of Hodgkin–Huxley neurons with periodically modulated [31,32] and delayed coupling [30,34,35].

The obtained results stimulated further research in this direction. Since SNR can be improved by adjusting the network size, intrinsic noise, and the number of stimulated neurons, the important questions arise: Does coherence resonance really exist in the brain neural network, and does it help detect weak stimuli? To answer these questions, neurophysiological experiments were carried out.

3.4. Mean-field approach to describe coherence and anticoherence resonances in neuronal population of FitzHugh–Nagumo neurons

So, in the previous sections we have analyzed the CR effect in excitable neural network models. However, there is a possibility to build a CR theory in the framework of analytical approach, which implies mean-field limits for globally and locally connected neuron populations. The mean-field limit refers to an averaged behavior of a complex network when the number of elements increases to infinity. Recently, Baspinar et al. [24] applied the mean-field approach to a network of FHN neurons in different coupling configurations. Studying the effects of the coupling strength and noise intensity on CR, they used both the network and mean-field models and found a good agreement between analytical and numerical results in the case of globally coupled FHN neuronal network. The prediction accuracy of the mean-field method in the case of locally coupled elements is much lower. Let us consider their approach in more detail.

The deterministic FHN ordinary equations describing the evolution of a single neuron belonging to a network read as

$$\begin{aligned} &\varepsilon\frac{dx_i}{dt} = f(x_i, y_i) + \frac{\sigma}{2P}\sum_{j=i-P}^{i+P}\left(x_j - x_i\right), \qquad \frac{dy_i}{dt} = g_a(x_i), \\ &f(x, y) = x - \frac{x^3}{3} - y, \qquad g_a(x) = x + a, \end{aligned} \tag{78}$$

where σ is the coupling strength, x_i is the activator (membrane potential) and y_i is the inhibitor (recovery) variables of the ith neuron, $i = 1, \dots, N$, N is the number of neurons, $\varepsilon = 10^{-2}$ and a are the control parameters (see the description of Eq. (60)). The topology parameter P determines the network architecture of the analyzed neural population. Specifically, P is the number of nearest neighbors of the ith neuron in each direction of the ring. If $P = 1$, the coupling is local, i.e., the neuron is only coupled with its nearest neighbors. If $P \approx (N-1)/2$, the neurons are globally coupled. If $1 < P < (N-1)/2$, we deal with non-local coupling in the network.

The deterministic network model in Eqs. (78) can be rewritten in a stochastic form by adding a Gaussian white noise term $dW_i(t)$ to the recovery variable equation of each neuron, where $dW_i(t)$ is built from an independent Wiener process [21,45]. Then, the stochastic FHN equations can be read as follows

$$\varepsilon dx_i = f(x_i, y_i)dt + \frac{\sigma}{2P}\sum_{j=i-P}^{i+P}\left(x_j - x_i\right)dt, \quad dy_i = g_a(x_i)dt + \sqrt{2D}\,dW_i, \tag{79}$$

where D is the noise intensity.

In the globally coupled mean-field framework, the topology parameter $P = N/2$ as $N \to \infty$. In this case, we can change, without loss of generality, the indexing of the coupling term in Eqs. (79) according to $\sum_{j=1}^{N+1}(x_j - x_i)$. It should be noted that the noise terms in Eqs. (79) are assumed to be independent and equally distributed for each neuron as well as for each state variable. Then, each state variable can be considered as a stochastic process representing the values of the state variable changing randomly in time. Thus, the state variables x_i and y_i of each neuron evolve according to their associated probability distributions, which converge in the thermodynamic limit to the ones of mean-field state variables x and y, characterized as

$$\begin{aligned} &\lim_{N\to\infty}\max_{i=1,\dots,N}\mathcal{E}\left[\sup_{s\le t}\left(x_i(s) - x(s)\right)^2\right] = 0, \\ &\lim_{N\to\infty}\max_{i=1,\dots,N}\mathcal{E}\left[\sup_{s\le t}\left(y_i(s) - y(s)\right)^2\right] = 0 \end{aligned} \tag{80}$$

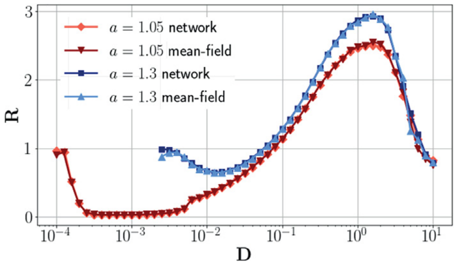

Fig. 17. Standard deviation of ISI R for a globally coupled population of stochastic FHN neurons in both the neuronal network given by Eqs. (79) and its mean-field system derived by Eqs. (82) for fixed coupling strength $\sigma = 0.1$, $N = 100$, $\varepsilon = 10^{-2}$, and varying noise intensity D. Light red diamonds identify the network while dark red downward triangles identify the mean-field results for $a = 1.05$; dark blue squares identify the network while light blue upward triangle identify the mean-field simulations for $a = 1.3$.
Source: From [24].

with $\mathcal{E}$ denoting expectation value. According to Refs. [158,159] the state variables x and y comprise the solution to the mean-field equations

$$\varepsilon dx = f(x, y)dt + \sigma\,(\mathcal{E}[x] - x)\,dt, \quad dy = g_a(x)dt + \sqrt{2D}\,dW, \tag{81}$$

which can be obtained for the initial stochastic FHN network in Eqs. (79) based on (i) a unique solution of Eqs. (81) exists for finite time, assuming that the terms f and g_a are locally sufficiently regular (locally Lipschitz), and (ii) for each neuron in the network the probability distributions of processes x_i and y_i converge to the probability distributions of the mean-field state variables x and y, respectively.

Eqs. (81) correspond to the classical mean-field limit of globally coupled FHN-type oscillator networks. Baspinar et al. [24] considered an extended version of the mean-field limit associated with the globally coupled FHN system. In Refs. [158,159] it was shown that the same results and the corresponding relations as in Eqs. (81) take place for the extended adapted version as well:

$$\varepsilon dx = f(x, y)dt + \sigma\,(\mathcal{E}[x] - x)\,dt + \sqrt{2\varepsilon\overline{D}}\,d\overline{W}, \qquad dy = g_a(x)dt + \sqrt{2D}\,dW. \tag{82}$$

Here, dW and $d\overline{W}$ are the noise terms generated independently from a Gaussian distribution with zero mean and unit variance with the noise intensity levels as D and $\overline{D}$, respectively. The choice of this extended adapted model is motivated by the presence of the global coupling term. The noise effects arising from the coupling can be considered by introducing an additional noise term $d\overline{W}$. From biophysical point of view, the additional noise in the first equation of Eqs. (82) describes the stochastic nature of the gap junction media, which creates small random changes in the coupling current, while the noise term in the second equation corresponds to the random switching of channel gates arranging the ionic current [157,160].

The mean-field limit in Eqs. (81) or (82) describes the population behavior by employing a single FHN system once the number of the neurons in the population is sufficiently high, whereas, for the network Eqs. (79), a separate stochastic FHN equations should be solved for each neuron in the network. In other words, the network equations require a high-dimensional stochastic system while the mean-field limit requires only a two-dimensional dynamical system, being a good representative of the averaged dynamics of the population and making analytical treatment of the system feasible.

Let us consider the role of noise intensity D in CR in a network of globally coupled FHN oscillators. Fig. 17 demonstrates the dependence of the standard deviation of ISI R (Eq. (6)) on the noise intensity calculated for both the initial FHN neuronal network given by Eqs. (79) and the mean-field model derived by Eqs. (82). CR is observed for both presented values of a, where a minimum in R emerges. The location of the minimum depends on the excitability threshold value, and it occurs for different noise intensities D in the two cases. It is worth noticing here that, if the system is closer to the Hopf bifurcation point, i.e., for $a = 1.05$, it requires lower noise intensity for CR to occur. And vice versa, if the system is further away from the Hopf bifurcation point ($a = 1.3$), the network requires higher noise intensity.

It should be noted that for both values of a, the $R(D)$-curves have both extrema, minimum and maximum. The occurrence of the maximum in the vicinity of $D_{ACR} \approx 2$ is associated with the phenomenon of anticoherence resonance. The interesting fact is that the anticoherence resonance is captured by the mean-field analysis. The emergence of anticoherence resonance is due to the increasing role played by noise, which destroys the refractory time proper of each neuron, thus allowing for infinitely small ISIs. At a very low noise intensity, the spike generation is coherent and all neurons spike with almost the same time interval. For increasing noise intensity, longer and more random time intervals are possible between successive spikes. Finally, at the maximum ($D = D_{ACR}$) and for wider noise intensities, noise guides the dynamics and destroys the coherence. We observe infinitely small ISIs which are a signature of a fluctuation-driven dynamics, where neurons overcome the threshold very often due to the high noise intensity.

In the case of local coupling with $P = 1$ the second term in the first equation in Eqs. (79) for the ith neuron can be rewritten in the simple form $\sigma(x_{i-1} - 2x_i + x_{i+1})dt/2$. Assuming the periodic boundary conditions

$$x_{N+K} = x_K \quad \text{for all} \quad K \in \{-N, -N+1, \dots, N-1, N\}, \tag{83}$$

the average dynamics of a locally coupled FHN network in the thermodynamic limit can be written as

$$\begin{aligned} \frac{\varepsilon}{N}\sum_{i=1}^{N} dx_i &= \frac{1}{N}\sum_{i=1}^{N} f(x_i, y_i)dt + \frac{\sigma}{2N}\sum_{i=1}^{N}(x_{i-1} - 2x_i + x_{i+1})dt, \\ \frac{1}{N}\sum_{i=1}^{N} dy_i &= \frac{1}{N}\sum_{i=1}^{N} g_a(x_i)dt + \frac{1}{N}\sum_{i=1}^{N}\sqrt{2D}dW_i, \end{aligned} \tag{84}$$

where the term proportional to the coupling strength σ on the right-hand side of the first equation vanishes for $N \to \infty$.

Introducing new variables

$$x := \frac{1}{N}\sum_{i=1}^{N} x_i, \qquad y := \frac{1}{N}\sum_{i=1}^{N} y_i, \tag{85}$$

we define

$$\frac{1}{N}\sum_{i=1}^{N} dW_i = dW, \tag{86}$$

where dW is the Gaussian white noise as a result of the central limit theorem. It should be noted that the definitions of mean-field variables in Eqs. (85) are different from the previously considered globally coupled case. This is due to the fact that the classical mean-field formalism is not applied here.

The nonlinearity of the function f does not allow us to obtain the exact mean-field limit directly from Eqs. (84). Following Ref. [161] in this case it is possible to approximate the state variables x_i as the Gaussian random variables with expectation x and variance ρ^2 as follows

$$\mathcal{E}[x_i] = \frac{1}{\sqrt{2\pi\rho^2}}\int_{-\infty}^{+\infty} x_i e^{-\frac{(x_i-x)^2}{2\rho^2}} dx_i = x, \quad \mathcal{E}[x_i^3] = \frac{1}{\sqrt{2\pi\rho^2}}\int_{-\infty}^{+\infty} x_i^3 e^{-\frac{(x_i-x)^2}{2\rho^2}} dx_i = x^3 + 3\rho^2 x. \tag{87}$$

This approximation assumes that the excitable system is sufficiently close to the equilibrium point and that the noise intensity D is small.

As a consequence, when $N \to \infty$ we can write the mean-field limit from the average dynamics given in Eqs. (84) as

$$\varepsilon dx = f(x, y)dt - \rho^2 x dt, \qquad dy = g_a(x)dt + \sqrt{2D}dW, \tag{88}$$

where we take into account the law of large numbers [162]

$$\frac{1}{N}\sum_{i=1}^{N} x_i = \mathcal{E}[x_i]. \tag{89}$$

The absence of the coupling term in Eqs. (87) means that there is no coupling effect at the mean-field level. The integration of Eqs. (88) within the mean-field theory framework does not provide any data on ρ. Therefore, the values of ρ are calculated numerically when modeling the neuronal network and entered into each time sample when Eqs. (88) are solved numerically.

It should be noted that for a globally coupled network, the mean-field approach does not require any approximation and provides an accurate description of the mean-field variables. In particular, it provides a set of mean-field variables with the same probability distribution as the neuronal network variables calculated in the infinite limit ($N \to \infty$). In contrast, in the case of a locally coupled neuronal network, the mean-field variables are approximated by random variables distributed according to a Gaussian distribution and represent the mean of the network variables. Thus, for a locally coupled network, the mean-field model is considered, which is an approximation of the averaged network. As a result, the mean-field model in Eqs. (88) will only be successful in a subset of the whole parameter set.

Recently, Baspinar et al. [24] also considered the case of nonlocal connectivity ($1 < P < N$) and concluded that the dynamics of a network of a nonlocally coupled topology cannot be considered as something special, since it can be related to processes occurring in both sparse and highly connected networks. This conclusion is supported by the well-known data for (i) massive networks; when connectivity scales with N, the network behaves as a globally coupled system with a modified coupling constant to account for different fractions of active links [163]; and (ii) sparse networks characterized by constant connectivity not growing with N; the thermodynamic limit shows completely different behavior, typical for locally coupled topology [164]. Taken into account the above issues, we will not dwell here separately on the consideration of CR for the nonlocal topology of the FHN neuronal network.

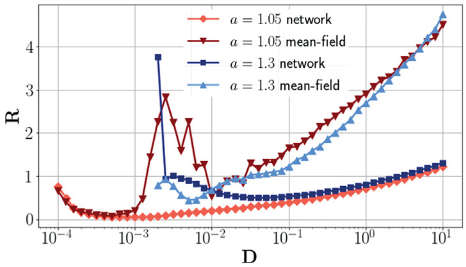

Fig. 18. Standard deviation of ISI R for a locally coupled population of stochastic FHN neurons in both the neuronal network with $P = 1$ given by Eq. (79) and its mean-field system defined by Eq. (88) for fixed coupling strength $\sigma = 0.1$, $N = 100$, $\varepsilon = 10^{-2}$, and varying noise intensity D. Light red diamonds and dark red downward triangles identify, respectively, the network and mean-field results for $a = 1.05$, while dark blue squares and light blue upward triangle identify, respectively, the network and mean-field simulations for $a = 1.3$.
Source: From [24].

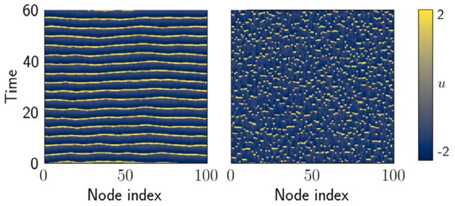

Fig. 19. Spatio-temporal plots representing (left) coherent and (right) incoherent dynamics in a locally coupled network of FHN oscillators subjected to noise.
Source: Based on data from [24].

As in the case of a network of globally coupled neurons, the effect of local coupling is well illustrated by the dependence of the normalized standard deviation R of ISI on the noise intensity, shown in Fig. 18. At low noise intensities $D < 10^{-3}$, there is a good agreement between the results of the mean-field approach and neural network simulation. As the noise intensity increases, the coherence of spike generation increases (R decreases) and a minimum corresponding to CR is observed. However, such agreement is only observed at weak noise. As the noise intensity D further increases to values greater than 10^{-3}, the spike coherence starts to decrease and the mean-field curve no loner overlaps with the curve obtained from the network equations. Such a behavior occurs because we approximate the state variables x and y with Gaussian stochastic processes for low noise intensities to derive the mean-field system, and this approximation does not hold for high noise intensities. In the case of $a = 1.3$, the excitable system is farther from the boundary between excitable and oscillatory regimes compared to the case of $a = 1.05$. This leads to rather incoherent firing of neurons and the Gaussian approximation becomes invalid, that affects mean-field predictions.

Thus, in the case of local coupling, the mean-field approach makes it possible to reproduce the CR effect, but the quantitative correspondence of the R patterns is only observed in a narrow range of the system parameters, when the spike dynamics is coherent and the assumption of Gaussian distribution of variables is valid. Such a behavior differs significantly from the case of a global coupling topology, where the agreement between the results of mean-field theory and network simulation is much better.

4. Coherence resonance in spatially distributed networks of spiking elements

In this section, we systematically analyze the constructive role of noise in spatially distributed networks of spiking elements. We show that an optimal level of noise in these systems results in the appearance of CR which can reveal itself as spatial–temporal pattens, coherent either in time, or in space, or in both.

To illustrate coherent dynamics, spatiotemporal graphs such as those shown in Fig. 19 are often used.

4.1. Spatiotemporal coherence resonance

Spatiotemporal patterns in a nonlinear medium often appear as spiral waves. Such waves were observed in mammalian neocortex [165–167] and cardiac tissue [168,169]. Therefore, spiral waves play an active role in signaling in neuronal systems [167,170]. In addition, the appearance and decay of a spiral wave often indicate an unfavorable course of certain diseases. In particular, spiral wave instability in cardiac tissue can lead to death due to ventricular fibrillation [171,172].

The influence of Gaussian white noise on spatiotemporal dynamics was investigated in various systems, including neural networks modeled by Rulkov maps [135,173], FitzHugh–Nagumo [112,174], Braaksma–Grassman, Jung cellular

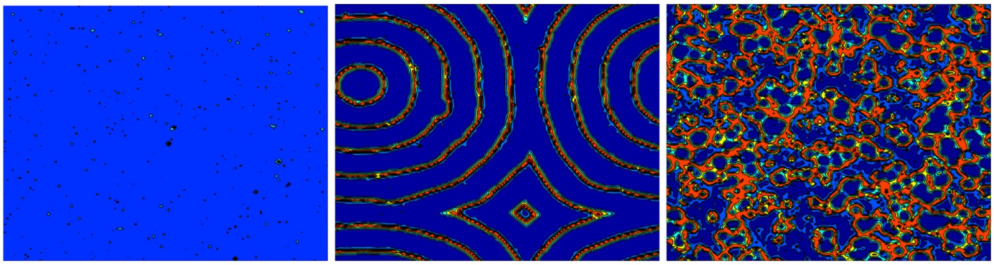

Fig. 20. Spatial wave formation in the square-lattice HH neural network for different noise levels: (left) $\sigma = 0.01$, (middle) $\sigma = 15$, and (right) $\sigma = 60$. All patterns depict values of $V_{i,j}$ on a 128×128 square grid at a given time t. The diffusive coefficient is $D = 0.5$.
Source: Based on data from [175].

automata systems [112], and Hodgkin–Huxley (HH) neurons [175,176]. The results of numerical simulation show that the formation of spatiotemporal patterns in excitable media can be controlled by noise. Moreover, it was found that line waves can be converted into spiral or target waves and can support propagation in neural networks. It was also proved that noise can improve coherence of these waves.

Fig. 20 shows typical spatial $V_{i,j}$ patterns for various noise levels in a 128×128 HH neural network. In the left panel we plot the pattern at a low noise level. Since the neurons do not generate large amplitude peaks, they do not have a pronounced spatial structure. At an intermediate level of noise in space, specific patterns appear that propagate in an orderly manner over the spatial grid in the form of circular waves, as shown in the middle panel in Fig. 20. Obviously, the spatial structures of the circular structure are characterized by layers, with one smaller cycle surrounded by another, larger one. In addition, the number of ordered cycles increases with increasing noise level. A further increase in the noise level leads to the disorder of spatial structures due to random activation of individual neurons. Thus, when the noise level is high enough, ordered circular patterns cannot be maintained and are replaced by disordered random portraits, as shown in right panel of Fig. 20.

Studies of spatiotemporal regularities in the HH neural network with a square lattice with the nearest diffusion connection show that this network contains ordered circular waves with a layered structure at an intermediate noise level. As the noise level is increased, the ordered circular waves deform and eventually transform into random patterns. The spatiotemporal coherence was characterized by the coherence value defined as

$$\beta = H\frac{\omega_p}{\Delta\omega}, \tag{90}$$

where ω_p is the frequency of the main peak in the spectrum, H is the peak height mainly depending on the spectral amplitude, and $\Delta\omega$ is the half-width of the peak, reflecting the temporal randomness of the spectrum. It was observed that the coherence value β increases with increasing diffusive coefficient, that means that the spatiotemporal CR is enhanced.

4.2. Spatial coherence resonance

Spatial CR was discovered by Carrillo et al. [115] for chemical systems near Turing pattern forming instabilities. Then, spatial CR was found in other media, such as neuron networks [28,42,116,177–184], Höfer calcium oscillators [185], prisoner's dilemma game [186], semiconductor structures [187], biochemical [188] and optical [189] media. To reveal spatial CR, the spatial-frequency spectra are analyzed depending on different levels of spatial–temporal noise. In contrast to temporal CR, the spatial CR manifests itself in space, and not in time or spatiotemporal scale of the system. In particular, there is an optimal level of additive noise at which a certain spatial frequency of the system resonates. It should be noted that no additional deterministic actions are introduced into the system initiated from a steady state. Consequently, spatial structures are induced exclusively by additive spatial–temporal noise and reflect spatial periodicity inherent in the media.

Among a variety of media, spatial coherence resonance was found in neural networks. In particular, Sun et al. [42] analyzed the spatial frequency spectra of a network of diffusively coupled HH neurons as a function of different levels of additive noise and the network topology. By calculating the average spatial structural function given by Eq. (46), they found a spatial CR. This means that there is an optimal level of additive noise at which one or another spatial frequency of excitatory events in the neural network is best pronounced. However, in contrast to the results in networks with diffusive nearest-neighbor interactions, small-world networks cannot support coherent patterns of noise-induced spatial excitations and therefore do not guarantee the occurrence of spatial CR.

A two-dimensional lattice of $N \times N$ diffusively coupled HH neurons is modeled as [42]

$$\begin{aligned} C\dot{V}_{i,j} = &- g_{Na}m_{i,j}^3 h_{i,j}(V_{i,j} - V_{Na}) - g_K n_{i,j}^4(V_{i,j} - V_K) - g_L(V_{i,j} - V_L) \\ &+ I^{ext} + \sigma\xi_{i,j}(t) + D(V_{i-1,j} + V_{i+1,j} + V_{i,j+1} - 4V_{i,j}), \end{aligned} \tag{91}$$

where the subscript $i, j = 1, \ldots, N$ denotes each HH neuron in the lattice, σ is the standard deviation of additive uncorrelated Gaussian noise $\xi_{i,j}$, and $D = 0.35$ is the coupling strength. Whereas without adding noise, the neural network

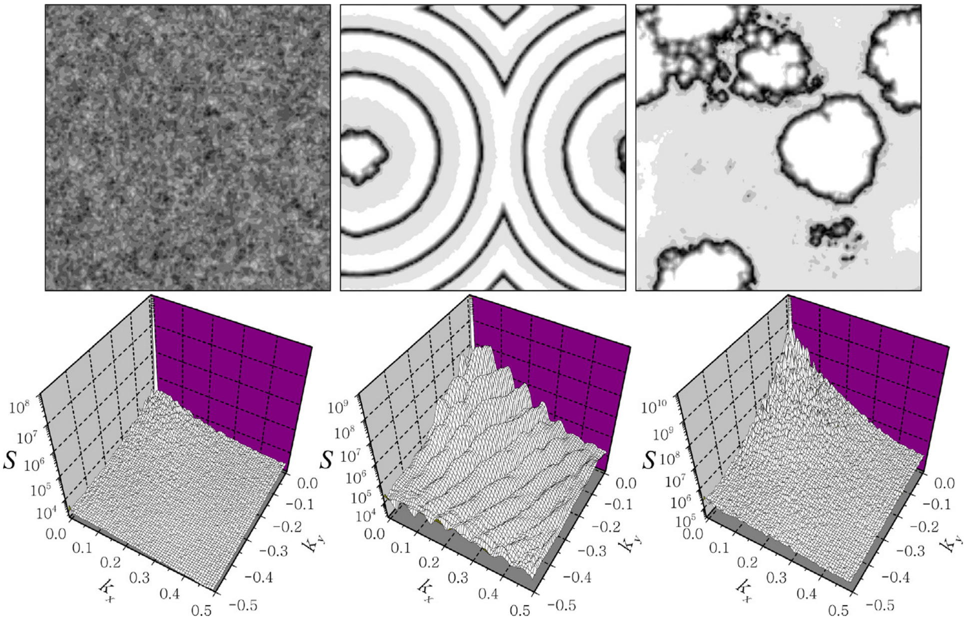

Fig. 21. Illustration of spatial coherence resonance in the network of 128 × 128 diffusively coupled HH neurons. Spatial profile (upper row) and spatial structure (lower row) of $V_{i,j}$ obtained for noise levels (left) $\sigma = 1.1$, (middle) $\sigma = 1.3$, and (right) $\sigma = 1.9$. Spatial dynamics is most coherent at the moderate noise level, exhibiting ordered circular waves propagating through the medium.
Source: Based on data from [42].

remains forever stationary, additive noise of a certain amplitude induces spatial spiral waves in the medium, as illustrated in the upper row in Fig. 21. The spatial structure function calculated by Eq. (48) is presented in the lower row.

The SNR obtained as the peak height of $S(k)$ at k_{max} normalized to the background fluctuations in the system displays a resonance with respect to the noise amplitude σ, that evidences spatial CR. The existence of a resonance of spatial coherence results from the characteristic noise-robust excursion time inherent to all excitable systems. Both the excursion and the diffusion rates determine the spiral wave eigenfrequency which leads to the order enhancement at the appropriate noise intensity. Since internal noise is unavoidable in biological systems, spatial CR is a natural phenomenon in real living systems.

4.3. *Coherence resonance chimeras*

Chimera states are spatiotemporal patterns of synchronous (spatially coherent) and desynchronous (spatially incoherent) behavior of coupled oscillators in complex networks. Spatiotemporal patterns are associated with spatially coherent and incoherent behavior rather than purely temporal coherence or regularity as measured by correlation time. After its discovery in the network of phase generators [109,190], chimeras were found experimentally in electrical networks [191], social systems [192], neural networks [193], and neurophysiological excitable systems [194,195].

Recently, Semenova et al. [196] discovered a new type of CR, which they called *coherence resonance chimeras*. They found that coherent and incoherent spikes alternate between two groups of network elements. To understand the reasons for such a behavior, the time evolution of the coupling for every network node was analyzed in a ring of N nonlocally coupled FitzHugh–Nagumo oscillators described by

$$\begin{aligned} \varepsilon \dot{u}_i &= u_i - \frac{u_i^3}{3} - v_i + \frac{\sigma}{2R} \sum_{j=i-R}^{i+R} [b_{uu}(u_j - u_i) + b_{uv}(v_j - v_i)], \\ \dot{u}_i &= u_i + a_i + \frac{\sigma}{2R} \sum_{j=i-R}^{i+R} [b_{vu}(u_j - u_i) + b_{vv}(v_j - v_i)] + \sqrt{2D}\xi_i(t), \end{aligned} \tag{92}$$

where u_i and v_i are the activator and inhibitor state variables, respectively, $i = 1, \ldots, N$ is the oscillator number (all indices are modulo N, $\varepsilon > 0$ is a time-scale parameter, and a_i is the excitation threshold ($|a_i| > 1$ for excitable and $|a_i| > 1$ for oscillatory element i). All elements are considered to be excitable ($a_i \equiv a = 1.001$), σ is the coupling strength, R is the number of nearest neighbors, and $\xi(t) \in R$ is Gaussian white noise, i.e., $\langle \xi(t) \rangle = 0$ and $\langle \xi(t)\xi(t') \rangle = \delta_{ij}\, \delta(t - t')$, $\forall i, j$,

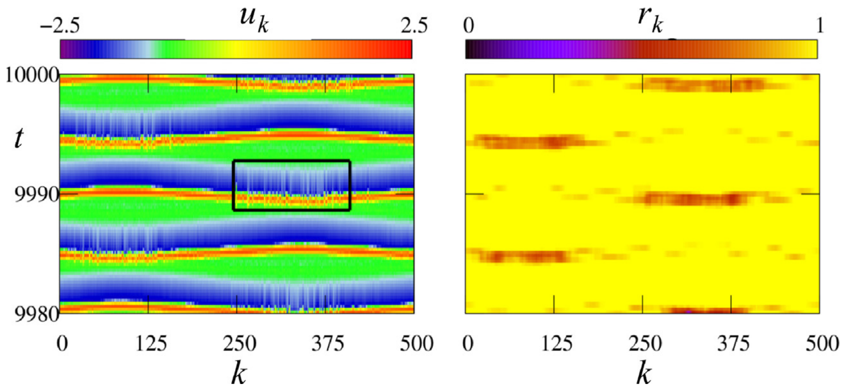

Fig. 22. Coherence resonance chimera in (left) space–time plots and (right) local order parameter of activator u for excitability parameter $a = 0.5$, noise intensity $D = 0.0002$, $R/N = 0.12$, $\sigma = 0.4$, and $\varepsilon = 0.05$. The black box in the left panel marks the counter-propagating excitation wave. *Source:* Based on data from [199].

and D is the noise intensity. The cross couplings between activator u and v variables is depicted by a rotational coupling matrix [197]:

$$B = \begin{pmatrix} b_{uu} & b_{uv} \\ b_{vu} & b_{uv} \end{pmatrix} = \begin{pmatrix} \cos\phi & \sin\phi \\ -\sin\phi & \cos\phi \end{pmatrix}, \tag{93}$$

where $\phi \in [-\pi\ \pi)$. Chimeras were found for $\phi = \pi/2 - 0.14$.

CR chimeras are characterized by the coexistence of two space-separated domains, where one part of the network is spatially coherent and the other shows incoherent spikes, i.e. when spikes of neighboring neurons are not correlated. To quantify the coherence and incoherence for this pattern, the local order parameter r_k was calculated as [198]

$$r_k = \left| \frac{1}{2\delta} \sum_{|j-k|\le\delta}^{N} e^{i\theta_j} \right|, \quad k = 1, \ldots, N, \tag{94}$$

where $\theta_j = \arctan(v_j/u_j)$ (v_j and u_j being the jth oscillator's variables) is the geometric phase. $r_k = 1$ and $r_k < 1$ means coherent and incoherent oscillations of the kth unit. This parameter is similar to that given by Eq. (29).

The chimeric state is shown in Fig. 22 as a spatiotemporal plot, color-coded by the variable u_k (left panel) and the local order parameter r_k (right panel) for noise intensity $D = 0.0002$. One can see the space–time burst pattern that combines the features of chimeric states and coherence resonance, whereas in the excitable mode without noise ($D = 0$), the network is in a homogeneous stationary state and, therefore, no chimeric states arise. In the right panel, it is clearly seen desynchronization islands (dark spots) corresponding to incoherent regions characterized by the order parameter less than unity.

An important feature that distinguishes CR chimeras from deterministic chimeras observed in oscillatory networks is that they appear as partly coherent and partly incoherent excitation waves. The appearance of these waves can be understood by analyzing the propagation and termination of excitation waves in the ring. There are two very fast counter-propagating excitation waves emanated from the incoherent region marked by the black box in the left panel in Fig. 22. These wave become coherent as they propagate, and when they meet again at opposite positions in the ring, they annihilate. Later, at the same position, near $k = 50$, another incoherent domain is born, which again generates two fast counter-propagating coherent excitation waves, and so on.

Another characteristic feature of the stochastic chimera is its alternating behavior, which is absent in the oscillatory regime without noise. Namely, the incoherent domain of the chimeric pattern periodically changes its position in the ring, although its width remains unchanged. It should be noted that strong noise destroys CR chimeras. For instance, with noise intensity $D > 0.000325$, the system in Eq. (92) is incoherent in space, but still very regular, almost periodic in time. However, in the case of stronger noise, i.e., for $D = 0.1$, the system behavior becomes incoherent in time and even more incoherent in space. Thus, CR chimeras appear at intermediate noise intensities, which is a characteristic feature of CR. Because of strong connection of each element with its neighbors, CR chimeras in the network appear at much lower noise intensities than CR in a single system.

Recently, CR chimeras were also found in a small-world network of identical Hindmarsh–Rose neurons subject to α-stable Lévy noise [200]. Taking into account that many real networks have small-world properties with short average path lengths and high clustering coefficients [201], the simulation of such networks allows us to estimate the probability of the appearance of chimera states in real neural networks under the influence of noise. The strength of coherence was used to identified chimera states as follows

$$S(t) = \frac{\sum_{k=1}^{N} \Theta(r_k)}{N}, \tag{95}$$

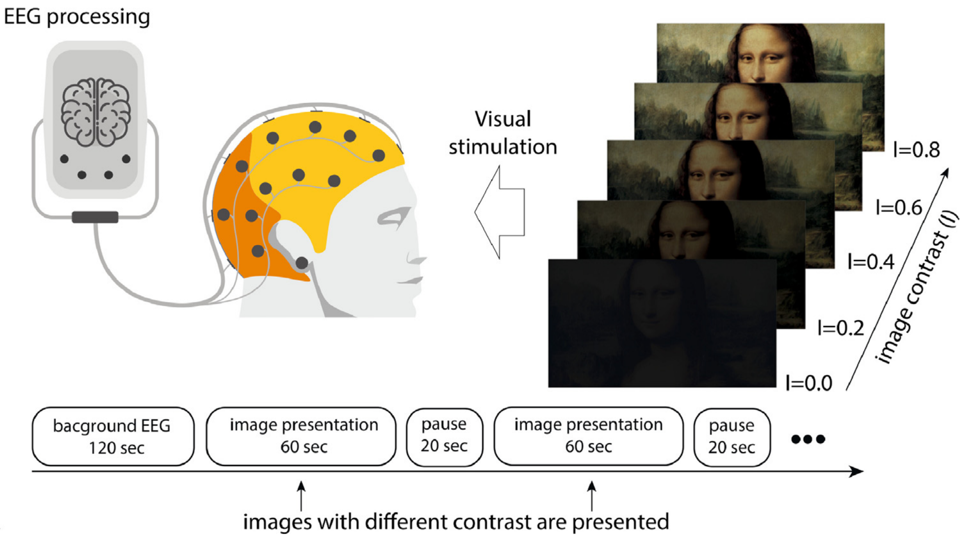

Fig. 23. Experimental design for detecting coherence resonance in the brain network using Mona Liza portraits with different contrast level I.

where r_k is the local order parameter of the kth neuron at time t calculated with Eq. (94) and $\Theta(r_k)$ is the indicator function of coherence defined as

$$\Theta(r_k)=\begin{cases}1, & \text{if } r_k>1-10^{-4},\\ 0, & \text{if } r_k\le 1-10^{-4}.\end{cases} \tag{96}$$

$\Theta(r_k)=1$ and $\Theta(r_k)=0$ indicate coherence and incoherence, respectively. Therefore, $S(t)=1$ and $S(t)=0$ mean that all neurons are coherent and incoherent, respectively. If $0<S(t)<1$, then the system is in a chimera state at time t; higher $S(t)$ means that a larger number of neurons belong to the coherence group.

4.4. Coherence resonance in distributed cortical networks

The brain is known to dynamically adapt the functional neural network structure to improve the sensory processing efficiency as cognitive demands increase [202,203]. This mechanism implies that conscious perception requires coherent activity of several distributed brain areas [204,205]. The problem of the emergence of neural connections between remote brain areas are widely discussed in the scientific literature. There are several theories which attempt to explain how neural ensembles interact in the brain. Specifically, Fries [206] suggested that neural communication is supported by neural coherence. According to his theory, activated groups of neurons interact during those periods of time when they are coherent. In addition, it was concluded that neural communication occurs simultaneously in different frequency ranges and requires coherence. This effect referred to as "communication through coherence" (CTC) implies that a group of postsynaptic neurons, receiving information from several presynaptic groups, first responds to the group with which it is more coherent. In the absence of coherence, inputs arrive at random phases of the excitability cycle and therefore have very low coupling efficiency.

Coherence is significant for communication between brain regions [207]. Moreover, neural communication can be significantly improved by CR occurring in a neural network at a certain noise level [8]. It was hypothesize that the brain adjusts the size of the active neural network according to cognitive needs in order to increase SNR. Although CR in neural networks was predicted by numerical simulations of various neural models, its detection in the real brain neural network provided the experimental evidence of this hypothesis.

Numerical results described above predict that intrinsic neural noise causes a resonant behavior of the stimulus-related brain response at the external signal amplitude slightly above the neural excitation threshold. To check if CR really exists, the EEG experiments with visual stimuli were carried out. Specifically, the subjects were presented with Mona Lisa images with different contrast $I\in[0,1]$. The experimental design is shown in Fig. 23.

An increase in the image contrast is associated with growing noise intensity I^{ext} in the model Eq. (71). This causes an increase in the firing rate of neurons in visual cortex [208–211]. Then, the brain network coherence was estimated using both the correlation time of EEG signals (time coherence) and brain connectivity (topological coherence). Let us show how these values were measured experimentally.

Assuming that longer correlation time means higher coherence and basing on the results of numerical simulations, it is supposed that the correlation time has a local maximum when I passes the perceptual threshold. Accordingly, the global network coherence can be defined as the number of EEG signals showing the maximum correlation time for a

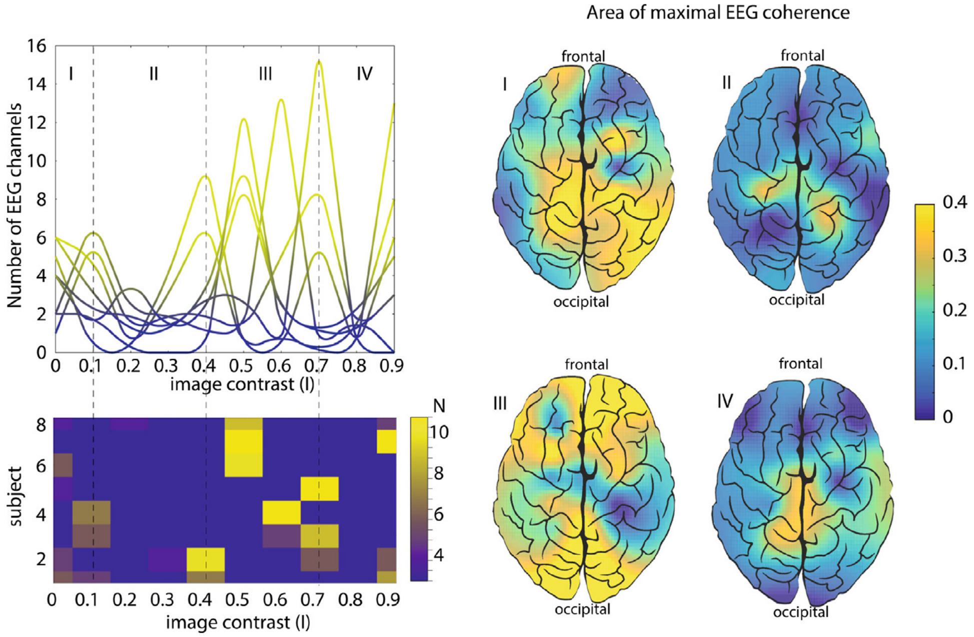

Fig. 24. Experimental results demonstrating coherence resonance near perception thresholds. (Upper left) Number of EEG channels with maximal correlation time versus image contrast for different subjects (each curve corresponds to one participant in the experiment). The most local maxima are concentrated in areas I and III corresponding to image recognition and portrait identification, respectively. (Lower left) Distributions of the coherent channel among participants. (Right panels) Brain coherence for different image contrasts: (I) $I = 0.1$, (II) $I = 0.4$, (III) $I = 0.7$, and (IV) $I = 0.8$ for one typical subject.

given contrast level I. Thus, the global coherence of a neural network can be defined as the number of EEG channels that demonstrate the maximum correlation time for a given image contrast. The dependence of the number of channels on the image contrast is presented in Fig. 24, where different curves refer to different subjects. One can see that the global coherence of the network maximizes at low ($I < 0.1$) and average $0.3 < I < 0.7$ contrast values. Thus, while observing this image, the perception passes through two thresholds, a low threshold corresponding to perception of Mona Liza silhouette only, and a high threshold associated with detailed recognition of facial features and background.

Therefore, the number of active EEG channels is a good indicator of the brain coherence. The dependence of this indicator on the image contrast is shown in the upper left graph in Fig. 24, where different curves correspond to different subjects. One can see that the global network coherence (in number of channels) has at least two local maxima, at low ($I < 0.1$) and at middle ($0.3 < I < 0.7$) contrast levels. The distribution of the number of channels among participants is presented below.

The first local coherence maxima is observed in region I for all participants in a narrow range of the image contract. This maximum corresponds to neural coherence caused by the low perception level of the Mona Lisa silhouette only. The second (global) maximum occurs in region III, where the maxima for different subjects are distributed over a wide range of I. The difference in the position of the global maximum for different subjects can be explained by the difference in their individual brain noise levels. Since the contrast in region III is higher that in region I and II, the participants receive a significant amount of visual information and can already recognize more finite details of the image that causes sharp peaks in the global network coherence. The higher peak amplitude in region III means that the larger size of the neural network involved in sensory processing, especially frontal and occipital–parietal cortex (see the brain images in the right-hand side in Fig. 24). For other regions, where the contrast values are smaller (region II) and higher (region IV) than I in region III, the distributed brain structure is not excited and sensory processing engages the visual cortex.

Since coherence is a key mechanism of neural communication, we hypothesize that an increase in coherence in the frontal and occipital–parietal areas contributes to their effective interaction in different frequency ranges. To prove this hypothesis, the brain network was reconstructed from multidimensional EEG signals using wavelet bicoherence. This approach allows finding functional connectivity between different brain areas by analyzing synchronization between corresponding EEG signals in certain frequency bands.

Brain connectivity can be revealed by analyzing EEG data using continuous wavelet transform. For each time series $x_p(t)$ from pth electrode, the wavelet energy spectrum was calculated in the frequency range $f \in [0, 30]$ Hz as follows

$$E^p(f,t) = \sqrt{f\left(\int_{t-4/f}^{t+4/f} X_p(t)\psi^*(f,t)dt\right)^2}, \tag{97}$$

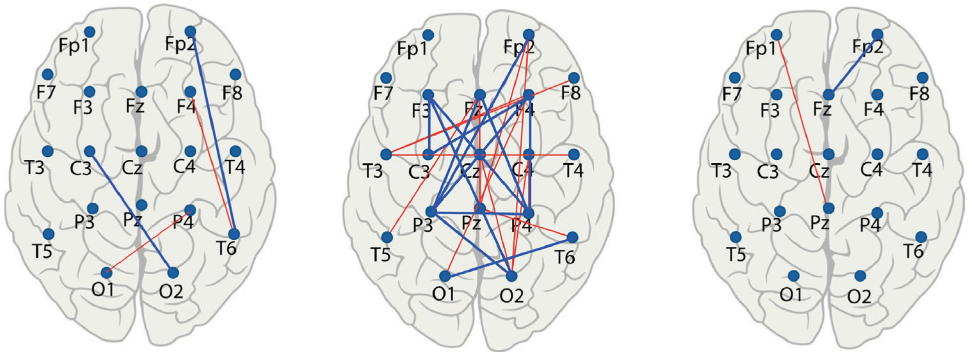

Fig. 25. Structural CR in functional brain connectivity in alpha (8–12 Hz; red links) and beta (15–30 Hz; blue links) bands for image contrasts: (left) $I = 0.1$, (middle) $I = 0.4$ (middle), and (right) $I = 0.7$. The link strengths are calculated via wavelet bicoherence.

where $\psi(f,t)$ is a mother wavelet function and "*" denotes complex conjugation. As a mother wavelet function, we choose the Morlet wavelet, often used for the analysis of neurophysiological data, defined as

$$\psi(f,t)=\sqrt{f}\pi^{1/4}e^{j\omega_0 f(t-t_0)}e^{f(t-t_0)^2/2}, \tag{98}$$

where $\omega_0 = 2\pi$ is the wavelet parameter and t_0 is the shift of the wavelet along the time axis.

To measure the interaction between every two EEG channels ($x_p(t)$ and $x_q(t)$), wavelet bicoherence were used. For this aim, the following complex wavelet coefficients were considered

$$W_p(f,t)=a_p(f,t)+ib_p(f,t) \quad \text{and} \quad W_q(f,t)=a_q(f,t)+ib_2(f,t), \tag{99}$$

and the corresponding signal phases were calculated as

$$\phi_p(f,t)=\arctan\frac{b_p(f,t)}{a_p(f,t)} \quad \text{and} \quad \phi_q(f,t)=\arctan\frac{b_q(f,t)}{a_q(f,t)}. \tag{100}$$

Next, the relative phase difference

$$\Delta\phi(f,t)=\phi_q(f,t)-\phi_p(f,t) \tag{101}$$

was obtained and the following coefficients

$$\cos\Delta\phi(f,t)=\frac{a_p(f,t)a_q(f,t)+b_p(f,t)b_q(f,t)}{\sqrt{a_p^2(f,t)+b_p^2(f,t)}\sqrt{a_q^2(f,t)+b_q^2(f,t)}}, \tag{102}$$

$$\sin\Delta\phi(f,t)=\frac{a_q(f,t)b_p(f,t)-a_p(f,t)b_q(f,t)}{\sqrt{a_p^2(f,t)+b_p^2(f,t)}\sqrt{a_q^2(f,t)+b_q^2(f,t)}} \tag{103}$$

were found. These coefficients are averaged over a full length of each ith stimulus presentation ($\tau_i = 60$ s). Finally, the coefficients for ith stimulus were derived as

$$\cos\Delta\phi(f,t)_{\tau_i}=\int_{\tau_i}\cos\Delta\phi(f,t)dt \quad \text{and} \quad \sin\Delta\phi(f,t)_{\tau_i}=\int_{\tau_i}\sin\Delta\phi(f,t)dt, \tag{104}$$

and the degree of coherence between every pair of EEG signals was calculated during ith stimulus presentation as the mutual wavelet spectral amplitude

$$\sigma(f)_{\tau_i}=\sqrt{\cos^2\Delta\phi(f,t)_{\tau_i}+\sin^2\Delta\phi(f,t)_{\tau_i}}\in[0,1]. \tag{105}$$

When $\sigma(f)_{\tau_i}=0$, no phase coherence exists between the signals at frequency f, otherwise, the coherence takes place.

Then, the values of $\sigma(f)_{\tau_i}$ are averaged over α (8–12 Hz) and β (15–30 Hz) frequency bands. Finally, the coherence between every pair of EEG signals during visual perception was calculated in the α and β frequency bands as

$$\sigma_{\tau_i}^{\alpha,\beta}=\int_{\alpha,\beta}\sigma(f)_{\tau_i}df. \tag{106}$$

The results of the brain connectivity are depicted in Fig. 25, where we show functional connections between different brain areas in regions II–IV in alpha (red) and beta (blue) bands. One can see that in both frequency bands, the maximum number of links occur in area III (middle image), i.e., the network size exhibits structural CR when the number of links and their weights are maximized, especially between frontal and parietal areas. Thus, these results confirm our hypothesis that stronger brain noise is associated with larger neuron network involved in information processing.

Thus, experimental and theoretical studies provide substantial evidence for the positive impact of brain internal noise on sensory processing efficiency and cognitive function. At the same time, intrinsic brain noise not only enhances the neural response in certain brain areas, but also provides pathways for neural communication between distant areas. In this context, this study bridged the gap between the neural noise paradigm and neural communication theories, communication through coherence and global workspace theory. These results are supported by other studies showing that efficient visual information processing requires an increase in the neural network size. In addition, enhancing coherence is achieved due to CR, supported by the presence of neural noise.

Despite significant progress in studying neural network coherence, in particular, the formation of brain connections through CR, some coherence measures require further investigation, for instance, the use of network entropy for characterization of structural CR.

5. Experimental approaches to brain noise estimation

The brain, like any other biological system, is a very noisy system. Random neuronal activity results either from internal physiological neuronal or from external sources which affect our perception. The former is called *endogenous* brain noise, while the other is known as *exogenous* brain noise. Stochastic processes in the neural network can have various origins, such as probabilistic random spontaneous neural activity, random synaptic connections, etc. [139,212]. All these random oscillations can be distinguished in EEG, MEG, and other brain imaging recordings.

Among many sources of neural noise, we have to mention the quasi-random release of neurotransmitters by synapses, random synaptic input from other neurons, and random switching of ion channels. Noise in the neural network can appear when connections between neurons are weakened or blurred as a result of reduced branching, loss of neurons, or periodic inhibition. Neural noise can be considered in comparison to the signal strength for relevant or actively processed information; the nervous system is noisy if the ratio of signal strength to random background noise is low. Too much and too little brain noise can be the result of some mental illnesses such as autism and schizophrenia, respectively. In addition, brain noise changes with age, as well as a result of neurodegenerative diseases such as Alzheimer disease [213]. Therefore, it is extremely important to have the instrument for measuring brain noise. On the other hand, noise can have a beneficial effect on the nervous system; it is necessary for its normal functioning at all levels of organization, from cells to the brain.

5.1. Brain noise estimation based on steady-state visual evoked field

Brain noise can be estimated from experimental data. For this purpose, special approaches were developed to assess brain noise from EEG and MEG recordings [142]. Numerous data on neurophysiological activity indicate the presence of a fairly strong stochastic component, or $1/f$ noise, in the power spectrum [214,215]. Neuronal noise is defined as random background electrical fluctuations in the central nervous system [216–218]. Noise of an individual neuron affects dynamics of other neurons in neural ensembles. However, it is clear that neural networks can maintain stable activity in the presence of noise. This property is determined by several mechanisms that control the overall level of noise in the network. If input signals from presynaptic neurons have independent noise, then the noise level in the postsynaptic neuron will change in proportion to the square root of the number of signals, while the signal itself changes in proportion to the total number of neurons N in the network. If noise in the signals is perfectly correlated, then neural noise will also change in proportion to N. This allows us to draw an important conclusion that the involvement of a large neural ensemble in information processing should lead to an increase in the noise level that will be recorded in such an ensemble.

An efficient method for assessing neurocerebral noise is based on frequency locking of the brain response to a periodically modulated stimulus [219]. As is known from the theory of coupled oscillators [91], frequency capture occurs in a stochastic or chaotic system, which is acted upon by a periodic external force. Frequency blocking can be continuous or intermittent depending on both the strength of the external force and the noise intensity. In the intermittency regime, the frequency locking windows are interrupted by unlocking periods at a phase shift of $2\pi n$ radians ($n = \pm 1, \pm 2, \ldots$). At the same time, in the frequency-locking regime the oscillation phase is not completely synchronized, but fluctuates around the average value due to noise. Therefore, the amplitude of the phase fluctuations is related to the internal brain noise. The stronger the noise, the greater the amplitude fluctuations.

The experimental technique for assessing brain noise was as follows. Participants were presented with a flickering visual stimulus with frequency $f_s = 6.67$ Hz with simultaneous recording of a magnetoencephalogram (MEG). Because the flicker frequency is high enough to prevent the evoked neuronal activity from returning to its original state, the evoked response is continuous. In the case of MEG, this response is called the steady-state visual evoked field (SSVEF). Spectral analysis shows that the greatest SSVEF response falls on the second harmonic of the flicker frequency, i.e. at $2f_s = 13.34$ Hz. As is known from the theory of synchronization, noise in a system of coupled stochastic or chaotic oscillators leads to their desynchronization, which can be detected by fluctuations in the phase difference of the coupled variables. Since the strongest brain response occurs at the second harmonic of the flicker frequency, the phase difference between SSVEF and the second harmonic of the stimulation signal can be found as

$$\Phi = \left(t_n^b - t_n^s\right) 2f_s, \tag{107}$$

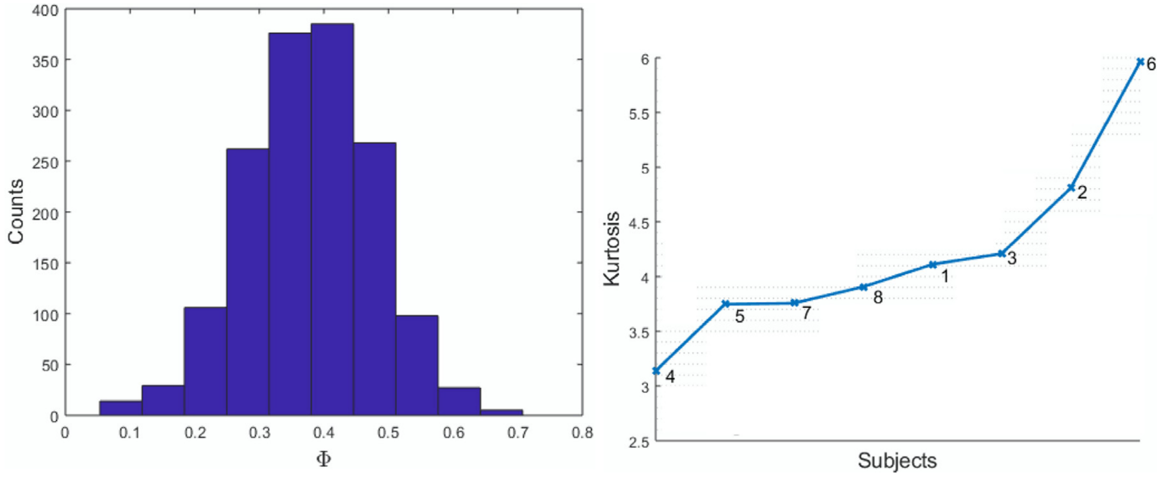

Fig. 26. (Left) Probability distribution of SSVEF phase fluctuations for subject 4 and (right) kurtosis for eight subjects. The subjects with higher kurtosis have lower brain noise.

where t_n^b and t_n^s are the positions in time of the nth maximum of the brain response (SSVEF) and the second harmonic of the flicker signal, respectively.

SSVEF phase fluctuations in time windows where the phase is locked are used for statistical analysis. Fig. 26 shows the example of probability distribution of these fluctuations and kurtosis for eight participants, whose kurtosis was calculated as

$$K = \frac{E(\Phi - \langle\Phi\rangle)^4}{\sigma^4}, \tag{108}$$

where $\langle\Phi\rangle$ is the average phase difference, σ is the standard deviation, and E is the function of the expected value.

In physics, noise is considered as a random stochastic process which exhibits probabilistic properties, such as, e.g., Gaussian distribution. However, in mathematics, there are deterministic dynamical systems whose dynamics obeys the same statistical laws as stochastic systems, for instance, deterministic Brownian motion [220–222]. It is assumed that noise is associated with wider phase probability distribution and, therefore, with inverse kurtosis. This means that stronger noise broadens the probability distribution and hence decreases kurtosis. Experimentally recorded neural noise results from random neurophysiological activity of the neural network, while attentional noise leads to the interruption of frequency locking. Because each person's neural network is unique, knowing the noise can be useful for designing efficient brain–computer interfaces that can be adapted to the subject's brain noise.

5.2. Brain noise estimation based on psychometric functions

An alternative approach to estimating perceptual brain noise is based on the measurement of psychometric functions which describe stimulus/response relationships. Psychologists are well aware how perception can be quantified. A graph showing the response of a subject perceiving a stimulus as a function of the level, intensity, or type of stimulus is called a *psychometric function*. The psychometric function can serve as an effective characteristic for estimating stochastic characteristics of neural responses recorded by human behavior in response to some stimulus.

Psychometric functions can have different forms, but the most common and interesting one is the sigmoid-like curve which represents the observer's behavior near the perceptual threshold. This is because the transition from one response to another (e.g., "can't tell" to "can tell") is not instantaneous. Because neural responses are variable [223,224], the subjects do not give the same response to every stimulus. The sigmoid-shaped psychometric curve is characterized by the following parameters.

- The *ceiling* is the best performance for the most distinguishable stimuli. Sometimes this score is not 100% because people make mistakes when answering (e.g., they accidentally press the wrong button on the keyboard).
- The *floor* is the worst performance. If you do a two-alternative forced-choice task (2AFC) [225], the worst a subject can do is the 50% they could get by guessing. If you do a simple yes/no task (present the stimulus in each trial, and participants say "yes" if they detect it), the floor is 0%.
- The *middle* is the most interesting part. This is where the subject begins to detect change, but not always. You determine the threshold by choosing a performance criterion (e.g., 75% correct answers); the threshold is the value of the stimulus (intensity or difference) that resulted in criterion performance.

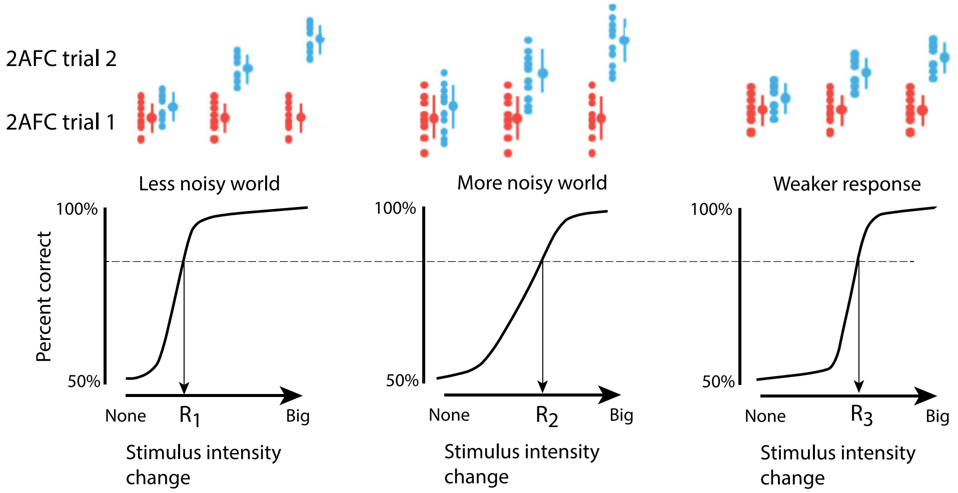

Fig. 27. Detection thresholds are reached when stimulus-induced response changes are large compared to the variability in the response. Here $R_1 < R_2 = R_3$.
Source: Adapted from [228].

One of the things we can learn from the psychometric function is whether a person's detection/discrimination threshold is high because the average neural response to a stimulus is weak or because there is great variability in the response. Thresholds are higher when the response is not very dependent on the stimulus. Thresholds are also higher when responses are very variable — even big changes cannot be reliably detected. The slope of the psychometric function (for one level/type of stimulus) indicates the level of neural noise or variability in responses. Therefore, when comparing different groups of subjects, if one has higher thresholds than the other, we can use the slope to determine whether this difference is due to a decrease in response amplitude or an increase in noise [226,227].

Fig. 27 illustrates what was said above using the example of the 2AFC task. The left panel shows the psychometric function in the case of low perceptual noise with a low detection threshold R_1. The next two panels show two situations with a high detection thresholds $R_2 = R_3 > R_1$, which are nevertheless are caused by different reasons – a decrease in the response amplitude or an increase in the noise amplitude. In the first case, just-noticeable difference (JND) increases, since the response changed more slowly, in the second case, the growth of JND is determined by the fact that responses were noisier. As a result, in the second case, the slope of the psychometric curve is much less than in the first case.

Thus, the approach based on a combination of neuroimaging methods at the level of large populations of neurons (e.g., measured with optical imaging, EEG/MEG or functional magnetic resonance imaging) and psychophysical methods at the level of behavioral performance (e.g., measured by experimentally constructing psychometric functions) provides an effective tool for a comprehensive study of the impact of noise and the phenomenon of CR on a person at the level of his reaction to certain stimuli. Moreover, in many cases, it is possible to limit noise assessment to psychophysical studies, which are usually much simpler and cheaper than neuroimaging studies.

Let us describe the experimental technique for estimating brain noise based on psychometric functions. The method is centered on peculiarities of the human brain activity related to the interpretation of ambiguous images. The main idea of the method is as follows. Ambiguous images with different degree of ambiguity were presented to participants of the experiment. In particular, Runnova et al. [142], used an experimental paradigm with an ambiguous bistable visual stimulus in the form of the Necker cube, which allows two possible interpretations. Obviously, the images with a weak degree of ambiguity are interpreted always in the same way, whereas the images with a high degree of ambiguity are interpreted in two different ways and hence can be considered as a typical two-alternative forced choice (2AFC) task. Then, the psychometric function can be measured by presenting the subject with many images with varying contrast parameter I and measuring probability P of choosing one or another (left-oriented or right-oriented) interpretation of the bistable image.

During the experiments, the Necker cube images with $N = 16$ degrees of ambiguity $\Delta I_i = I_i - I_0$ with different contrast parameters $I_i = i/(N-1)$ ($I_0 = 0.5$, $i = 0, \ldots, N-1$) (Fig. 28(a)) were repeatedly presented 750 times to subjects in a random sequence on the computer screen. The subjects were instructed to press either a left or a right key on the control panel according to their first visual impression (left-oriented cube or right-oriented cube). For each value I_i of the contrast parameter the probability $P_r(I_i)$ of the right-oriented cube (right key choice) was calculated as

$$P_r(I_i) = \frac{r(I_i)}{r(I_i) + l(I_i)}, \tag{109}$$

where $r(I_i)$ and $l(I_i)$ are the numbers of clicks on the right and left keys, respectively.

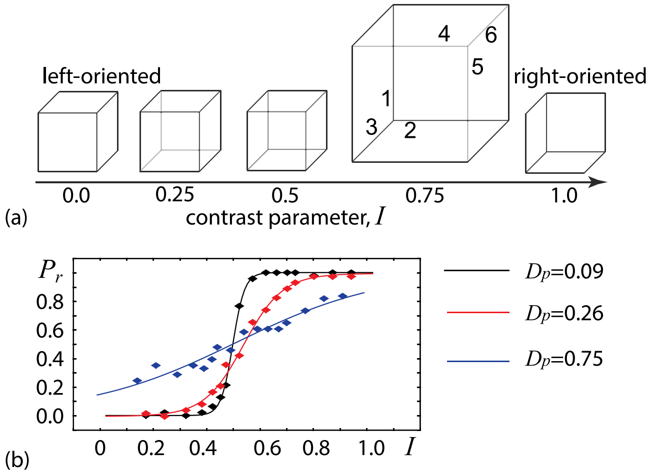

Fig. 28. (a) Examples of visual stimuli (Necker cubes) with different values of the contrast parameter I, which determines the cube orientation and the degree of ambiguity. The subjects without perceptual impairments interpreted this two-dimensional image as a three-dimensional cube oriented either to the left or to the right. The balance between the brightness of three inner lines (1,2,3) located in the lower left corner and three inner lines (4,5,6) in the upper right corner determines the ambiguity and orientation of the 3D cube. The contrast parameter $I \in [0, 1]$ reflects the normalized brightness of the inner lines (1,2,3) in the grayscale palette, while the normalized brightness of the remaining inner lines (4,5,6) is defined as $(1 - I)$. Thus, the boundary conditions $I = 0$ and $I = 1$ correspond to unambiguous 2D projections of the cube, oriented respectively to the left or to the right, whereas $I_0 = 0.5$ implies a completely ambiguous spatial orientation of the 3D cube image. (b) Experimentally measured psychometric functions as probability P_r of perceiving a right-oriented image of the Necker cube through contrast parameter I, obtained for three typical subjects (shown by dots) and corresponding theoretical approximations $\hat{P}_r(I)$ (shown by solid curves). Using the least squared method, the values of effective noise intensity D_p associated with the individual bistable perception energy function are determined.

Fig. 28(b) shows the psychometric functions obtained for three subjects. The difference in the slopes of the curves indicates that each subject's brain has a different level of neural noise. Thus, brain noise can be quantified.

The perception of an ambiguous image leads to discontinuity in its interpretation. For example, a symmetric Necker cube ($I_0 = 0.5$) is perceived either as a left- or right-oriented cube. Such an alternation of two possible interpretations of the ambiguous stimulus indicates that the system is close to the cusp catastrophe [229]. In particular, a bistable system can be described by a dimensionless potential energy function with two local minima $x_{l,r}$ [230]:

$$U(x) = \frac{x^4}{4} - \frac{x^2}{2} + \frac{\Delta I}{\alpha} x \tag{110}$$

with α being the scaling factor determined by individual features of the double-well potential function and the dimensionless firing rate x of the neuronal population given by

$$\dot{x} = -U'(x) + \xi(t), \tag{111}$$

where $\xi(t)$ is zero-mean δ-correlated Gaussian noise with $\langle \xi_n \rangle = 0$ and $\langle \xi_n \xi_m \rangle = D\delta(n - m)$ (D being the noise intensity).

The addition of noise in Eq. (111) results in the stochastic differential equation

$$dX = -U'(x)\,dt + dW, \tag{112}$$

where $X(t)$ and $W(t)$ describe stochastic and one-dimensional Winner processes, respectively. The probability density $\rho(x, t)$ of the stochastic process $X(t)$ can be modeled using the Fokker–Planck equation

$$\frac{\partial \rho_X(x, t)}{\partial t} = \frac{\partial}{\partial x}[U'(x)\rho_X(x, t)] + \frac{D}{2}\frac{\partial^2 \rho_X(x, t)}{\partial x^2}. \tag{113}$$

Since stationary probability density $\rho(x)$ being the solution of Eq. (113) is time independent, Eq. (113) can be reduced to the following ordinary differential equation (ODE)

$$\rho'(x) + \frac{2}{D}U'(x)\rho(x) - C = 0, \tag{114}$$

where C is an unknown constant.

To solve the inhomogeneous ODE Eq. (114), the homogeneous ODE is considered

$$\rho'(x) + \frac{2}{D}U'(x)\rho(x) = 0, \tag{115}$$

whose solution is known to have the following form

$$\rho(x) = B(x) \exp\left(-\frac{2}{D}U(x)\right). \tag{116}$$

Having substituted Eq. (116) for $\rho(x)$ into Eq. (114), we obtain the ODE for the unknown function $B(x)$ as

$$B'(x) = C \exp\left(\frac{2}{D}U(x)\right), \tag{117}$$

whose solution can be found in the form

$$B(x) = C\int_0^x \exp\left(\frac{2}{D}U(z)\right) dz + A, \tag{118}$$

where A is a constant. Finally, from Eqs. (116) and (118) we obtain the general form of the stationary probability density $\rho(x)$ being the solution of the Fokker–Planck Eq. (113) as

$$\rho(x) = \exp\left(-\frac{2U(x)}{D}\right)\left[A + C\int_0^x \exp\left(\frac{2U(z)}{D}\right) dz\right]. \tag{119}$$

Having found the constant C from the extremum condition

$$\rho'(x_{l,r}) = C = 0, \tag{120}$$

we obtain the final form for the stationary probability density function as

$$\rho(x) = A\exp\left(-\frac{2U(x)}{D}\right), \tag{121}$$

where A is determined by the normalization condition

$$\int_{-\infty}^{+\infty} \rho(x)\, dx = 1. \tag{122}$$

In the case of a symmetric ambiguous stimulus, such as the Necker cube, the probability for a person to perceive one of two possible interpretations, for example, right orientation, can be found as

$$\hat{P}_r = \int_0^{+\infty} \rho(x)\, dx, \tag{123}$$

where $\hat{P}_r(\varDelta I, \alpha, D)$ is determined by parameters $\varDelta I$, α, and D. Fixing α and D and using $\varDelta I$ as a control parameter, one can calculate probability $\hat{P}_r(\varDelta I, \alpha, D)$ to perceive the right-oriented cube and compare it with the experimental psychometric function given by Eq. (109). The values of α and D in Eq. (123) can be found using the least square technique for the minimum error value

$$E(\alpha, D) = \sum_{j=1}^{N}\left[P_r(\varDelta I_j) - \hat{P}_r(\varDelta I_j, \alpha, D)\right]^2. \tag{124}$$

As was shown in Ref. [142], the minimum error $E_{\min}$ corresponds to the best coincidence of theoretical and experimental results. This curve found empirically was approximated by

$$\alpha D = D_p = \text{const.} \tag{125}$$

In other words, the parameter D_p is actually a universal invariant providing the minimum value $E_{\min}$ of the error surface $E(\alpha, D)$. Accordingly, the value of D_p can be interpreted as the effective noise intensity associated with the individual double-well potential function $U(x)$ defined by Eq. (110). The effective noise intensity D_p can easily be determined from the psychometric function using the least square method and should be considered as closely related to the individual characteristics of human perception. The results of comparison of experimental and theoretical studies are illustrated in Fig. 28(b). One can note the excellent agreement between theoretically predicted and experimentally obtained data.

5.3. External coherence resonance

In the psychometric function problem, we measure endogenous brain noise, as opposed to the standard stochastic/coherent resonance research problem in neuroscience, where we study the response of the nervous system to noisy sensory input from the environment (i.e., external noise). In neuroscience, this situation is often referred to as *external coherent resonance* (ECR). However, it overlooks the important point that at every level of the nervous system (from molecular and cellular to behavioral) there is a significant amount of endogenous noise, even in the absence of an external noise source. As we mentioned earlier in this review with the example of visual perception (see Section 5.2), such endogenous noise can contribute to CR [8]. In addition, a number of theoretical works with neural models suggest that internal noise can improve transmission in neural networks [231,232]. The complexity of such studies lies in the fact that there is no way to control the level of endogenous noise and hence to evaluate the measure of coherence as a function of noise intensity (see Fig. 1). Therefore, new approaches based on the concept of stochastic facilitation are needed to be able to establish the correct hypothesis and choose an adequate measure of CR in a living system (following Section 6.1 and Fig. 30).

On the other hand, the coherent/stochastic resonance effects in psychophysical studies are not always well pronounced, although they are significant from a statistical point of view. For example, the CR effect in visual perception, measured by a decrease in the contrast threshold, is about 2 dB [233], and the noise-induced enhancement in hearing is no more than 4% [234]. Due to such minor changes observed when averaging over a group of subjects, it is possible that some of the subjects (sometimes up to half of the entire group [235]) do not exhibit ECR. In this regard, the question arises of what determines the fact of observing ECR in each of the subjects. Aihara et al. [236] suggested that the appearance/absence of ECR is determined by the subject's endogenous brain noise level. ECR does not occur at strong endogenous noise because its level is already equal or even higher than the optimal value for CR observation, so the addition of an external noise source only worsens the efficiency of CR detection.

Aihara and coauthors [237] tested this hypothesis with a visual detection experiment. In their psychophysical experiment, the subjects viewed two images on a monitor through a mirror stereoscope used to merge the two images, each of which was presented separately to the left and right eyes. Time-varying gray level signals and external noise were presented to the right and left images, respectively. The subjects were asked to press a button when they detected a signal in the fused image. To assess the overall (i.e., internal plus endogenous) noise level in the brain, the psychometric function was used that relates the hit rate to the signal level; the term 'hit' indicates that the subject responds correctly when the stimulus contains the cue. In this study, the psychometric function $P(x)$ was empirically described by the cumulative Gaussian distribution function:

$$P(x) = \frac{1}{\sqrt{2\pi}\,\beta} \int_{-\infty}^{x} \exp\left(-\frac{(s-\alpha)^2}{2\beta^2}\right) ds, \tag{126}$$

where the mean α and standard deviation β are called the threshold and spread parameters, respectively.

According to Faisal et al. [224], trial-to-trial variability may be related to endogenous noise, and the resulting spread reflects the overall level of brain noise. The authors of Ref. [237] showed that the spread averaged over all subjects is a monotonically increasing function of external noise levels, which confirms the assumption that the spread reflects the total noise level, which means that the spread in the absence of external noise can be associated with internal noise. In fact, the spread in the external-noise-free condition (i.e., a measure of the internal noise level) is negatively correlated with the ECR effects, supporting the hypothesis that the higher the level of internal noise, the less likely it is that external noise will improve signal detection through ECR. At the same time, the classical psychometric function in Eq. (126) is insufficient in the sense that the function has only one variable — the stimulus level, and does not take into account the influence of noise (internal, endogenous, or both). Aihara et al. [236] proposed a psychometric function as a bivariate function of signal and external noise intensity to describe the CR effects.

The noise effect y can be incorporated into α and β parameters of the psychometric function given by Eq. (126) as

$$\alpha = a\beta \exp\left(\frac{b^2}{2\beta^2}\right), \tag{127}$$

$$\beta = cy + d, \tag{128}$$

where a, b, c, and b are adjustable positive parameters. Eq. (127) is derived from the CR/SR threshold theory. Differentiating Eq. (127) with respect to b and equating the value of the differential to zero, we find that the threshold α has a local minimum at $\beta = b$, i.e., the parameter b is related to the optimal noise level for CR. The external noise effect on the spread Eq. (128) is described empirically based on the experimental observation [237] that the spread β depends approximately linearly on the external noise level y. Setting $y = 0$ in Eq. (128) yields $d = \beta$, indicating that the parameter d represents the spread in the absence of external noise. As a consequence, d reflects the intensity of rather internal than external noise. So, the proposed bivariate psychometric function $P(x, y)$ in the presence of external noise is described by Eqs. (126), (127), and (128) [237], where in Eq. (126), instead of $P(x)$, the two-variable function $P(x, y)$ is considered to be the probability to detect a signal of level x in the presence of external noise of level y.

Using this approach to separate external noise from endogenous brain noise confirmed the hypothesis of a relationship between external and internal noise intensities when observing CR. The visual detection experiment [236] showed that the ability to observe ECR was associated with suboptimal levels of endogenous noise in subjects. The authors of [236] used the spread of the psychometric function in the absence of external noise as an indicator of the endogenous noise level.

It should be noted, however, that determining internal brain noise is still a complex unsolved problem, although in some specific tasks, for example, when perceiving ambiguous images perception, as well as clearly ambiguous auditory or tactile stimuli [230], some approaches have been developed to measure internal brain noise. Apparently, the level of internal noise varies greatly from subject to subject. It is likely that the level of internal noise can also vary greatly in the same subject, depending on his condition. This is confirmed by Fig. 28(b) with psychometric functions corresponding to different noise intensities for three subjects. To test this, the level of endogenous brain noise should be manipulated.

Currently, it is not entirely clear how the level of endogenous noise can be varied. Ward [238] suggested that this could be realized by manipulating variables that might influence endogenous noise such as arousal. It is also possible to alter the level of endogenous noise, for example, by developing paradigms that alter the task complexity or develop the skills of the subjects. If the fusion of multiple independent random synaptic inputs contributes to endogenous noise, then due to the involvement of large neural populations in the task, different organization of neural networks can lead to different levels of endogenous noise [224]. In this regard, Milton et al. [239] showed experts have a purposeful and efficient organization of task-related neural networks, whereas novices' networks are more scattered. Moreover, the brain neuronal network is able to quickly reconfigure during short-term training session of a visual 2AFC task of sorting stimulus [240].

The diagnosis of brain CR in psychophysical experiments is based on the measurement of psychometric functions, and more specifically on signal detection theory in psychophysics, suggesting that the spread (i.e., trial-to-trial variability) results from noise sources either in bottom-up sensory or top-down non-sensory processing, or both [241]. One problem is that a psychological measure, such as spread, is not a direct measure of neural noise. Therefore, a direct neurophysiological measure to test the stochastic facilitations hypothesis is desirable. For non-invasive physiological measurement of brain noise level, the most common option is to use EEG or MEG.

Apparently, the first attempt to measure brain noise using EEG in visual perception was made by Srebro and Malladi [242]. The problem with their approach was that, due to volume conduction, EEG noise originates not only in visual areas, but also in very large cortical areas that may not be involved in visual perception. It is unknown whether source current estimation methods [243], which suppress the effect of volume conduction, can solve the noise source separation problem in the brain. As far as MEG is concerned, although the effect of volume conduction is less pronounced, MEG also has limitations. Magnetic signals from the brain are extremely weak compared to magnetic noise from the environment (e.g., fluctuations in the Earth's geomagnetic field) and the human body (e.g., electrophysiological signals from skeletal muscles). Given this limitation, measuring the brain noise level using MEG is also difficult. The solution here is to use indirect measurements of EEG and MEG signals when we have adequate mathematical models of the perceptual and processing processes that take place, as described in Sections 4.4 and 5.1 for EEG and MEG, respectively.

Another approach to directly measuring brain noise is to use an invasive technique such as the electrocorticogram. However, this research is more applicable to the study of stochastic effects in animals (see, e.g., [244,245]) and their application to the human brain is limited only to medical applications [246]. Thus, at present, we still have to resort to indirect measurements based on psychophysical models when studying brain noise, especially in psychophysical experiments for measuring psychometric functions.

5.4. Event-related coherence in the brain

Coherence was used in many studies of brain connectivity in patients and healthy individuals, including studies of working memory [247], brain lesions [248], hemiparesis [249], rest-state networks [250], schizophrenia [251–253], response to anti-panic drugs [254], and motor imagery [255,256]. Brain connectivity manifests itself in three forms: structural, functional, and efficient [257–260]. Structural connectivity identifies anatomical neural networks that show possible pathways for neural communication [261,262]. Functional connectivity finds active areas of the brain that have a correlated frequency, phase, and/or amplitude [263]. Finally, effective connectivity uses information about functional connectivity and additionally determines the direction of the flow of dynamic information [264,265]. Effective and functional connectivity can be measured in both frequency [266] and time domains, e.g., Granger causation [260] or artificial neural network functional connectivity [267]. For instance, the presentation of flickering visual stimuli induces coherent responses in the visual cortex at the flicker frequency and its harmonics with different coherent neural network sizes in subjects [219,268].

Coherence is commonly used to quantify neural synchrony between spatially separated EEG electrodes or MEG coils [269]. Essentially, it is an estimate of the relative amplitude and phase consistency between two signals in a given frequency band. There is a linear mathematical method that results in a symmetrical matrix that lacks any direction information. Identical signals give a coherence value of 1, while the coherence value approaches 0 as the dissimilarity between the considered signals increases.

Significant progress has been made in the development of new computational algorithms that allow calculations of connectivity directly between different brain regions (source space) [260] instead of electrodes or coils (channel space). Initial space analysis provides better anatomical localization and allows for intersubject or group analysis, because brain activity can now be projected to a more standardized space. In 2004 Hoechstetter et al. [270] presented a new method for studying sources of brain coherence. Discrete multi-source models were generated using brain electrical source analysis, and source activity was mapped to time–frequency space. In addition, magnitude-squared coherence was assessed to reveal associated brain sources. The use of inverse solutions for estimating brain activity in the source space from the channel space allowed the elimination of the current leakage between adjacent channels. This prevents localization errors, which are fundamental for channel space coherence analysis.

Another signal processing technique used to measure coherence in EEG and MEG is phase synchronization, a measure of how stable the phase difference is over the time in question. Phase locking requires that the signals in question be phase-locked with zero or any finite phase difference, regardless of their respective amplitudes. In this regard, brain noise can cause desynchronization in a neural network [91]. Each participating neuron, and the synapses that connect them, adds a brain-specific noise when a stimulus is presented to the subject. Therefore, it can be argued that a larger neural network will carry higher brain noise and therefore lower average coherence. On the other hand, larger active neuronal oscillations in response to a stimulus are likely to have stronger average coherent activity and also entail higher brain noise. Thus, the relationship between the observed coherence and the level of inherent brain noise is one of the central problems in cognitive neuroscience [271,272].

The analysis of neurophysiological data obtained in the experiments on visual perception of flickering stimuli confirmed the hypothesis of the existence of the correlation between event-related coherence in the visual cortex and neuronal noise [273] performed independent analyses of the MEG data of 17 participants using two most popular open source MATLAB toolboxes (FieldTrip and Brainstorm). Before the coherence and brain noise calculations, the MEG data were first converted from the recorded channel data into the brain source waveforms by solving the inverse problem. The inverse solution was obtained for a 2D cortical shape in Brainstorm and a 3D volume in FieldTrip. Stronger brain interaction with visual stimuli was found to be consistent with higher levels of brain noise in both studies.

In the MEG experiment, a gray square image with varying greyness levels on a gray background (brightness: 127 in 8-bit format) was projected onto a translucent screen. The pixels' brightness was modulated by a harmonic signal with frequency $f_m = 6.67$ Hz (60/9) and a 50% amplitude, i.e., between black (0) and gray (127). This particular frequency was chosen because it causes the most pronounced spectral response in the visual cortex [219]. The experiment began with the presentation of a non-flickering image with a red dot at the center, on which the subject had to concentrate his gaze for 120 s. The recorded brain activity was used as a reference signal or background. After a short rest, the square image began to flicker and was presented 2–5 times for 120 s, interrupted by a 30-s break between presentations.

The sources of the neural activity were localized by building a forward model and a leading field matrix. The forward model allows one to estimate the field measured by MEG sensors for a given brain current distribution for each subject. Then, lead fields or forward problem solutions can be evaluated using various algorithms, such as single sphere [274], overlapping spheres [275], approximation of realistic geometry spherical harmonics [276], and boundary element methods [277].

The forward solution computed with Brainstorm utilized the overlapping spheres method. The number of cortical sources was 15,000. Unlike Brainstorm, in FieldTrip a semi-realistic head model developed by Nolte [276] was used, so-called a single-shell model, which is based on correcting the lead field for a spherical volume conductor by superimposing fundamental functions, gradients, harmonic functions, built for spherical harmonics. So, the head volume was discretized with a grid with a 0.7-cm resolution to obtain a source space consisting of 9025 voxels, whereas the lead field matrix was calculated using each grid point. Thus, Brainstorm used a surface model of the cortex, while FieldTrip used a volumetric model.

The next step in assessing the location and strength of neuronal activity was to find the inverse solution that can be calculated using several options, including dipole fitting based on nonlinear optimization [278], minimum variance beamformers in time and frequency domains [279,280], and linear estimation of distributed source models [281,282]. In both software analyses, standardized low resolution brain magnetic tomography (sLORETA) was used [283]. To calculate intracerebral oscillators, sLORETA utilizes standardized current density images. The sLORETA family of solutions were validated using numerous imaging [284,285] and simulation [286,287] methods. Despite the blurring of the image, sLORETA showed accurate localization with zero error in the reconstruction of single sources in all noiseless calculations [288], i.e., the estimated maximum current density coincides with the exact dipole location [282]. Meanwhile, in all simulations with noise, sLORETA yielded the lowest localization errors compared to the minimum norm solution.

Stimulus-induced coherence in the brain was used to estimate the size of the activated brain network and characterize the strength of its activation. Since the analysis methods and derived source models differ significantly, different software programs require appropriate independent indices for evaluating event-related coherence (ERC). For both F- (C^F) and B-trials (C^B) magnitude-squared coherence was calculated between time series of each of the 15,000 brain sources and the reference sinusoidal signal at the second harmonic of the flicker frequency ($2f_m = 13.33$ Hz) was measures. To assess ERC in the brain, the difference between coherence values of F- and B-trials was obtained for cortical sources in visual areas V_1 and V_2 according to the Brodmann atlas, i.e., $ERC = C^F_{vis} - C^B_{vis}$. The distributions of the average ERC over the cortex for typical subjects with low and high brain noise levels are illustrated in Fig. 29.

The results showed that subjects with stronger visual cortical activity displayed stronger brain noise which was estimated using the method described in Section 5.1. This connection can be explained as follows. The higher the power of reconstructed sources, the larger neural network and hence the number of synapses are involved in cognitive activity. Since neurons and synapses contribute into phase-destabilizing stochastic perturbations, the overall brain noise level is positively correlated with a size of the neural network size involved in information processing.

6. Noise-enhanced performance of neurointerfaces

Many researchers working in the field of brain signals try to reduce external noise, as they consider it detrimental to the detection and transmission of information. Indeed, too strong noise can complicate the interpretation of experimental data and thus make it difficult to control neural interfaces. However, as early as 30 years ago, it was discovered that random

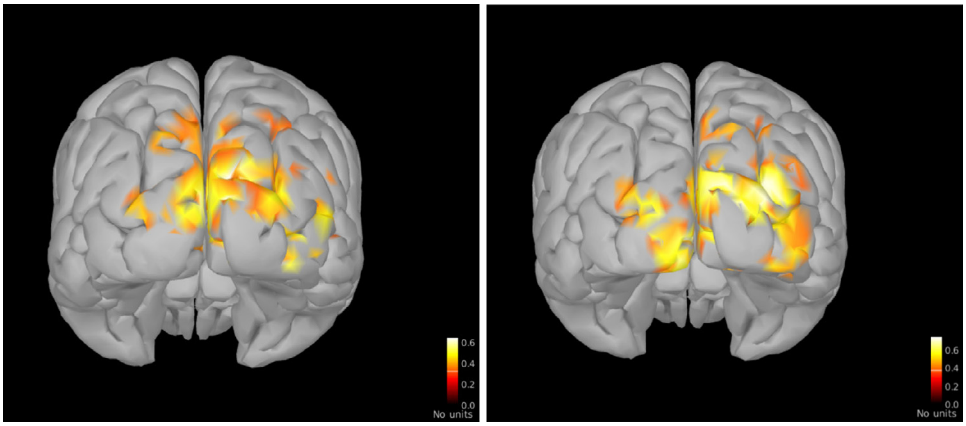

Fig. 29. Typical cortical distribution of event-related coherence (ERC) for subjects with (left) weak and (right) strong brain noise. Neural activation is more extensive in the right image.
Source: Based on data from [273].

fluctuations play a beneficial role in enhancing the detection of weak information-carrying signals. In particular, it was found that external noise can improve sensibility of sensory neurons due to the existence of CR. Sensory neurons are ideal for demonstrating this effect because they are inherently noisy and act as threshold systems [289]. Therefore, threshold CR plays a significant role in sensory perception because it enhances the detection of weak biological signals and thereby improves biological information processing, including auditory, visual, tactile, and even balance [290].

6.1. Stochastic facilitation

It should be noted that some authors confuse "coherence resonance" with "stochastic resonance", especially when describing psychophysical experiments. Although both resonances are stochastic in nature, the latter is a particular case of the former. Here we will adhere to the above terminology and call a stochastic resonance without a periodic signal a coherent resonance.

This uncertainty in the definition of CR and SR in biological systems was noted by McDonnell and Ward's [291], who introduced the concept of *stochastic facilitation* instead of SR when considering noise effects on the coherent dynamics of biological systems. In Fig. 30 we illustrate their framework for studying stochastic facilitation in neural systems. The first step is to formulate a hypothesis about the positive role of biological noise in facilitating signal processing or the computational task of a particular neural system. Next, a biological entity is identified that can be stimulated with inputs that match the hypothesis, and responses are measured. Then, the input signal relevant to the hypothesis (if necessary) is selected and the noise level is generated and injected into the system. After that, data are collected and processed. Based of the obtained data, the hypothesis proposed at the beginning of the study is confirmed and the conclusion is made about the effect of noise on the coherence of the biological system. This is an important paradigm shift, because in previous studies of stochastic and coherence resonance, researchers proceeded from a different concept. Typically, the performance of a neural system chosen for the study was measured through the output SNR as a function of the noise power. Such an approach required an input periodic signal, which is rare in biological experiments. In addition, the output signal is often defined solely in terms of time of action potentials, and the SNR is based on the power spectral density of the resulting stochastic point process.

Instead of formulating first a computational hypothesis, the choice of SNR as a metric imposed an implicit hypothesis that the computational role of the neural system is to produce a sequence of action potentials. Our experimental results justified this approach in which a hypothesis should be formulated first and explored using only relevant biologically acceptable signals and metrics. Specifically, we estimated the CR effect by expanding the functional brain network [8] or finding the perceptual threshold of a particular image, when the approach based on the calculation of the classical SNR does not work.

6.2. Enhanced sensitivity of visual perception

In many experiments on studying human visual information processing the researchers use images of different contrasts (see Section 4.4) or noisy images. One of the first experimental observations of CR was reported by Simonotto et al. [292]. Although the authors of that and other papers speak about SR, in fact, they are dealing with CR. Let us dwell in more detail the experimental technique of their work.

In the psychophysical experiment of Simonotto et al. [292], noisy Big Ben images shown in Fig. 31(a) were presented to subjects in random sequence. The noise intensity and/or correlation was varied with the time of presentation. The

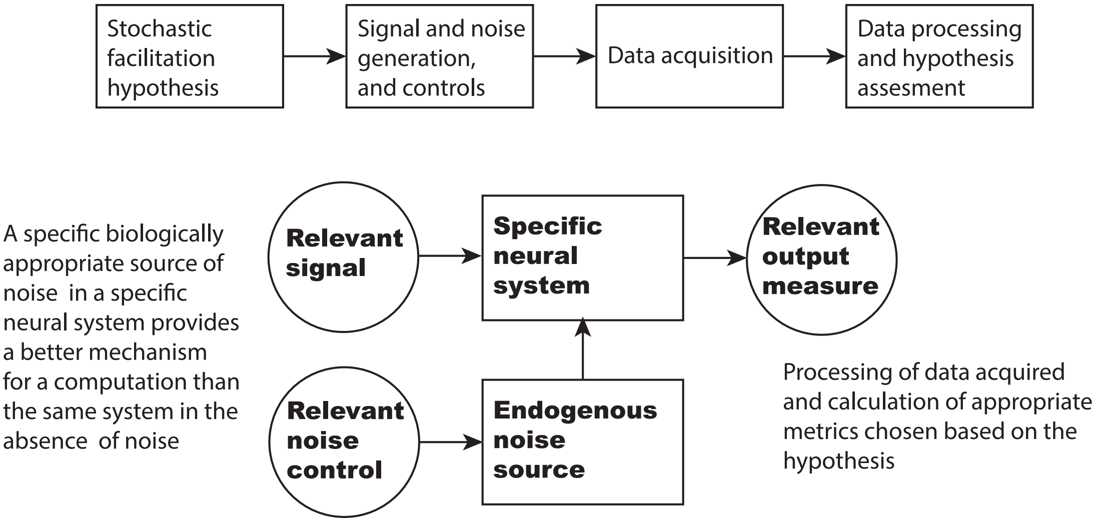

Fig. 30. Algorithm for studying stochastic facilitation in neural systems.
Source: Adapted from [291].

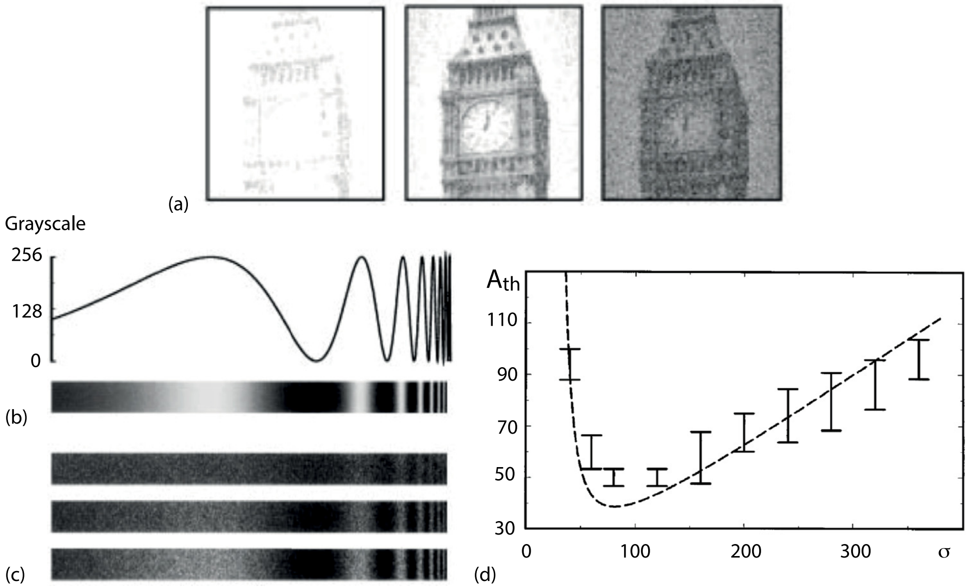

Fig. 31. (a) Examples of visual stimuli: the Big Ben pictures digitized on a 1 to 256 gray scale with a spatial resolution of 256 × 256 pixels. A random number j, from a Gaussian distribution with zero mean and standard deviation σ, is added to the original gray value i of every pixel. Thus, noise in each pixel is incoherent with that in all other pixels though the standard deviation is the same for all. The resulting image is then threshold filtered according to the rule: if $i+j<\Delta$, the gray value in that pixel is replaced with 256 (white), otherwise with 1 (black). The pictures are drawn for $D=30$ and $\sigma=10$, 90, and 300 on the gray scale (from left to right). (b) The spatial function $A\sin(1/x)+128$, where x is the horizontal coordinate, used to generate the stripes of spatially varying gray levels as shown below, for the case of maximum contrast $A=128$. (c) Three example stripes for decreasing contrast $A=128$, 78, and 28 (from bottom to top), threshold filtered with $s=250$ and $\Delta=150$. The temporal development of noise was generated by writing a new realization of noise into each frame, threshold filtering, and presenting the images on a monitor at a 60-Hz frame rate, a time interval which is considerably faster than known averaging times in the visual system. (d) Perceptive contrast threshold A_{th} dependence on noise intensity σ. The subject was presented with 10 different noise intensities chosen at random with each noise intensity visited randomly 10 times for a total of 100 presentations in a single session. The error bars are standard deviations of 10 determinations of A_{th} by the subject at each noise level.
Source: Based on data from [292].

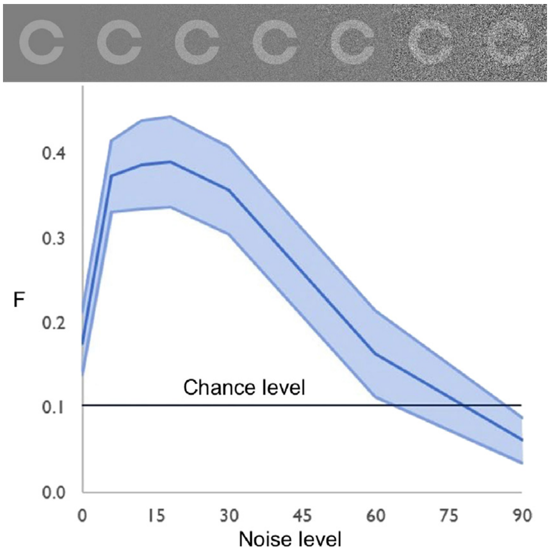

Fig. 32. (Up) Noisy letters and (down) fraction of recognized letters versus noise level. The blue line is the mean value over all subjects.
Source: Based on data from [296].

images were digitized with a spatial resolution of 256 × 256 pixels. Then the gray values of all pixels were shifted below the threshold level, so that the image was not visible on the screen. Gaussian noise with zero mean was added to the sub-threshold, which acted on each discrete screen pixel independently (the noise sources in each pixel were uncorrelated). If the gray value of a particular pixel crossed the perception sensitivity threshold, it became visible on the screen, otherwise it remained invisible (white). As a consequence, at low noise levels only part of the pixels appeared on the screen, so that the image recognition was impossible. At a very high noise level, almost all pixels became black and the image recognition was difficult. However, at a certain (optimal) noise intensity (different for different subjects), the image recognition maximizes and it can be perceived. As seen from Fig. 31(a), the middle image is the one most clearly perceived since the noise intensity of the pixels is close to the optimum value for visual perception.

However, such an image, taken for clarity of consideration, is not suitable for quantitative determination of image quality in psychophysical experiments. Instead, a pattern defined by the function of amplitude A, or contrast, with variable spatial frequency was used (upper panel in Fig. 31(b)). The bottom panel in (b) shows the maximum contrast band without noise with gray values defined by the spatial function without threshold filtering. Three examples of bands for the same noise intensity σ (close to the optimal value) and threshold Δ, but with contrast values decreasing from bottom to top are displayed in Fig. 31(c). Subjects were presented with a sequence of images, each of which consisted of a set of 7 such bands. The threshold remained constant throughout the experiment, but the standard deviation of noise for each presentation was randomly chosen from a set of 10 values. Subjects were asked to count from bottom to top until they reached a band in which they could no longer distinguish a particular subtle feature, such as one of the high-frequency vertical bands to the right of the bands. Thus, they found the threshold of perceptual contrast A_{th} for that particular feature and noise intensity σ.

The perceptual threshold as a function of the noise intensity σ for one of the subjects is shown in Fig. 31(d). The dependence has a pronounced minimum at the optimal noise intensity. The solid curve represents the results obtained on the base of the theory of the positive threshold crossing rate [293], and is often used to describe more precisely the effects of SR [294,295]:

$$A_{th} \propto \sigma \exp\left(\Delta^2/2\sigma^2\right). \tag{129}$$

Although the agreement between the experimental data and approximate description is not very good, it would be naive to believe that the complex processes of visual perception in the brain can be described within the framework of a single SR model [297]. Moreover, the mathematical description of the threshold perception was derived under the assumption that an external periodic signal modulates the bistable potential. However, in the case under consideration, there is no periodic signal, and we are dealing with the classical CR effect.

Another interesting experiment which evidenced the improvement of visual sensitivity in CR was performed by Itzcovich et al. [296]. Letters with different noise level were presented in random sequence to subjects with retinal disorder and severely impaired (see Fig. 32). The subject pressed a key if she (he) recognized the image. The authors discovered that noise added to the letter images improves the detection of subthreshold vision. It was found that the fraction (F) of recognized letters has a resonant character with respect to the noise level. Maximum recognition ranged between 20% and 80% pixels crossing the perceptive threshold in the letter area.

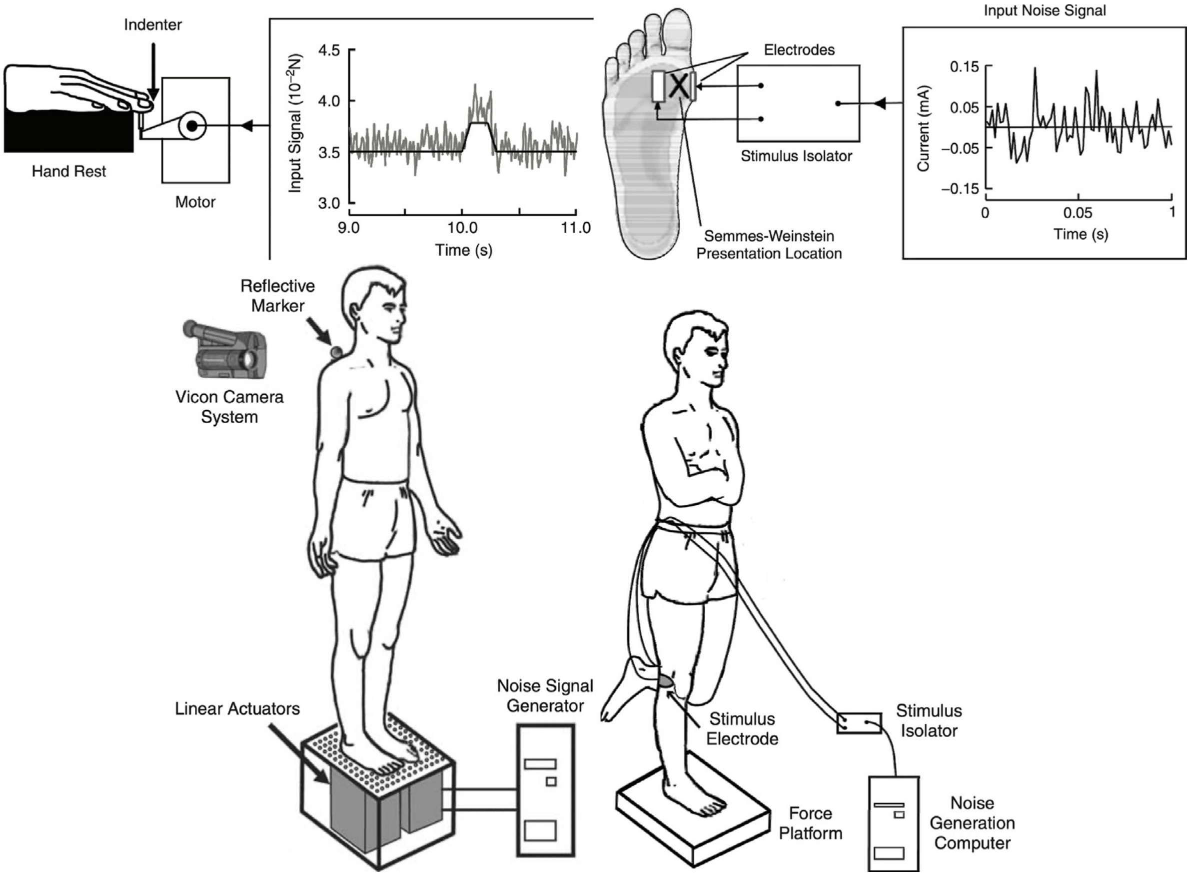

Fig. 33. Schematic representations of experimental setups for psychophysical tests. (Top) Enhancing somatosensation with (left) mechanical and (right) electrical input noise applied to hand and foot, respectively. The insets show samples of mechanical and electrical noise signals. (Down) Enhancing balance control with mechanical input noise while the subject staying (left) on two legs and (right) on one leg.
Source: Adapted from [302].

6.3. Somatosensory control through coherence resonance

Current trends in neuroscience have moved CR research in sensory biology from the level of sensory receptors to the level of neural networks of the central nervous system (CNS). The most attractive CR feature is that it promises to benefit humanity, for which numerous physiological functions are marked by the threshold behavior. For example, some CNS disorders are caused by an increase in the sensitivity threshold, that leads to a decrease in the spiking frequency of the corresponding neurons. In this context, CR was observed in mammalian neural networks [298]. These results inspired other researchers to use CR for therapeutic purposes, for example, in violation of the person's balance, the patient's movements, and other physiological functions [299,300]. In particular, electrical or mechanical noise was used to enhance people's ability to detect subthreshold skin stimuli and control balance [301–303]. The benefits of noise are not limited to sensory processes, but extend to somatosensory control as well. In this regard, Priplata et al. [304] found that noise-based devices, such as randomly vibrating insoles, could improve human balance control in the elderly.

Fig. 33 shows some experimental schemes on somatosensory control through CR. The top row illustrates how mechanical and electrical noises applied to the hand and foot, respectively, improve their sensation. The bottom row shows experimental setups for improving human balance by noisy electrical stimulation applied either to the planform (left picture) or to one of the legs (right picture).

Let us consider the effect of behavioral CR effect on the posture control system in more detail. The human balance control system depends, in part, on somatosensory feedback and on the elderly; decreased somatosensitivity is associated with an increased likelihood of falling. Priplata et al. [304] suggested that external noise could improve sensory and motor functions through the CR mechanism. During the experiments, the participants stood quietly on the vibrating gel-based insoles with eyes closed and arms at their sides, as illustrated in Fig. 34. Two insoles were molded with a viscoelastic silicone gel. Three vibrating elements, called tactors, were embedded in each insole to propagate noise-like vibrations to the plantar foot surface. Each insole received a noise signal, whose amplitude was set independently with potentiometers for each foot.

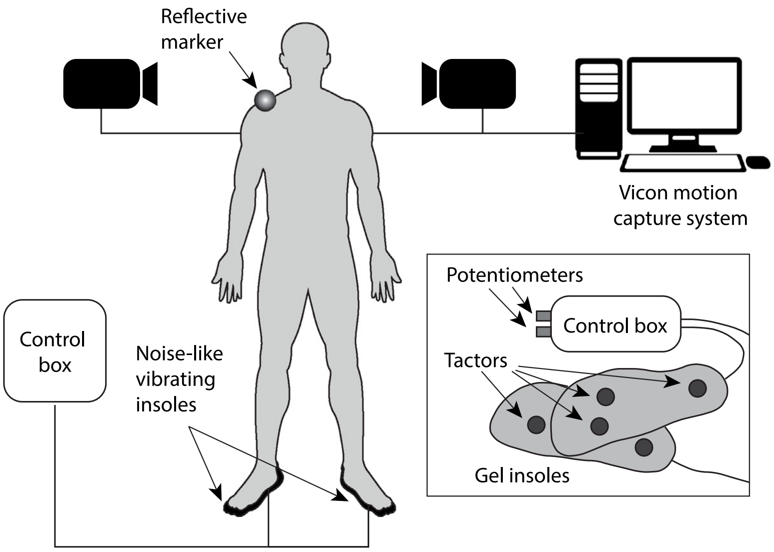

Fig. 34. Experimental setup for observation of behavioral CR in human posture control system. The insert shows the design of vibrating insoles. *Source:* Based on data from [304].

To assess whole-body posture, head-arm-trunk segment displacement was measured using a reflective marker attached to the right shoulder of each participant using a Vicon motion analysis system to record the displacement of this marker during each 30-s standing test. A graph of mediolateral and anteroposterior shoulder displacement, called a stabilogram, was analyzed for each trial. Participants performed a series of trials with and without mechanical noise, which were randomized in a pair-wise fashion.

To characterize equilibrium during quiet standing, traditional sway parameters were calculated from the stabilograms: mean stabilogram radius, area covered by the stabilogram, maximum sway radius, and range of anteroposterior and mediolateral excursions. Three random walk variables were also used: critical mean squared displacement, effective long-term diffusion coefficient, and long-term scale exponent [305]. The critical mean square displacement characterizes the threshold at which sensory feedback mechanisms are activated by the postural control system, while the effective long-term diffusion coefficient and the long-term scale exponent reflect the stochastic activity and antidrift-like dynamics, respectively, of these feedback mechanisms [305,306]. The main hypothesis of the study [304] was that adding mechanical noise to the feet through insoles would, through a CR effect, reduce postural vibrations.

The authors evaluated a resonance effect of noise exposure of the somatosensory system on posture control in humans. They experimentally showed that postural fluctuations in both young and old people during quiet standing can significantly be reduced by exposing the feet to mechanical noise through vibrating insoles. Although the observed effect was referred to as “stochastic resonance”, the experimental setup explicitly implied the observation of “coherence resonance” because no periodic signal was applied.

The experiment of Priplata et al. [304] showed that noise led to a decrease in all sway parameters in elderly participants. The authors believe that subsensory mechanical noise imposed on the feet of calmly standing people using vibrating insoles leads to an increase in feedback and a decrease in postural sway, which expresses the CR effect. Interestingly, comparing the results obtained in a group of elderly participants with a group of younger subjects shows that elderly people exhibit better motor control performance than younger people when mechanical noise is applied to their legs. Young participants may have near-optimal sensory feedback and balance control compared to elderly subjects, who often have lateral postural instability and elevated sensory feedback thresholds. Unfortunately, the authors did not present the dependence of the balance maintenance performance on the external noise intensity, apparently due to the laboriousness and long duration of such measurements, difficult for elderly participants. At the same time, as was shown in some psychophysical experiments and in Section 5.2, the most easily measured natural brain characteristics are the psychometric functions.

The main conclusion is that subthreshold stimuli can be detected when the patient is exposed to the optimal dose of any type of noise. Thus, CR improves the patient’s tactile sensation when a mechanical stimulus is close to or below a threshold. In this regard, the development of special interfaces, such as socks and gloves, controlled by electrical or mechanical noise, could be useful in situations requiring increased tactile sensation. Possible applications include telerobotics, microsurgery, cardiology, and the like. The neural interfaces based on CR can also be helpful for people with elevated cutaneous sensory threshold after a stroke or other cerebrovascular accident. Of note is an interesting application of CR in the human blood pressure regulation system, so-called “baroreflex” system [307], where a negative feedback was used to automatically regulate the blood pressure by changing the heart rate and vascular resistance. It was found that the addition of a certain level of noise optimizes the heart rate response.

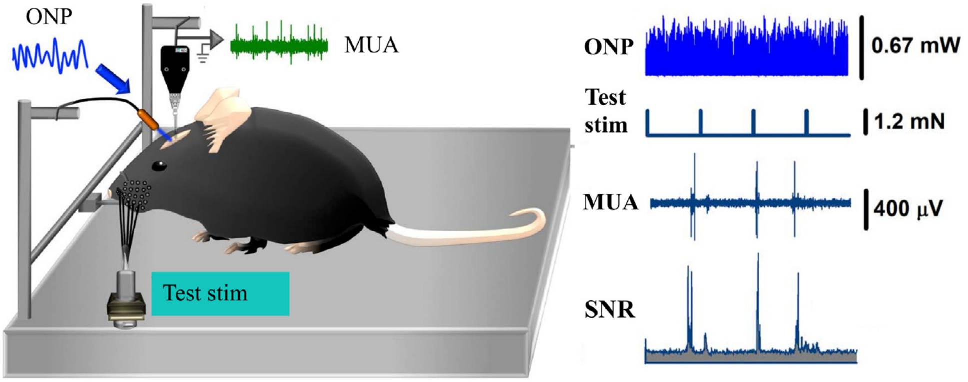

Fig. 35. (Left) Experimental arrangement of optogenetic noise photostimulation (ONP) applied to barrel cortex during whisker-induced multiunit activity (MUA). (Right) Typical time series of ONP, whiskers protraction input (test stim), whisker-evoked MUA response with ONP, and signal-to-noise ratio (SNR) defined by Eq. (130).
Source: Adapted from [308].

6.4. Coherence resonance induced by direct brain stimulation

As was shown in Section 4.4, the size of the neural network and, accordingly, brain noise is adjusted in such a way as to obtain CR that allows for improved perception of weak stimuli and neuronal communication. In this regard, an important question arises: Is it possible to improve the perception of sensory information using external stochastic brain stimulation? If the answer to this question is positive, such stimulation could be used in special neurointerfaces to manage neural noise in order to obtain CR and help a person process sensory information most efficiently when performing cognitive tasks.

Stochastic optogenetic photostimulation in mice. The first attempt to control brain noise was made in 2018 by Huidobro et al. [308], who used optogenetic noise-photostimulation (ONP) of the barrel cortex (BC) to selectively adjust the noise level in the population of mouse cortical stem neurons. The experimental setup is presented in Fig. 35.

This way, ChR2 neurons in the barrel whisker cortex were selectively stimulated by the optical noisy signal, and neurons responded to sensory stimuli from the whiskers. The whisker-induced multiunit activity (MUA) response was used as a first step to determine whether ONP applied to BC mice can improve somatosensory perception upon whisker stimulation. Three stimulation protocols were performed: (i) mechanical test stimulation of whiskers only, (ii) mechanical test whisker stimulation during ONP, and (iii) ONP of BC alone. Typical examples of the corresponding time series are shown on the right side in Fig. 35.

The output SNR was calculated as follows:

$$\mathrm{SNR} = \frac{|\mathrm{MUA}_w + \mathrm{ONP}|}{|\mathrm{MUA}_0|}, \tag{130}$$

where MUA_w and MUA_0 are respectively the whisker-evoked MUA and the MUA elicited by ONP without whisker prostration.

As a result, it was found that there is an optimal non-zero intensity of noisy stimulation when the somatosensory perception reaches a maximum value, as illustrated in Fig. 36. Such a coherence resonance behavior was observed the total area under the whole output-SNR graph averaged over all experiments (gray area in the SNR time series in Fig. 35).

The results suggest that internally generated brain noise can improve neural activity in response to sensory input.

Transcranial random noise stimulation in humans. Transcranial random noise stimulation (tRNS) of visual cortex was also applied to humans [244,309]. The brain stimulation was performed when participants completed the random-dot-motion (RDM) recognition task. Participants were exposed to visual stimuli consisting of a set of moving dots as illustrated in Fig. 37. Some correlated points move to the right, while the remaining uncorrelated points move in random directions. The participant should judge whether the dots moved on average to the left or right. This value is referred to as the level of coherence.

The RDM tasks with different coherence levels were presented to participants, and the number of correct decisions about the motion direction was calculated. Simultaneously, tRNS was applied either to the left, right, or bilateral visual cortex, as illustrated in Fig. 38.

The analysis was performed by calculating the group %correct-choice-index (%CCI) for 5 levels of the coherence and 5 values of the tRNS intensity by dividing %correct motion-direction responses under tRNS by %correct responses when no tRNS was applied (baseline) according to the following formula:

$$\%\mathrm{CCI} = \%\mathrm{Corr}(i)/\%\mathrm{Corr}(\mathrm{zeronoise}), \tag{131}$$

where i denotes each of the 5 tested noise intensities.

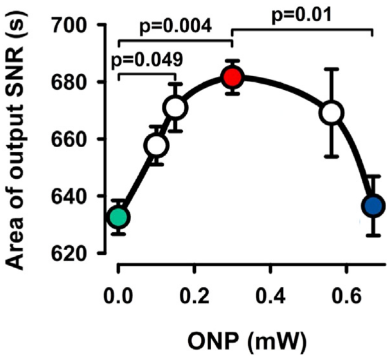

Fig. 36. Coherence resonance measured as the averaged output SNR of the whisker-evoked multiunit activity of neurons from the barrel cortex of Thy1-ChR2-YFP-transgenic mice.
Source: Based on data from [308].

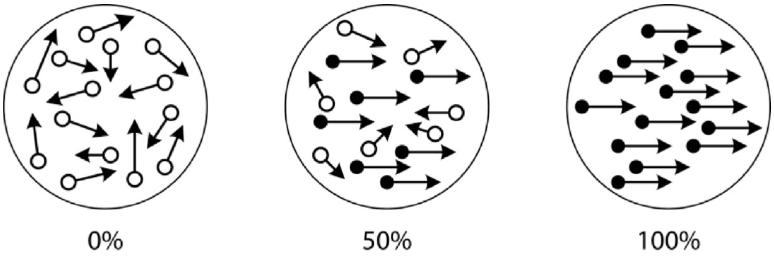

Fig. 37. Schematic of the random-dot-motion (RDM) tasks with 0%, 50%, and 100% coherence of dots moving to the right.

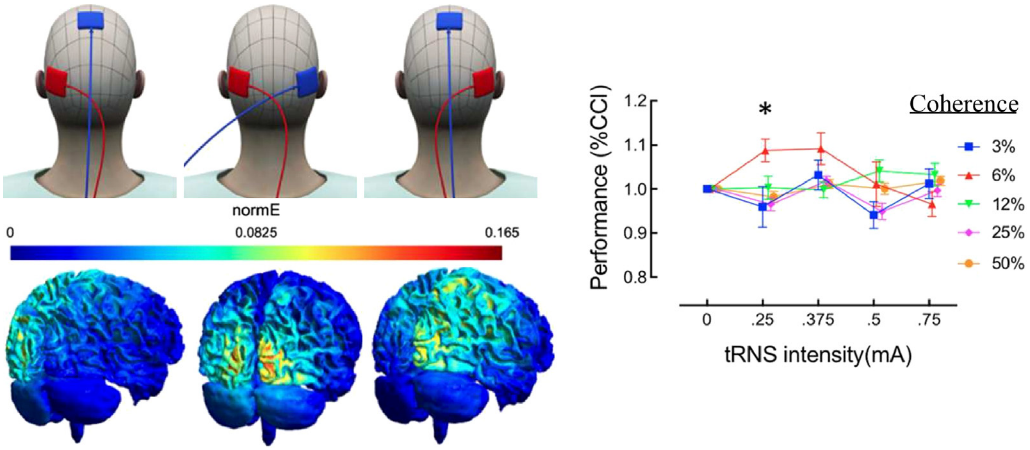

Fig. 38. (Left) Electrode pad montages and modeled electrical field strength (normE) for three tRNS experiments: left, bilateral, and visual cortex stimulation. (Right) Coherence resonance in perceptual decision-making in the RDM discrimination task during bilateral stimulation. Performance (correct decisions) for each coherence level as a function of tRNS intensity. $^{*}p_{\text{corrected}} < 0.05$.
Source: Based on data from [244].

It was found that bilateral noisy tRNS provides the beneficial effect on the efficiency of sensory processing and cognitive ability. As seen from the graphs in Fig. 38, the performance in perceptual decision-making reaches maximum at a certain noise level (between 0.25 and 0.375) when the coherence level is equal to 6%. At the same time, no resonance behavior was detected for unilateral tRNS. The results are in good agreement with ONS studies in animals described in the previous section.

Thus, tRNS-induced CR may be promising for use in BCI to improve sensory perception, motor activity, and cognitive functions in people with congenital or acquired neurological disorders, in the elderly, or even potentially in people involved in specialized professional and sports activities.

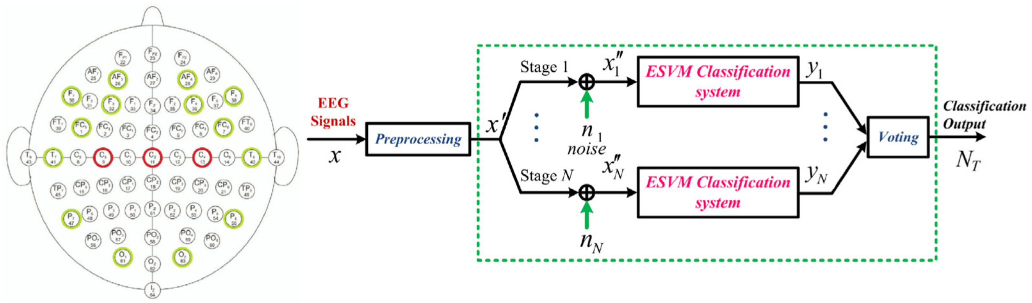

Fig. 39. Schematic of the noisy ESVM system for P300 and MI classification.
Source: Adapted from [318].

6.5. Controlling mental commands through coherence resonance in BCI

One of the important aims of BCIs is to control external devices with the help of mental commands without using any movements [255,310,311]. In parallel, brain activity is recorded using electroencephalography (EEG), functional magnetic resonance imaging (fMRI), positional emission resonance imaging (PET), or magnetoencephalography (MEG) [312]. The most popular non-invasive BCIs are based on EEG due to its relative simplicity, low cost, and non-invasiveness. Many types of neural activity patterns are present in EEG signals, such as slow cortical potential (SCP), P300, steady state visual evoked potential (SSVEP), motor imagery (MI), etc. [313]. P300 and MI are most commonly used for BCI applications. P300 applications include the P300 speller paradigm, neurophones, wheelchair control, and robotic arms [314]. Whereas, MI applications include robot control, wheelchair control, car game control, and rehabilitation [315]. The MI paradigm aim is to distinguish between different MI tasks, such as imaginary movements of the left and right hands, fingers, foots, etc. Classification methods include support vector machines (SVM), linear discriminant analysis (LDA), and deep learning approaches. Among various techniques, ensemble support vector machines (ESVM) [316] and convolutional neural networks (CNN) [317] are the most suitable for solving the problem of P300 signal variation from different subjects.

Recently, Sampanna et al. [318] have shown that the addition of Gaussian noise improves the accuracy of P300 and MI classification systems in the training phase, in the testing phase, and in both the training and testing phases. The scheme of the noisy P300 and MI classifier is presented in Fig. 39.

The classification system is a set of N conventional identical stages. Each stage i processes the same filtered signal x' of the raw data x received from EEG channels. Then, independent noise n_i is added to the signal x' at each stage. The training process of the classifier is to find an optimal hyperplane that separates two classes with the maximum possible margin. Training the system with known data gives us optimal parameters for using in a real EEG signal classification system.

The classification accuracy P_A is defined as a ratio of the number of correct classification outputs N_C and the total number of testing characters N_T obtained in the experiment, i.e.,

$$P_A = \frac{N_C}{N_T} \times 100\%. \tag{132}$$

Fig. 40 illustrates the CR effect of the P300 and MI classification systems. One can see that additive noise of the appropriate intensity improves the classification accuracy.

Experimental results show that adding noise to the pooled datasets can virtually increase the number of training samples and reduce the likelihood of overfitting. Moreover, noise can improve the accuracy of BCI systems for any number of signal repetitions. This means that we can reduce the number of signal repetitions or collection time and thus can speed up responses with high accuracy. Due to the CR phenomenon, adding noise improves the detection of weak signals. Thus, these collective benefits of noise suggest that future research should consider the role of adding noise to the BCI system design. The appropriate noise intensity depends on signal characteristics and classification systems such as features, classifiers, number of signal repetitions, and number of stages in the set.

Xie et al. [319] showed that adding spatiotemporal noise to visual stimuli improves the classification performance of BCIs based on steady-state motion visual evoked potential (SSMVEP), as well as enhances plasticity of evoked potentials [320]. In addition, moderate visual noise reliably reduces mental workload and fatigue that often occurs during online visual BCI operations [321,322]. Recent studies evaluating the impact of natural artifacts on BCI SSVEP showed that random disturbances can improve the BCI performance in some subjects [323].

7. Conclusion

In this review, we analyzed an important phenomenon in the complex system theory known as coherence resonance, which is observed in a wide class of excitable neural networks when exposed to endogenous or exogenous noise of optimal

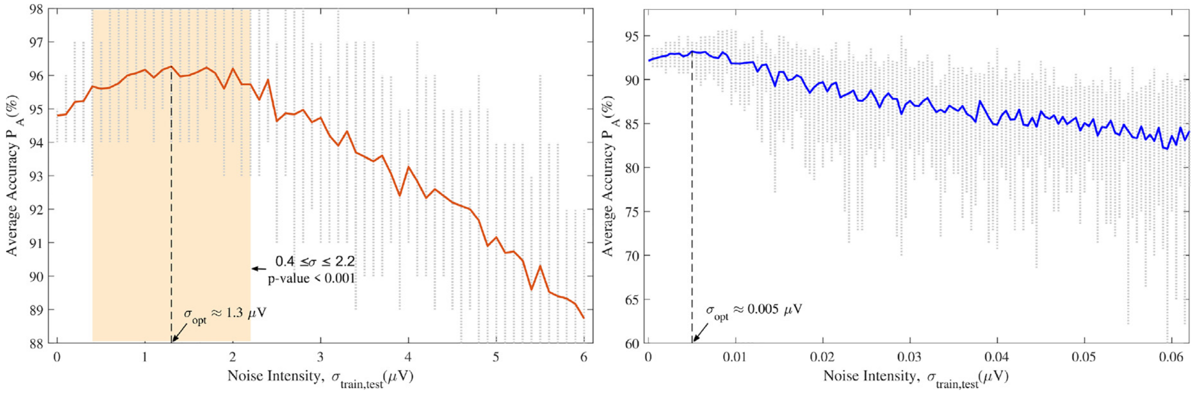

Fig. 40. Noise-induced coherence resonance in the accuracy of (left) P300 and (right) MI classifications. The system uses a set of ESVM classifiers with $N = 20$ stages. The vertical dashed lines show the variation in noise realizations.
Source: Based on data from [318].

intensity. As a result of CR, the performance of such networks can be greatly improved near the excitation threshold. We can say that noise acts as a constructive factor that causes an increase in the degree of coherence or order in an autonomous self-oscillatory system or a network of coupled neural oscillators. On the other hand, CR can be viewed of as a noise-induced transient, in which the degree of order in a nonlinear system is increased by noise of a certain amplitude. CR is a general physical phenomenon, to which the well-studied phenomenon of SR belongs. The latter takes place in the presence of a periodic signal. In this review, we did not consider SR, since a large number of review papers [9–13] were devoted to its study.

Let us briefly summarize the main results of this survey. The effect of CR is realized when the system is exposed to noise of a relatively high intensity and diagnosed by evaluating one or more measures of the system coherence. In Section 2 we have discussed various approaches to quantifying the degree of coherence and classifying them according to the system type. To date, quite a lot of such order measures were proposed, however, depending on the type of the system under consideration (stochastic or deterministic), the CR diagnostic method differs in a set of possible measures. Particular attention has been paid to the experimental evidence of CR in the brain neural network. The main feature of such research is that we are usually not interested in a specific form of action potentials and turn to the consideration of a spiking signal to evaluate the ordering of neural spikes in time. As a consequence, such specific coherence measures as the fano-factor and effective diffusion coefficient of interspike intervals are introduced. We do not exclude that in future new tools for diagnosing CR will be developed, especially in living systems.

We should note that the CR phenomenon is not restricted to stochastic systems. A similar resonant behavior appears in deterministic noiseless systems, where chaotic oscillations play a similar role as noise in stochastic systems. This phenomenon known as *deterministic coherence resonance* was observed in bistable [56,324] and excitable [54,67,325,326] chaotic systems, including coupled chaotic oscillators [91,111,327,328]. The coherence in chaotic systems maximizes with respect to the coupling strength or mismatch between fundamental frequencies of the coupled oscillators. Consideration of deterministic CR is beyond the scope of this review.

In addition, the CR phenomenon also occurs in non-excitable systems. The necessary conditions for CR in non-excitable systems are (i) multistability, (ii) delayed feedback, and (iii) random forcing [329]. The application of random noise in a muiltistable system causes new noise-dependent time scales related to the mean escape times (or Kramers times) from basins of attraction of the coexisting states. On the other hand, relaxation oscillation times of the coexisting attractors are practically independent of the noise intensity, whereas their variances grow with increasing noise intensity. Noise-induced CR in non-excitable systems was observed in systems with two [22,55,80,329–332] and three [333,334] coexisting attractors.

Speaking about networks of excitable elements, we primarily mean networks of coupled neurons. At present, a large number of neural network models based on discrete and continuous systems were studied, and a theory based on the mean field approximation was developed to describe CR in such active media. Some of these models have been considered in Section 3. Interestingly, under certain conditions, anticoherence resonance was also observed, i.e., a decrease in the degree of order in such networks under a certain level of external noise exposure. The authors of many papers devoted to a study of CR in neural networks use a realistic Hodgkin–Huxley model described in Section 3.3. We have shown that the results of numerical simulations based on this model are in good agreement with experimental results obtained by the functional brain network measurements during sensory information processing.

A very interesting object for studying CR is spatially distributed spiking neural networks including the brain cortical network, for which CR is expressed in the formation of a spatiotemporal pattern, coherent in time or space (or simultaneously in time and space). This topic has been considered in Section 4. A particular attention was given to CR chimeras formed due to the competition of excitation waves, which, upon interaction, can suppress each other.

There is substantial evidence of beneficial effects of intrinsic brain noise on the efficiency of sensory processing and cognitive ability. In Section 5 of this review we have described the methods for estimating brain noise and the observation of CR in ensembles of brain neurons in vivo. When studying this phenomenon, we have immediately encountered a more complex situation of the need to separate external noise, leading, as saying in neurology, to external CR, and internal endogenous noise of the brain. If we can easily control and manage the former within the framework of the experiment, then we cannot manipulate internal brain noises, and often cannot even quantify them. This problem can be solved with invasive measurements of brain neuron activity. If it is not possible, we can only measure the CR effect on the brain indirectly through human behavioral characteristics, which in psychophysics are measured using psychometric functions. Coherence resonance in this case is called behavioral CR. There is a lot of confusion in psychophysical literature between the concepts of stochastic and coherent resonance. All resonance effects caused by noise are usually called stochastic resonance by neuroscientists and psychologists, although in fact a detailed study of their works suggests that they are dealing with CR. A typical example is the effect of mechanical noise on a person's leg, which can significantly improve balance control. The control methods for improving performance neurointerfaces through CR have been considered in Section 6.

Another important problem in the study of CR in the brain neural network is the difficulty in determining an adequate informative measure of order in living organisms. The correct choice of characteristics is largely determined by the correct formulation of the initial research hypothesis. Perhaps, in the case of biological systems, it is more correct to speak not about coherence or stochastic resonance, but about stochastic facilitations, the use of which was proposed by McDonald and Ward [291] in relation to neural ensembles. This issue has been discussed in detail in Section 6.1. We conclude that no matter how we call the effect of streamlining dynamics of the neural ensemble in the brain.

Intrinsic brain noise contributes not only in enhancing neuronal response in particular brain areas, but also provides pathways for neural communication between remote brain regions. It can be stated that at present it has been convincingly proven that CR can help ensure optimal communication between brain regions (communications through coherence), increase the efficiency of motor control, and improve the perception robustness of sensory information to external and internal noises. We have shown that effective visual sensory processing in the brain requires neural communication in the frontoparietal cortical network, and thus neural communication requires coherence.

Last but not least, we note that at present there is considerable interest in the possibility of experimental observation of quantum coherence resonance (QCR). This is because the theoretical and experimental study of QCR can provide new insights into possible future applications of quantum dissipative systems in important areas of quantum technologies, such as quantum information, quantum metrology, and quantum standard. Kato and Nakao [335] theoretically showed the possibility of realizing QCR in a squeezed quantum Van der Pol system. In the semiclassical approach, they interpreted this phenomenon by analogy with classical noisy excitable systems, using stochastic differential equations to describe a phase-space trajectory. They also demonstrated that the QCR phenomenon persists under moderately strong quantum fluctuations, for which the semiclassical description is unacceptable, but nevertheless, a large number of energy levels contribute to the system dynamics. Moreover, the authors found that with a further increase in the intensity of quantum fluctuations, the system can exhibit a second peak in the degree of coherence, when only a small number of energy levels are involved in the dynamics, and a strong quantum effect prevails in the system. From the physical viewpoint, QCR means that the regularity of the system's response is enhanced by the constructive action of quantum fluctuations. This differs from the quantum synchronization case, where, as in the classical approach, quantum fluctuations have a deleterious effect on the synchronization quality [336,337]. In addition, the QCR analysis in networks of quantum excitable systems is promising for the development of a quantum analogue of the neural ensembles discussed in this review.

Declaration of competing interest

The authors declare that they have no known competing financial interests or personal relationships that could have appeared to influence the work reported in this paper.

Acknowledgment

This study was supported by the Priority 2030 program of the Ministry of Education and Science of Russian Federation, Russia.

References

[1] I. Prigogine, I. Stengers, Order Out of Chaos, Bantam Books, New York, 1984.

[2] H. Gang, T. Ditzinger, C.Z. Ning, H. Haken, Stochastic resonance without external periodic force, Phys. Rev. Lett. 71 (1993) 807–810.

[3] A.S. Pikovsky, J. Kurths, Coherence resonance in a noise-driven excitable system, Phys. Rev. Lett. 78 (1997) 775–778.

[4] P. Balenzuela, P. Rué, S. Boccaletti, J. Garcia-Ojalvo, Collective stochastic coherence and synchronizability in weighted scale-free networks, New J. Phys. 114 (2014) 013036.

[5] R. Benzi, A. Sutera, A. Vulpian, The mechanism of stochastic resonance, J. Phys. A 14 (L453–L457) (1981) 7186.

[6] B. McNamara, K. Wiesenfeld, Theory of stochastic resonance, Phys. Rev. A 39 (1989) 4854–4869.

[7] A.V. Andreev, V.V. Makarov, A.E. Runnova, A.N. Pisarchik, A.E. Hramov, Coherence resonance in stimulated neuronal network, Chaos Solitons Fractals 106 (2018) 80–85.

[8] A.N. Pisarchik, V.A. Maksimenko, A.V. Andreev, N.S. Frolov, V.V. Makarov, M.O. Zhuravlev, A.E. Runnova, A.E. Hramov, Coherent resonance in the distributed cortical network during sensory information processing, Sci. Rep. 9 (2019) 18325.
[9] F. Moss, D. Pierson, D. O'Gorman, Stochastic resonance: Tutorial and update, Int. J. Bifurcation Chaos 4 (6) (1994) 1383–1397.
[10] L. Gammaitoni, P. Hänggi, P. Jung, F. Marchesoni, Stochastic resonance, Rev. Modern Phys. 70 (1998) 223–287.
[11] B. Andó, S. Graziani (Eds.), Stochastic Resonance: Theory and Applications, Kluwer Academic Publishers, Boston, 2000.
[12] C. Nicolis, Stochastic resonance in multistable systems: The role of dimensionality, Phys. Rev. E 86 (2012) 011133.
[13] M.D. McDonnell, D. Abbott, What is stochastic resonance? Definitions, misconceptions, debates, and its relevance to biology, PLoS Comput. Biol. 5 (5) (2009) e1000348.
[14] B. Lindner, J. García-Ojalvo, A. Neiman, L. Schimansky-Geiere, Effects of noise in excitable systems, Phys. Rep. 392 (2004) 321–424.
[15] W.-J. Rappel, A. Karma, Noise-induced coherence in neural networks, Phys. Rev. Lett. 77 (1996) 3256.
[16] S. Reinker, Y.-X. Li, R. Kuske, Noise-induced coherence and network oscillations in a reduced bursting model, Bull. Math. Biol. 68 (6) (2006) 1401–1427.
[17] H. Yu, L. Zhang, X. Guo, J. Wang, Y. Cao, J. Liu, Effect of inhibitory firing pattern on coherence resonance in random neural networks, Physica A 490 (2018) 1201–1210.
[18] C. Zhou, J. Kurths, B. Hu, Array-enhanced coherence resonance: Nontrivial effects of heterogeneity and spatial independence of noise, Phys. Rev. Lett. 87 (2001) 98101.
[19] R. Toral, C.R. Mirasso, J.D. Gunton, System size coherence resonance in coupled Fitzhugh–Nagumo models, Europhys. Lett. 61 (2003) 162–167.
[20] N. Burić, K. Todorović, N. Vasović, Influence of interaction delays on noise-induced coherence in excitable systems, Phys. Rev. E 82 (2018) 037201.
[21] M. Masoliver, N. Malik, E. Schöll, A. Zakharova, Coherence resonance in a network of FitzHugh–Nagumo systems: Interplay of noise, time-delay, and topology, Chaos 27 (2017) 101102.
[22] M.E. Yamakou, J. Jost, Coherent neural oscillations induced by weak synaptic noise, Nonlinear Dynam. (2018) http://dx.doi.org/10.1007/s11071-018-4311-1.
[23] M.E. Yamakou, J. Jost, Control of coherence resonance by self-induced stochastic resonance in a multiplex neural network, Phys. Rev. E 100 (2019) 022313.
[24] E. Baspinar, L. Schulen, S. Olmi, A. Zakharova, Coherence resonance in neuronal populations: Mean-field versus network model, Phys. Rev. E 103 (2021) 032308.
[25] M. Masoliver, C. Masoller, A. Zakharova, Control of coherence resonance in multiplex neural networks, Chaos Solitons Fractals 145 (2021) 110666.
[26] Q. Wang, M. Perc, Z. Duan, G. Chen, Synchronization transitions on scale-free neuronal networks due to finite information transmission delays, Phys. Rev. E 80 (2015) 026206.
[27] D.E. Postnov, O.V. Sosnovtseva, S.K. Han, T.G. Yim, Stochastic synchronization of coupled coherence resonance oscillators, Int. J. Bifurc. Chaos 10 (11) (2020) 2541–2550.
[28] Z.Q. Liu, H.M. Zhang, Y.Y. Li, C.C. Hua, H.G. Gu, W. Ren, Multiple spatial coherence resonance induced by the stochastic signal in neuronal networks near a saddle-node bifurcation, Physica A 389 (2010) 2642–2653.
[29] F. Bönsel, P. Krauss, C. Metzner, M.E. Yamakou, Control of noise-induced coherent oscillations in three-neuron motifs, Cogn. Neurodyn. 16 (2022) 941–960.
[30] Y. Gong, Y. Hao, X. Lin, L. Wang, X. Ma, Influence of time delay and channel blocking on multiple coherence resonance in Hodgkin–Huxley neuron networks, BioSystems 106 (2011) 76–81.
[31] X. Lin, Y.B. Gong, L. Wang, Multiple coherence resonance induced by time-periodic coupling strength in stochastic Hodgkin–Huxley neuron networks, Chaos 21 (2011) 043109.
[32] L. Wang, Y.B. Gong, X. Lin, B. Xu, Multiple coherence resonances by time-periodic coupling strength in scale-free networks of bursting neurons, Eur. Phys. J. B 85 (2012) 14.
[33] E. Yilmaz, M. Ozer, V. Baysal, M. Perc, Autapse-induced multiple coherence resonance in single neurons and neuronal networks, Sci. Rep. 6 (2016) 80.
[34] Q. Wang, Y. Gong, Multiple coherence resonance and synchronization transitions induced by autaptic delay in Newman–Watts neuron networks, Appl. Math. Mod. 40 (2016) 7147–7155.
[35] H. Xie, Y. Gong, Multiple coherence resonances and synchronization transitions by time delay in adaptive scale-free neuronal networks with spike-timing-dependent plasticity, Chaos Solitons Fractals 94 (2017) 80–85.
[36] H. Xie, Y. Gong, B. Wang, Spike-timing-dependent plasticity optimized coherence resonance and synchronization transitions by autaptic delay in adaptive scale-free neuronal networks, Chaos Solitons Fractals 108 (2018) 1–7.
[37] Y. Wu, Y. Gong, B. Xu, Periodic coupling strength-dependent multiple coherence resonance by time delay in Newman–Watts neuronal networks, BioSystems 114 (2018) 186–190.
[38] J.H. Kim, H.J. Lee, C.H. Min, K.J. Lee, Coherence resonance in bursting neural networks, Phys. Rev. E 92 (4) (2015) 042701.
[39] W.C. Stacey, D.M. Durand, Noise and coupling affect signal detection and bursting in a simulated physiological neural network, J. Neurophysiol. 88 (2002) 2598–2611.
[40] Y. Wang, D.T.W. Chik, Z.D. Wang, Coherence resonance and noise-induced synchronization in globally coupled Hodgkin–Huxley neurons, Phys. Rev. E 61 (1) (2000) 740–746.
[41] J. Pham, K. Pakdaman, J.-F. Vibert, Noise-induced coherent oscillations in randomly connected neural networks, Phys. Rev. E 58 (1998) 3610–3622.
[42] X. Sun, M. Perc, O. Lu, J. Kurths, Spatial coherence resonance on diffusive and small-world networks of Hodgkin–Huxley neurons, Chaos 18 (2008) 023102.
[43] M.E. Yamakou, E.M. Inack, Coherence resonance and stochastic synchronization in a small-world neural network: An interplay in the presence of spike-timing-dependent plasticity, 2022, http://dx.doi.org/10.48550/arXiv.2201.05436, arXiv:2201.05436[q-bio.NC].
[44] R. Jaimes-Reátegui, J.H. García-López, A. Gallegos, G. Huerta Cuellar, P. Chholak, A.N. Pisarchik, Deterministic coherence and anti-coherence resonances in networks of chaotic oscillators with frequency mismatch, Chaos Solitons Fractals 152 (2021) 111424.
[45] N. Semenova, A. Zakharova, Weak multiplexing induces coherence resonance, Chaos 28 (5) (2018) 051104.
[46] R. Tönjes, C.E. Fiore, T. Pereira, Coherence resonance in influencer networks, Nature Commun. 12 (1) (2021) 1–8.
[47] O.V. Ushakov, H.J. Wünsche, F. Henneberger, I.A. Khovanov, L. Schimansky-Geier, M. Zaks, Coherence resonance near a Hopf bifurcation, Phys. Rev. Lett. 95 (2005) 123903.
[48] T. Ohira, Y. Sato, Resonance with noise and delay, Phys. Rev. Lett. 82 (14) (1999) 2811–2814.
[49] P.M. Geffert, A. Zakharova, A. Andrea Vüllings, W. Just, E. Schöll, Modulating coherence resonance in non-excitable systems by time-delayed feedback, Eur. Phys. J. B 87 (12) (2014) 1–13.
[50] V. Semenov, A. Feoktistov, T. Vadivasova, E. Schöll, A. Zakharova, Time-delayed feedback control of coherence resonance. Experimental study, Chaos 25 (14) (2015) 033111.

[51] A. Zakharova, T. Vadivasova, V. Anishchenko, A. Koseska, J. J. Kurths, Stochastic bifurcations and coherencelike resonance in a self-sustained bistable noisy oscillator, Phys. Rev. E 81 (1) (2010) 011106.

[52] A. Zakharova, A. Feoktistov, T. Vadivasova, E. Schöll, Coherence resonance and stochastic synchronization in a nonlinear circuit near a subcritical Hopf bifurcation, Eur. Phys. J. Spec. Top. 222 (10) (2010) 2481–2495.

[53] I.Z. Kiss, J.L. Hudson, G.J. Escalera Santos, P. Parmananda, Experiments on coherence resonance: noisy precursors to Hopf bifurcations, Phys. Rev. E 67 (2) (2003) 035201.

[54] J.F. Martinez Avila, H.L.D.d.S. Cavalcante, J.R. Rios Leite, Experimental deterministic coherence resonance, Phys. Rev. Lett. 93 (14) (2004) 144101.

[55] M. Arizaleta Arteaga, M. Valencia, M. Sciamanna, H. Thienpont, M. López-Amo, K. Panajotov, Experimental evidence of coherence resonance in a time-delayed bistable system, Phys. Rev. Lett. 99 (2007) 023903.

[56] A.N. Pisarchik, R. Corbalán, Stochastic resonance in a chaotic laser, Phys. Rev. E 58 (1999) R2697–R2700.

[57] G. Giacomelli, M. Giudici, S. Balle, J.R. Tredicce, Experimental evidence of coherence resonance in an optical system, Phys. Rev. Lett. 84 (2000) 3298–3301.

[58] F. Arecchi, R. Meucci, Stochastic and coherence resonance in lasers: Homoclinic chaos and polarization bistability, Eur. Phys. J. B 69 (2009) 93–100.

[59] C.C. Otto, B.B. Lingnau, E.E. Schöll, K.K. Lüdge, Manipulating coherence resonance in a quantum dot semiconductor laser via electrical pumping, Opt. Express 22 (11) (2014) 13288–13307.

[60] H. Li, W. Qin, Dynamics and coherence resonance of a laminated piezoelectric beam for energy harvesting, Nonlin. Dyn. 81 (4) (2015) 1751–1757.

[61] L. Haitao, Q. Weiyang, L. Chunbo, D. Wangzheng, Z. Zhiyong, Dynamics and coherence resonance of tri-stable energy harvesting system, Smart Mater. Struct. 25 (1) (2015) 015001.

[62] G.Y. Zhong, H.F. Li, J.C. Li, D.C. Mei, N.S. Tang, C. Long, Coherence and anti-coherence resonance of corporation finance, Chaos Solitons Fractals 118 (2019) 376–385.

[63] G.Y. Zhong, F. He, J.C. Li, D.C. Mei, N.S. Tang, Coherence resonance-like and efficiency of financial market, Physica A 534 (2019) 122327.

[64] B. Dmitriev, Y. Zharkov, S. Sadovnikov, V. Skorokhodov, A. Stepanov, Coherent resonance in klystron oscillator at self-excitation threshold, Tech. Phys. Lett. 37 (11) (2011) 1082–1085.

[65] Y. Huang, H. Qin, W. Li, S. Lu, J. Dong, H. Grahn, Y. Zhang, Experimental evidence for coherence resonance in a noise-driven GaAs/AlAs superlattice, Europhys. Lett. 105 (4) (2014) 17005.

[66] Z. Shai, Z. Yin, H. Song, W. Liu, X. Li, J. Zhu, K. Biermann, L.L. Bonilla, H.T. Grahn, Y. Zhan, Fast detection of a weak signal by a stochastic resonance induced by a coherence resonance in an excitable GaAs/$Al_{0.45}Ga_{0.55}$As superlattice, Phys. Rev. Lett. 88 (2018) 086806.

[67] D.E. Postnov, S.K. Han, T.Y. Yim, O.V. Sosnovtseva, Experimental observation of coherence resonance in cascaded excitable systems, Phys. Rev. E 59 (4) (1999) R3791–R3794.

[68] A.K. Han, T.G. Yim, D.E. Postnov, O.V. Sosnovtseva, Interacting coherence resonance oscillators, Phys. Rev. Lett. 83 (9) (1999) 1771–1774.

[69] D.V. Setsinsky, D.É. Postnov, Noise-induced coherence in an excitable system with frequency-dependent feedback, Tech. Phys. Lett. 31 (4) (2005) 302–305.

[70] A.V. Feoktistov, V.S. Anishchenko, Coherence resonance and synchronization of stochastic self-sustained oscillations in hard excitation oscillator, Rus. J. Nonlin. Dyn. 8 (5) (2012) 897–911.

[71] L. Kabiraj, R. Steinert, A. Saurabh, C. Paschereit, Coherence resonance in a thermoacoustic system, Phys. Rev. E 92 (4) (2015) 042909.

[72] P. Shaw, D. Saha, S. Ghost, M. Janaki, A. Iyengar, Intrinsic noise induced coherence resonance in a glow discharge plasma, Chaos 25 (4) (2015) 043101.

[73] K. Miyakawa, H. Isikawa, Experimental observation of coherence resonance in an excitable chemical reaction system, Phys. Rev. E 66 (4) (2002) 046204.

[74] L.Q. Zhou, X. Jia, Q. Ouyang, Experimental and numerical studies of noise-induced coherent patterns in a subexcitable system, Phys. Rev. Lett. 88 (2002) 138301.

[75] V. Beato, I. Sendiña-Nadal, I. Gerdes, H. Engel, Coherence resonance in a chemical excitable system driven by coloured noise, Philos. Trans. R. Soc. A 366 (1864) (2008) 381–395.

[76] D. Simakov, J. Pérez-Mercader, Noise induced oscillations and coherence resonance in a generic model of the nonisothermal chemical oscillator, Philos. Trans. R. Soc. A 3 (2013) 2404.

[77] I.Z. Kiss, Y. Zhai, J.L. Hudson, C. Zhou, J. Kurths, Noise enhanced phase synchronization and coherence resonance in sets of chaotic oscillators with weak global coupling, Chaos 13 (1) (2003) 267–278.

[78] D. Wilkowski, J. Ringot, D. Hennequin, J.C. Garreau, Instabilities in a magneto-optical trap: Noise-induced dynamics in an atomic system, Phys. Rev. Lett. 85 (9) (2000) 1839–1842.

[79] C.Y. Lee, W. Choi, J.-H. Han, M.S. Strano, Coherence resonance in a single-walled carbon nanotube ion channel, Science 329 (2010) 1320–1324.

[80] Z. Zhou, W. Qin, P. Zhu, Harvesting acoustic energy by coherence resonance of a bi-stable piezoelectric harvester, Energy 126 (2017) 527–534.

[81] A.M. Lacasta, F. Sagués, J.M. Sancho, Coherence and anticoherence resonance tuned by noise, Phys. Rev. E 66 (2002) 045105(R).

[82] A. Pototsky, N. Janson, Excitable systems with noise and delay, with applications to control: Renewal theory approach, Phys. Rev. E 77 (2008) 031113.

[83] P. Zhu, D.C. Mei, Anti-coherence and coherence resonance induced by nonlinear time delay in autonomous stochastic system, Eur. Phys. J. B 87 (2014) 109.

[84] J.W. Shuai, S. Zeng, P. Jung, Coherence resonance: On the use and abuse of the Fano factor, Fluct. Noise Lett. 2 (3) (2002) L139–L146.

[85] Y. Horikawa, Coherence resonance with multiple peaks in a coupled FitzHugh–Nagumo model, Phys. Rev. E 64 (2001) 31905.

[86] B. Hu, C. Zhou, Phase synchronization in coupled nonidentical excitable systems and array-enhanced coherence resonance, Phys. Rev. E 61 (2) (2000) R1001–R1004.

[87] J.P. Baltanas, J.M. Casado, Noise-induced resonances in the Hindmarsh–Rose neuronal model, Phys. Rev. E 65 (2002) 41915.

[88] B. Lindner, Coherence and Stochastic Resonance in Nonlinear Dynamical Systems, Logos–Verlag, 2002.

[89] F. Marino, M. Giudici, S. Barland, S. Balle, Experimental evidence of stochastic resonance in an excitable optical system, Phys. Rev. Lett. 88 (4) (2002) 040601.

[90] A. Neiman, P. Saparin, L. Stone, Coherence resonance at noisy precursors of bifurcations in nonlinear dynamical systems, Phys. Rev. E 56 (1997) 270–273.

[91] S. Boccaletti, A.N. Pisarchik, C.I. del Genio, A. Amann, Synchronization: From Coupled Systems To Complex Networks, Cambridge University Press, Cambridge, 2018.

[92] R.V. Solé, S.J. Valverde, Information theory of complex networks: On evolution and architectural constraints, Lecture Notes in Phys. 650 (2004) 189–207.

[93] K. Anand, G. Bianconi, Entropy measures for networks: Toward an information theory of complex topologies, Phys. Rev. E 80 (2009) 045102(R).

[94] O.A. Rosso, C. Masoller, Detecting and quantifying temporal correlations in stochastic resonance via information theory measures, Eur. Phys. J. B 69 (1) (2009) 37–43.

[95] M. He, W. Xu, Z. Sun, L. Du, Characterization of stochastic resonance in a bistable system with poisson white noise using statistical complexity measures, Sci. Numer. Simul. 28 (1–3) (2015) 39–49.

[96] M. He, W. Xu, Z. Sun, W. Jia, Characterizing stochastic resonance in coupled bistable system with poisson white noises via statistical complexity measures, Nonlinear Dynam. 88 (2) (2017) 1163–1171.

[97] Z. Sun, P. Dang, W. Xu, Detecting and measuring stochastic resonance in fractional-order systems via statistical complexity, Chaos Solitons Fractals 125 (2019) 34–40.

[98] Y. Wua, Z. Suna, Y. Liua, W. Xu, Quantifying stochastic multiresonance in the FHN neuronal network model via statistical complexity measure, Chaos Solitons Fractals (2022).

[99] Y. Kuramoto, Chemical Oscillations, Waves, and Turbulence, Springer, Berlin, 1984.

[100] S.H. Strogatz, From Kuramoto to Crawford: exploring the onset of synchronization in populations of coupled oscillators, Physica D 143 (1–4) (2000) 1–20.

[101] J.G. Restrepo, E. Ott, B.R. Hunt, Onset of synchronization in large networks of coupled oscillators, Phys. Rev. E 71 (2005) 036151.

[102] A. Arenas, A. Díaz-Guilera, J. Kurths, Y. Moreno, C. Zhou, Synchronization in complex networks, Phys. Rep. 469 (3) (2008) 93–153.

[103] S. Boccaletti, V. Latora, Y. Moreno, M. Chavez, D.U. Hwang, Complex networks: Structure and dynamics, Phys. Rep. 424 (4–5) (2006) 175–308.

[104] T. Ichinomiya, Frequency synchronization in a random oscillator network, Phys. Rev. E 424 (4–5) (2004) 175–308.

[105] J. Gómez-Gardeñes, Y. Moreno, A. Arenas, Paths to synchronization on complex networks, Phys. Rev. Lett. 98 (2007) 034101.

[106] M. Schröder, M. Timme, D. Witthaut, A universal order parameter for synchrony in networks of limit cycle oscillators, Chaos 27 (2017) 073119.

[107] R. Gopal, V. Chandrasekar, A. Venkatesan, M. Lakshmanan, Observation and characterization of chimera states in coupled dynamical systems with nonlocal coupling, Phys. Rev. E 89 (2014) 052914.

[108] D. Golomb, D. Hansel, G. Mato, Robust universal approach to identify travelling chimeras and synchronized clusters in spiking networks, in: Handbook of Biological Physics, vol. 4, Elsevier, 2001, pp. 887–968.

[109] S.H. Abrams, Chimera states for coupled oscillators, Phys. Rev. Lett. 93 (17) (2004) 174102.

[110] O. Dogonasheva, D. Kasatkin, B. Gutkin, D. Zakharov, Robust universal approach to identify travelling chimeras and synchronized clusters in spiking networks, Chaos Solitons Fractals 153 (2021) 111541.

[111] M. García-Vellisca, A.N. Pisarchik, R. Jaimes-Reátegui, Experimental evidence of deterministic coherence resonance in coupled chaotic systems with frequency mismatch, Phys. Rev. E 94 (2016) 012218.

[112] M.T. Hütt, R. Neff, H. Busch, F. Kaiser, Method for detecting the signature of noise-induced structures in spatiotemporal data sets, Phys. Rev. E 66 (2002) 026117.

[113] H. Busch, F. Kaiser, Influence of spatiotemporally correlated noise on structure formation in excitable media, Phys. Rev. E 67 (2003) 041105.

[114] M. Rosenblum, A.S. Pikovsky, J. Kurths, Phase synchronization of chaotic oscillators, Phys. Rev. Lett. 76 (11) (1996) 1804–1807.

[115] O. Carrillo, M.A. Santos, J. García-Ojalvo, J.M. Sancho, Spatial coherence resonance near pattern-forming instabilities, Europhys. Lett. 65 (4) (2004) 452.

[116] M. Perc, Spatial coherence resonance in excitable media, Phys. Rev. E 72 (2005) 016207.

[117] M. Gosak, Cellular diversity promotes intercellular Ca^{2+} wave propagation, Biophys. Chem. 139 (2009) 53–56.

[118] D.R. Cox, Renewal Theory, Methuen, 1962.

[119] T. Wellens, V. V. Shatokhin, A. A. Buchleitner, Stochastic resonance, Rep. Progr. Phys. 67 (2004) 45–105.

[120] C.B. Muratov, E. Vanden-Eijnden, E. Weinan, Self-induced stochastic resonance in excitable systems, Physica D 210 (3–4) (2005) 227–240.

[121] C.W. Gardiner, Handbook of Stochastic Methods for Physics, Chemistry and the Natural Sciences, Springer–Verlag, Berlin, 1985.

[122] T.R. Bogatenko, V.V. Semenov, Coherence resonance in an excitable potential well, Phys. Lett. A 382 (1222) (2018) 2645–2649.

[123] R. FitzHugh, Impulses and physiological states in theoretical models of nerve membrane, Biophys. J. 1 (1961) 445–466.

[124] J. Nagumo, S. Arimoto, S. Yoshizawa, An active pulse transmission line simulating nerve axon, Proc. Inst. Radio Eng. 50 (1962) 2061–2070.

[125] A. Neiman, Coherence resonance, Scholarpedia 2 (2007) 1442, http://dx.doi.org/10.4249/scholarpedia.1442.

[126] J. Hindmarsh, R. Rose, A model of neuronal bursting using three coupled first order differential equations, Proc. R. Soc. Lond. B 221 (1222) (1984) 87–102.

[127] J.M. Casado, Noise-induced coherence in an excitable system, Phys. Lett. A 235 (5) (1997) 489–492.

[128] S.R. Massanés, C.J.P. Vicente, Nonadiabatic resonances in a noisy Fitzhugh–Nagumo neuron model, Phys. Rev. E 59 (4) (1999) 4490–4497.

[129] B. Lindner, L. Schimansky-Geier, Analytical approach to the stochastic FitzHugh–Nagumo system and coherence resonance, Phys. Rev. E 60 (6) (1999) 7270–7276.

[130] S. Lee, A. Neiman, S. Kim, Coherence resonance in a Hodgkin–Huxley neuron, Phys. Rev. E 57 (1998) 3292–3297.

[131] A. Torcini, S. Luccioli, T. Kreuz, Coherent response of the Hodgkin–Huxley neuron in the high-input regime, Neurocomputing 70 (2007) 1943–1948.

[132] R.C. Hilborn, R.J. Erwin, Coherence resonance in models of an excitable neuron with noise in both the fast and slow dynamics, Phys. Lett. A 322 (1–2) (2004) 19–24.

[133] B. Cao, R. Wang, H. Gu, Y. Li, Coherence resonance for neuronal bursting with spike undershoot, Cogn. Neurodyn. 15 (2008) 77–90.

[134] O. Kwon, H.T. Moon, Coherence resonance in small-world networks of excitable cells, Phys. Lett. A 298 (2002) 319–324.

[135] X. Sun, Q. Lu, J. Kurths, Correlated noise induced spatiotemporal coherence resonance in a square lattice network, Physica A 387 (2008) 6679–6685.

[136] Y. Jia, H. Gu, X. Ding, Inhibitory autapses enhance coherence resonance of a neuronal network, Commun. Nonlinear Sci. Numer. Simul. 95 (2021) 105643.

[137] R.C. Elson, A.I. Selverston, R. Huerta, N.F. Rulkov, M.I. Rabinovich, H.D.I. Abarbanel, Synchronous behavior of two coupled biological neurons, Phys. Rev. Lett. 81 (1998) 5692–5695.

[138] X. Lang, Q. Lu, J. Kurths, Phase synchronization in noise-driven bursting neurons, Phys. Rev. E 82 (2010) 021909.

[139] G. Deco, E.T. Rolls, R. Romo, Stochastic dynamics as a principle of brain function, Prog. Neurobiol. 88 (2009) 1–16.

[140] J.A.S. Kelso, Dynamic Patterns: The Self-Organization of Brain and Behavior, Cambridge, Bradford Books, 1997.

[141] A.N. Pisarchik, R. Jaimes-Retegui, C.D.A. Magalln-García, C.O. Castillo-Morales, Critical slowing down and noise-induced intermittency in bistable perception, Biol. Cyber. 108 (2014) 397–404.

[142] A.E. Runnova, A.E. Hramov, V.V. Grubov, A.A. Koronovskii, M.K. Kurovskaya, A.N. Pisarchik, Theoretical background and experimental measurements of human brain noise intensity in perception of ambiguous images, Chaos Solitons Fractals 93 (2016) 201–206.

[143] N.F. Rulkov, Modeling of spiking-bursting neural behavior using two-dimensional map, Phys. Rev. E 65 (2002) 041922.

[144] N.F. Rulkov, I. Timofeev, M. Bazhenov, Oscillations in large-scale cortical networks: Map-based model, J. Comp. Neurosci. 17 (2004) 203–223.

[145] F.A.S. Ferrari, R.L. Viana, F. Gomez, T. Lorimer, R. Stoop, Macroscopic bursting in physiological networks: Node or network property? New J. Phys. 17 (2015) 055024.

[146] K. Lehnertz, C.E. Elger, Can epileptic seizures be predicted? Evidence from nonlinear time series analysis of brain electrical activity, Phys. Rev. Lett. 80 (1998) 5019–5022.

[147] A.N. Pisarchik, V.V. Grubov, V.A. Maksimenko, A. Lüttjohann, N.S. Frolov, C. Marqués-Pascual, D. Gonzalez-Nieto, M.V. Khramova, A.E. Hramov, Extreme events in epileptic EEG of rodents after ischemic stroke, Eur. Phys. J. Spec. Top. 227 (2018) 921–932.
[148] N.S. Frolov, V.V. Grubov, V.A. Maksimenko, A.N. Pavlov, E. Sitnikova, A.N. Pisarchik, J. Kurths, A.E. Hramov, Statistical properties and predictability of extreme epileptic events, Sci. Rep. 9 (2019) 7243.
[149] L. Angelini, M. De Tommaso, M. Guido, K. Hu, P.C. Ivanov, D. Marinazzo, G. Nardulli, L. Nitti, M. Pelicorop, C. Pierro, S. Stramaglia, Steady-state visual evoked potentials and phase synchronization in migraine patients, Phys. Rev. Lett. 93 (2004) 038103.
[150] D. Hu, H. Cao, Stability and synchronization of coupled Rulkov map-based neurons with chemical synapses, Commun. Nonlinear Sci. Numer. Simul. 35 (2016) 105–122.
[151] A. Campos-Mejía, A.N. Pisarchik, D.A. Arroyo-Almanza, Noise-induced on–off intermittency in mutually coupled semiconductor lasers, Chaos Solitons Fractals 54 (2013) 96–100.
[152] G. Huerta-Cuellar, A.N. Pisarchik, A.V. Kir'yanov, O.Y. Barmenkov, J. del Valle Hernández, Prebifurcation noise amplification in a fiber laser, Chaos Solitons Fractals 54 (2013) 96–100.
[153] A. Pikovsky, A. Zaikin, M.A. de la Casa, System size resonance in coupled noisy systems and in the Ising model, Phys. Rev. Lett. 88 (2002) 013036.
[154] A.L. Hodgkin, A.F. Huxley, A quantitative description of membrane current and its application to conduction and excitation in nerve, J. Physiol. 117 (4) (1952) 500–544.
[155] E.V. Pankratova, A.V. Polovinkin, E. Mosekilde, Resonant activation in a stochastic Hodgkin–Huxley model: interplay between noise and suprathreshold driving effects, Eur. Phys. J. B 45 (2005) 391–397.
[156] R.F. Fox, Stochastic versions of the Hodgkin–Huxley equations, Biophys. J. 72 (1997) 2068–2074.
[157] J.A. White, J.T. Rubinstein, A.R. Kay, Channel noise in neurons, Trends Neurosci. 261 (2000) 83–92.
[158] J. Baladron, D. Fasoli, O. Faugeras, J. Touboul, Mean-field description and propagation of chaos in networks of Hodgkin–Huxley and FitzHugh–Nagumo neurons, J. Math. Neurosci. 2 (1) (2012) 1–50.
[159] M. Bossy, O. Faugeras, D. Talay, Clarification and complement to "Mean-field description and propagation of chaos in networks of Hodgkin–Huxley and FitzHugh–Nagumo neurons", J. Math. Neurosci. 5 (1) (2015) 1–23.
[160] M.E. Yamakou, T.D. Tran, L.H. Duc, J. Jost, The stochastic Fitzhugh–Nagumo neuron model in the excitable regime embeds a leaky integrate-and-fire model, J. Math. Biol. 79 (2) (2019) 509–532.
[161] N. Burić, D. Ranković, K. Todorović, N. Vasović, Mean field approximation for noisy delay coupled excitable neurons, Physica A 389 (19) (2010) 3956–3964.
[162] N. Etemadi, An elementary proof of the strong law of large numbers, Z. Wahrscheinlichkeitstheor. Verwandte Geb. 55 (1) (1981) 119–122.
[163] S. Olmi, R. Livi, A. Politi, A. Torcini, Collective oscillations in disordered neural networks, Phys. Rev. E 81 (4) (2010) 046119.
[164] S. Luccioli, S. Olmi, A. Politi, A. Torcini, Collective dynamics in sparse networks, Phys. Rev. Lett. 109 (13) (2012) 138103.
[165] X. Huang, W.C. Troy, Q. Yang, H. Ma, C.R. Laing, S.J. Schiff, J.Y. Wu, Spiral waves in disinhibited mammalian neocortex, J. Neurosci. 24 (2004) 9897–9902.
[166] J. Wu, X. Huang, C. Zhang, Propagating waves of activity in the neocortex: What they are, what they do, Neuroscientist 14 (2009) 487–502.
[167] X.Y. Huang, W. Xu, J. Liang, K. Takagaki, X. Gao, J.Y. Wu, Spiral wave dynamics in neocortex, Neuron 68 (2004) 978–990.
[168] A. Garfinkel, Y.H. Kim, O. Voroshilovsky, Z. Qu, J.R. Kil, M.H. Lee, H.S. Karagueuzian, J.N. Weiss, P.S. Chen, Preventing ventricular fibrillation by flattening cardiac restitution, Proc. Natl. Acad. Sci. USA 97 (2000) 6061–6066.
[169] N. Bursac, F. Aguel, L. Tung, Multiarm spirals in a two- dimensional cardiac substrate, Proc. Natl. Acad. Sci. USA 101 (2004) 15530.
[170] A.B. Neiman, D.F. Russell, Synchronization of noise-induced bursts in noncoupled sensory neurons, Phys. Rev. Lett. 88 (13) (2002) 138103.
[171] J.M. Davidenko, R. Pertsov, A.V. Salomonsz, W. Baxter, J. Jalife, Stationary and drifting spiral waves of excitation in isolated cardiac muscle, Nature 355 (1992) 349–351.
[172] J. Jalife, Ventricular fibrillation: mechanisms of initiation and maintenance, Ann. Rev. Physiol. 62 (1) (2000) 25–50.
[173] X. Sun, J. Kurths, Q. Wang, Spatiotemporal coherence resonance in a map lattice, Int. J. Bifurc. Chaos 19 (2) (2009) 737–743.
[174] Y. Zheng, Q. Lu, Q. Wang, Spatio-temporal coherence resonance and firing synchronization in a neural network: Noise and coupling effects, Internat. J. Modern Phys. C 20 (3) (2009) 469–478.
[175] Q.Y. Wang, Q.S. Lu, G.R. Chen, Spatio-temporal patterns in a square-lattice Hodgkin–Huxley neural network, Eur. Phys. J. B 54 (2006) 255–261.
[176] Y. Wu, J. Li, S. Liu, J. Pang, M. Du, P. Lin, Noise-induced spatiotemporal patterns in Hodgkin–Huxley neuronal network, Cogn. Neurodyn. 7 (2013) 431–440.
[177] O. Kwon, H. Jo, H. Moon, Effect of spatially correlated noise on coherence resonance in a network of excitable cells, Phys. Rev. E 72 (6) (2005) 066121.
[178] M. Perc, Spatial coherence resonance in neuronal media with discrete local dynamics, Chaos Solitons Fractals 31 (2007) 64–69.
[179] Y.Y. Li, H.M. Zhang, C.L. Wei, M.H. Yang, H.G. Gu, W. Ren, Stochastic signal induced multiple spatial coherence resonances and spiral waves in excitable media, Chin. Phys. Lett. 26 (2009) 030504.
[180] X.J. Sun, Q.S. Lu, Spatial coherence resonance induced by coloured noise and parameter diversity in a neuronal network, Chin. Phys. B 19 (4) (2010) 040504.
[181] Z. Tang, Z. Ang, Y.Y. Li, L. Xi, B. Jia, H.G. Gu, Spiral waves and multiple spatial coherence resonances induced by colored noise in neuronal network, Commun. Theor. Phys. 57 (1) (2012) 61–67.
[182] Y.Y. Li, B. Jia, H.G. Gu, S.C. An, Parameter diversity induced multiple spatial coherence resonances and spiral waves in neuronal network with and without noise, Commun. Theor. Phys. 57 (5) (2012) 817–824.
[183] H.G. Gu, B. Jia, Y.Y. Li, G.R. Chen, White noise-induced spiral waves and multiple spatial coherence resonances in a neuronal network with type I excitability, Physica A 392 (2013) 1361–1374.
[184] X.J. Sun, Q.S. Lu, Non-Gaussian colored noise optimized spatial coherence of a Hodgkin–Huxley neuronal network, Chin. Phys. Lett. 31 (2) (2014) 020502.
[185] M. Wang, R. Sun, W. Huang, Y. Tu, Internal noise induced pattern formation and spatial coherence resonance for calcium signals of diffusively coupled cells, Physica A 393 (2014) 519–526.
[186] M. Perc, Coherence resonance in a spatial prisoner's dilemma game, New J. Phys. 8 (2006) 22.
[187] V. Janonis, R.M. Balagula, I. Grigeliunis, P. Prystawko, I. Kaâlynas, Spatial coherence of hybrid surface plasmon-phonon-polaritons in shallow n-GaN surface-relief gratings, Opt. Express 29 (9) (2021) 13839.
[188] M. Gosak, M. Marhl, M. Perc, Spatial coherence resonance in excitable biochemical media induced by internal noise, Biophys. Chem. 128 (2007) 210–214.
[189] P.A. Brandão, J.P. Mendonça, S.B. Cavalcanti, Spatial coherence of hybrid surface plasmon-phonon-polaritons in shallow n-GaN surface-relief gratings, Opt. Lett. 46 (2021) 717–720.
[190] Y. Kuramoto, D. Battogtokh, Coexistence of coherence and incoherence in nonlocally coupled phase oscillators, Nonlinear Phenom. Complex Syst. 5 (4) (2002) 380–385.
[191] A.E. Motter, S.A. Myers, M. Anghel, T. Nishikawa, Spontaneous synchrony in powergrid networks, Nat. Phys. 9 (2013) 191–197.

[192] J.C. Gonzalez-Avella, M.G. Cosenza, M.S. Miguel, Localized coherence in two interacting populations of social agents, Physica A 399 (2014) 24–30.
[193] J. Hizanidis, N.E. Kouvaris, G. Zamora-Lopez, A. Díaz-Guilera, C. Antonopoulos, Chimera-like states in modular neural networks, Sci. Rep. 6 (2016) 19845.
[194] N.C. Rattenborg, C.J. Amlaner, S.L. Lima, Behavioral, neurophysiological and evolutionary perspectives on unihemispheric sleep, Neurosci. Biobehav. Rev. 24 (2000) 817–842.
[195] A. Rothkegel, K. Lehnertz, Irregular macroscopic dynamics due to chimera states in smallworld networks of pulse-coupled oscillators, New J. Phys. 16 (2014) 055006.
[196] N. Semenova, A. Zakharova, V. Anishchenko, E. Eckehard Schöll, Coherence-resonance chimeras in a network of excitable elements, Phys. Rev. Lett. 117 (1) (2016) 014102.
[197] I. Omelchenko, O.E. Omel'chenko, P. Hövel, E. Schöll, When nonlocal coupling between oscillators becomes stronger: patched synchrony or multichimera states, Phys. Rev. Lett. 110 (2013) 224101.
[198] I. Omelchenko, Y. Maistrenko, P. Hövel, E. Schöll, Loss of coherence in dynamical networks: spatial chaos and chimera states, Phys. Rev. Lett. 106 (2011) 234102.
[199] A. Zakharova, N. Semenova, V.S. Anishchenko, E. Schöll, Noise-induced chimera states in a neural network, in: P. Gurevich, J. Hell, B. Sandstede, A. Scheel (Eds.), Springer Proc. Math. Stat., 205, Springer, Cham, 2017, pp. 44–62.
[200] Z. Wang, Y. Li, Y. Xu, T. Kapitaniak, J. Kurths, Coherence-resonance chimeras in coupled HR neurons with alpha-stable Lévy noise, J. Stat. Mech. 2022 (2022) 053501.
[201] D.J. Watts, S.H. Strogatz, Collective dynamics of 'small-world' networks, Nature 393 (1998) 440–442.
[202] F. Varela, J.-P. Lachaux, E. Rodriguez, J. Martinerie, The brainweb: phase synchronization and large-scale integration, Nat. Rev. Neurosci. 2 (2001) 229–239.
[203] J.M. Shine, P.G. Bissett, P.T. Bell, O. Koyejo, J.H. Balsters, K.J. Gorgolewski, C.A. Moodie, R.A. Poldrack, The dynamics of functional brain networks: integrated network states during cognitive task performance, Neuron 92 (2) (2016) 544–554.
[204] B.J. Baars, In the theatre of consciousness. global workspace theory, a rigorous scientific theory of consciousness, J. Conscious. Stud. 4 (1997) 292–309.
[205] S. Dehaene, M. Kerszberg, J.-P. Changeux, A neuronal model of a global workspace in effortful cognitive tasks, Proc. Natl. Acad. Sci. 95 (1998) 14529–14534.
[206] P. Fries, A mechanism for cognitive dynamics: Neuronal communication through neuronal coherence, Trends Cogn. Sci. 9 (2005) 474–480.
[207] G. Deco, M.L. Kringelbach, Metastability and coherence: Extending the communication through coherence hypothesis using a whole-brain computational perspective, Trends Neurosci. 39 (3) (2016) 125–135.
[208] M. Carandini, D.J. Heeger, J.A. Movshon, Linearity and normalization in simple cells of the macaque primary visual cortex, J. Neurosci. 17 (1997) 8621–8644.
[209] D.A. Ruff, C. Xue, L.E. Kramer, F. Baqai, M.R. Cohen, Low rank mechanisms underlying flexible visual representations, BioRxiv 730978 (2019).
[210] D. Tolhurst, J.A. Movshon, I. Thompson, The dependence of response amplitude and variance of cat visual cortical neurones on stimulus contrast, Exper. Brain Res. 41 (1981) 414–419.
[211] K. Sekar, W.M. Findley, R.R. Llinás, Evidence for an all-or-none perceptual response: single-trial analyses of magnetoencephalography signals indicate an abrupt transition between visual perception and its absence, Neurosci. 206 (2012) 167–182.
[212] A.A. Faisal, L.P. Selen, D.M. Wolpert, Noise in the nervous system, Nat. Rev. Neurosci. 9 (4) (2008) 292–303.
[213] R. Cremer, E.J. Zeef, What kind of noise increases with age? J. Gerontol. 42 (5) (1987) 515–518.
[214] K.J. Miller, Broadband spectral change: evidence for a macroscale correlate of population firing rate? J. Neurosci. 30 (19) (2010) 6477–6479.
[215] B.J. He, Scale-free brain activity: past, present, and future, Trends Cogn. Sci. 18 (9) (2014) 480–487.
[216] S.C. Li, U. Lindenberger, S. Sikström, Aging cognition: from neuromodulation to representation, Trends Cogn. Sci. 5 (11) (2012) 479–486.
[217] D. Serletis, O.C. Zalay, T.A. Valiante, B.L. Bardakjian, P.L. Carlen, Complexity in neuronal noise depends on network interconnectivity, Ann. Biomed. Eng. 39 (6) (2011) 1768–1778.
[218] S.L. Hong, G.V. Rebec, A new perspective on behavioral inconsistency and neural noise in aging: compensatory speeding of neural communication, Front. Aging Neurosci. 4 (2012) 27.
[219] A.N. Pisarchik, P. Chholak, A.E. Hramov, Brain noise estimation from MEG response to flickering visual stimulation, Chaos Solit. Fractals X 1 (2019) 100005.
[220] G. Huerta-Cuéllar, E. Jiménez-López, E. Campos-Cantón, A.N. Pisarchik, An approach to generate deterministic Brownian motion, Commun. Nonlinear Sci. Numer. Simul. 19 (2014) 2740–2746.
[221] A.N. Pisarchik, G. Huerta-Cuéllar, C.W. Kulp, Statistical analysis of symbolic dynamics in weakly coupled chaotic oscillators, Commun. Nonlinear Sci. Numer. Simul. 62 (2018) 134–145.
[222] F.J. Martín Pasquín, A.N. Pisarchik, Brownian behavior in coupled chaotic oscillators, Mathematics 9 (2021) 2503.
[223] A.R. Muotri, F.H. Gage, Generation of neuronal variability and complexity, Nature 441 (7097) (2006) 1087–1093.
[224] A.A. Faisal, L.P.J. Selen, D.M. Wolpert, Noise in the nervous system, Nat. Rev. Neurosci. 9 (4) (2008) 292–303.
[225] R. Madigan, D. Williams, Maximum-likelihood psychometric procedures in two-alternative forced-choice: Evaluation and recommendations, Percept. Psychophys. 42 (3) (1987) 240–249.
[226] W.J. Park, K.B. Schauder, R. Zhang, L. Bennetto, D. Tadin, High internal noise and poor external noise filtering characterize perception in autism spectrum disorder, Sci. Rep. 7 (1) (2017) 1–12.
[227] J.H. Reynolds, D.J. Heeger, The normalization model of attention, Neuron 61 (2) (2009) 168–185.
[228] C. Olman, Introduction To Sensation and Perception, University of Minnesota Libraries Publishing, 2022.
[229] T. Poston, I. Stewart, Catastrophe Theory and Its Applications, Pitman, 1978.
[230] A.N. Pisarchik, A.E. Hramov, Multistability in Physical and Living Systems: Characterization and Applications, Springer Nature, 2022.
[231] N. Hô, A. Destexhe, Synaptic background activity enhances the responsiveness of neocortical pyramidal neurons, J. Neurophysiol. 84 (3) (2000) 1488–1496.
[232] N.G. Stocks, R. Mannella, Generic noise-enhanced coding in neuronal arrays, Phys. Rev. E 64 (3) (2001) 030902.
[233] H. Sasaki, M. Todorokihara, T. Ishida, J. Miyachi, T. Kitamura, R. Aoki, Effect of noise on the contrast detection threshold in visual perception, Neurosci. Lett. 408 (2) (2006) 94–97.
[234] F.G. Zeng, Q.J. Fu, R. Morse, Human hearing enhanced by noise, Brain Res. 869 (1–2) (2000) 251–255.
[235] K. Kitajo, D. Nozaki, L.M. Ward, Y. Yamamoto, Behavioral stochastic resonance within the human brain, Phys. Rev. Lett. 90 (21) (2003) 218103.
[236] T. Aihara, K. Kitajo, D. Nozaki, Y. Yamamoto, How does stochastic resonance work within the human brain?–Psychophysics of internal and external noise, Chem. Phys. 375 (2–3) (2010) 616–624.
[237] T. Aihara, K. Kitajo, D. Nozaki, Y. Yamamoto, Internal noise determines external stochastic resonance in visual perception, Vis. Res. 48 (14) (2008) 1569–1573.
[238] L.M. Ward, Psychophysics of stochastic resonance, Fluct. Noise Lett. 4 (1) (2004) L11–L21.

[239] J. Milton, A. Solodkin, P. Hluštík, S.L. Small, The mind of expert motor performance is cool and focused, Neuroimage 35 (2) (2007) 804–813.

[240] V.A. Maksimenko, N.S. Frolov, A.E. Hramov, A.E. Runnova, V.V. Grubov, J. Kurths, A.N. Pisarchik, Neural interactions in a spatially-distributed cortical network during perceptual decision-making, Front. Behav. Neurosci. 13 (2019) 220.

[241] D. Ress, D.J. Heeger, Neuronal correlates of perception in early visual cortex, Nature Neurosci. 6 (4) (2003) 414–420.

[242] R. Srebro, P. Malladi, Stochastic resonance of the visually evoked potential, Phys. Rev. E 59 (3) (1999) 2566.

[243] C.M. Michel, M.M. Murray, G. Lantz, S. Gonzalez, L. Spinelli, R. Grave de Peralta, EEG source imaging, Clin. Neurophysiol. 115 (10) (2004) 2195–2222.

[244] O. Van der Groen, M.F. Tang, N. Wenderoth, J.B. Mattingley, Stochastic resonance enhances the rate of evidence accumulation during combined brain stimulation and perceptual decision-making, PLoS Comput. Biol. 14 (7) (2018) e1006301.

[245] N.S. Frolov, V.V. Grubov, V.A. Maksimenko, A. Lüttjohann, V.V. Makarov, A.N. Pavlov, E. Sitnikova, A.N. Pisarchik, J. Kurths, A.E. Hramov, Statistical properties and predictability of extreme epileptic events, Sci. Rep. 9 (1) (2019) 1–8.

[246] O.E. Karpov, V.V. Grubov, V.A. Maksimenko, N. Utaschev, V.E. Semerikov, D.A. Andrikov, A.E. Hramov, Noise amplification precedes extreme epileptic events on human EEG, Phys. Rev. E 103 (2) (2021) 022310.

[247] J. Gross, F. Schmitz, I. Schnitzler, K. Kessler, K. Shapiro, B. Hommel, A. Schnitzler, Modulation of long-range neural synchrony reflects temporal limitations of visual attention in humans, Proc. Natl. Acad. Sci. USA 101 (2004) 13050–13055.

[248] A.G. Guggisberg, S.M. Honma, A.M. Findlay, S.S. Dalal, H.E. Kirsch, M.S. Berger, S.S. Nagarajan, Mapping functional connectivity in patients with brain lesions, Ann. Neurol. 63 (2008) 193–203.

[249] P. Belardinelli, L. Ciancetta, M. Staudt, V. Pizzella, A. Londei, N. Birbaumer, G.L. Romani, C. Braun, Cerebro-muscular and cerebro-cerebral coherence in patients with pre- and perinatally acquired unilateral brain lesions, NeuroImage 37 (2007) 1301–1314.

[250] F. de Pasquale, S. Della Penna, A.Z. Snyder, C. Lewis, D. Mantini, L. Marzetti, P. Belardinelli, L. Ciancetta, V. Pizzella, G. Romani, et al., Temporal dynamics of spontaneous MEG activity in brain networks, Proc. Natl. Acad. Sci. USA 107 (2010) 6040–6045.

[251] L.B.N. Hinkley, S. Vinogradov, A.G. Guggisberg, M. Fisher, A.M. Findlay, S.S. Nagarajan, Clinical symptoms and alpha band resting-state functional connectivity imaging in patients with schizophrenia: implications for novel approaches to treatment, Biol. Psychiatry 70 (2011) 1134–1142.

[252] J.S. Kim, K.S. Shin, W.H. Jung, S.N. Kim, J.S. Kwon, C.K. Chung, Power spectral aspects of the default mode network in schizophrenia: An MEG study, BMC Neurosci. 15 (2014) 104.

[253] S.M. Bowyer, K. Gjini, X. Zhu, L. Kim, J.E. Moran, S.U. Rizvi, N.T. Gumenyuk, N. Tepley, N.N. Boutros, Potential biomarkers of schizophrenia from MEG resting-state functional connectivity networks: Preliminary data, J. Behav. Brain Sci. 5 (2015) 1.

[254] N.N. Boutros, M.P. Galloway, S. Ghosh, K. Gjini, S.M. Bowyer, Abnormal coherence imaging in panic disorder: A magnetoencephalography investigation, Neuroreport 24 (2013) 487–491.

[255] P. Chholak, G. Niso, V.A. Maksimenko, S.A. Kurkin, N.S. Frolov, E.N. Pitsik, A.E. Hramov, A.N. Pisarchik, Visual and kinesthetic modes affect motor imagery classification in untrained subjects, Sci. Rep. 9 (2019) 9838.

[256] P. Chholak, A.N. Pisarchik, S.A. Kurkin, V.A. Maksimenko, A.E. Hramov, Neuronal pathway and signal modulation for motor communication, Cybern. Phys. 24 (2019) 106–113.

[257] K.J. Friston, C.D. Frith, P.F. Liddle, R.S. Frackowiak, Functional connectivity: The principal-component analysis of large (PET) data sets, J. Cereb. Blood Flow Metab. 13 (1993) 5–14.

[258] V. Sakkalis, Review of advanced techniques for the estimation of brain connectivity measured with EEG/MEG, J. Neurosci. Methods 41 (2011) 1110–1117.

[259] R.E. Greenblatt, M.E. Pflieger, A.E. Ossadtchi, Connectivity measures applied to human brain electrophysiological data, J. Neurosci. Methods 207 (2012) 1–16.

[260] A.E. Hramov, N.S. Frolov, V.A. Maksimenko, S.A. Kurkin, V.B. Kazantsev, A.N. Pisarchik, Functional networks of the brain: From connectivity restoration to dynamic integration, Phys. Usp. 2020 (2020) 63.

[261] D. Le Bihan, J.F. Mangin, C. Poupon, C.A. Clark, S. Pappata, N. Molko, H. Chabriat, Diffusion tensor imaging: Concepts and applications, J. Magn. Reson. Imaging JMRI 13 (2001) 534–546.

[262] V.J. Wedeen, R.P. Wang, J.D. Schmahmann, T. Benner, W.Y.I. Tseng, G. Dai, D.N. Pandya, P. Hagmann, H. D'Arceuil, A.J. de Crespigny, Diffusion spectrum magnetic resonance imaging (DSI) tractography of crossing fibers, NeuroImage 41 (2008) 1267–1277.

[263] V.L. Towle, J.D. Hunter, J.C. Edgar, S.A. Chkhenkeli, M.C. Castelle, D. Frim, Frequency domain analysis of human subdural recordings, J. Clin. Neurophysiol. 24 (2007) 205–213.

[264] B. Horwitz, The elusive concept of brain connectivity, NeuroImage 19 (2003) 466–470.

[265] J. Cabral, M.L. Kringelbach, G. Deco, Exploring the network dynamics underlying brain activity during rest, Prog. Neurobiol. 114 (2014) 102–131.

[266] S.M. Bowyer, Coherence a measure of the brain networks: Past and present, Neuropsychiatr. Electrophysiol. 2 (2016) 1.

[267] N. Frolov, V. Maksimenko, A. Lüttjohann, A. Koronovskii, A. Hramov, Feed-forward artificial neural network provides data-driven inference of functional connectivity, Chaos 29 (2019) 091101.

[268] A.N. Pisarchik, P. Chholak, V.A. Maksimenko, A.E. Hramov, Voluntary and involuntary attention in bistable visual perception: A MEG study, Front. Hum. Neurosci. 14 (2020) 555.

[269] C.C. French, J.G. Beaumont, A critical review of EEG coherence studies of hemisphere function, Int. J. Psychophysiol. Off. J. Int. Organ. Psychophysiol. 1 (1984) 241–254.

[270] K. Hoechstetter, H. Bornfleth, D. Weckesser, N. Ille, P. Berg, M. Scherg, BESA source coherence: A new method to study cortical oscillatory coupling, Brain Topogr. 16 (2004) 233–238.

[271] P. An, M. Va, A. Av, F. Ns, M. Vv, Z. Mo, R. Ae, H. Ae, Coherent resonance in the distributed cortical network during sensory information processing, Sci. Rep. 9 (2019) 18325.

[272] P. Chholak, A.E. Hramov, A.N. Pisarchik, An advanced perception model combining brain noise and adaptation, Nonlinear Dynam. 100 (2020) 3695–3709.

[273] P. Chholak, S.A. Kurkin, A.E. Hramov, A.N. Pisarchik, Event-related coherence in visual cortex and brain noise: An MEG study, Appl. Sci. 11 (1) (2021) 375.

[274] B.N. Cuffin, D. Cohen, Magnetic fields of a dipole in special volume conductor shapes, IEEE Trans. Biomed. Eng. 24 (1977) 372–381.

[275] M.X. Huang, J.C. Mosher, R.M. Leahy, A sensor-weighted overlapping-sphere head model and exhaustive head model comparison for MEG, Phys. Med. Biol. 44 (1999) 432–440.

[276] G. Nolte, The magnetic lead field theorem in the quasi-static approximation and its use for magnetoencephalography forward calculation in realistic volume conductors, Phys. Med. Biol. 48 (2003) 3637–3652.

[277] F. Darvas, D. Pantazis, E. Kucukaltun-Yildirim, R. Leahy, E. Kucukaltun-Yildirim, R.M. Leahy, Mapping human brain function with MEG and EEG: Methods and validation, NeuroImage 23 (2004) S289–S299.

[278] M. Scherg, Fundamentals of dipole source analysis, Adv. Audiol. 6 (1990) 40–46.

[279] B.D. Van Veen, W. Van Drongelen, M. Yuchtman, A. Suzuki, Localization of brain electrical activity via linearly constrained minimum variance spatial filtering, IEEE Trans. Biomed. Eng. 44 (1997) 867–880.

[280] J. Gross, J. Kujala, M. Hämäläinen, L. Timmermann, A. Schnitzler, R. Salmelin, Dynamic imaging of coherent sources: Studying neural interactions in the human brain, Proc. Natl. Acad. Sci. USA 98 (2001) 694–699.

[281] M.S. Hämäläinen, R.J. Ilmoniemi, Interpreting magnetic fields of the brain: Minimum norm estimates, Med. Biol. Eng. Comput. 32 (1994) 35–42.

[282] R. Grech, T. Cassar, J. Muscat, K.P. Camilleri, S.G. Fabri, M. Zervakis, P. Xanthopoulos, V. Sakkalis, B. Vanrumste, Review on solving the inverse problem in EEG source analysis, J. Neuroeng. Rehabil. 5 (2008) 25.

[283] R.D. Pascual-Marqui, Standardized low-resolution brain electromagnetic tomography (sLORETA): Technical details, Methods Find. Exp. Clin. Pharmacol. 24 (2002) 5–12.

[284] C. Mulert, L. Jäger, R. Schmitt, P. Bussfeld, O. Pogarell, H.J. Möller, G. Juckel, U. Hegerl, Integration of fMRI and simultaneous EEG: towards a comprehensive understanding of localization and time-course of brain activity in target detection, NeuroImage 22 (2004) 83–94.

[285] D. Zumsteg, A. Friedman, H.G. Wieser, R.A. Wennberg, Propagation of interictal discharges in temporal lobe epilepsy: Correlation of spatiotemporal mapping with intracranial foramen ovale electrode recordings, Clin. Neurophysiol. 117 (2006) 2615–2626.

[286] R.D. Pascual-Marqui, D. Lehmann, M. Koukkou, K. Kochi, P. Anderer, B. Saletu, H. Tanaka, K. Hirata, E.R. John, L. Prichep, et al., Assessing interactions in the brain with exact low-resolution electromagnetic tomography, Philos. Trans. R. Soc. A 369 (2011) 3768–3784.

[287] M.A. Lopes, L. Junges, L. Tait, J.R. Terry, E. Abela, M.P. Richardson, M. Goodfellow, Computational modelling in source space from scalp EEG to inform presurgical evaluation of epilepsy, Clin. Neurophysiol. 131 (2020) 225–234.

[288] R.D. Pascual-Marqui, M. Esslen, K. Kochi, D. Lehmann, Functional imaging with low-resolution brain electromagnetic tomography (LORETA): A review, Methods Find. Exp. Clin. Pharmacol. 24 (2002) 91–95.

[289] A. Longtin, A. Bulsara, F. Moss, Time-interval sequences in bistable systems and the noise-induced transmission of information by sensory neurons, Phys. Rev. Lett. 67 (1991) 656–659.

[290] A. Zarkou, S.C.K. Lee, L.A. Prosser, S. Hwang, J. Jeka, Stochastic resonance stimulation improves balance in children with cerebral palsy: A case control study, J. Neuroeng. Rehabil. 15 (2018) 115.

[291] M.D. McDonnell, L.M. Ward, The benefits of noise in neural systems: bridging theory and experiment, Nat. Rev. Neurosci. 12 (7) (2011) 415–425.

[292] E. Simonotto, M. Riani, C. Seife, M. Roberts, J. Twitty, F. Moss, Visual perception of stochastic resonance, Phys. Rev. Lett. 78 (6) (1997) 1186.

[293] N. Wax, Selected Papers on Noise and Stochastic Processes, Courier Dover Publications, 1954.

[294] P. Jung, Stochastic resonance and optimal design of threshold detectors, Phys. Lett. A 207 (1–2) (1995) 93–104.

[295] P. Jung, Threshold devices: Fractal noise and neural talk, Phys. Rev. E 50 (4) (1994) 2513.

[296] E. Itzcovich, M. Riani, W.G. Sannita, Stochastic resonance improves vision in the severely impaired, Sci. Rep. 7 (2017) 12840.

[297] V.S. Anishchenko, A.B. Neiman, F. Moss, L. Shimansky-Geier, Stochastic resonance: noise-enhanced order, Phys.-Usp. 42 (1) (1999) 7.

[298] J.J. Collins, T.T. Imhoff, P. Grigg, Noise-enhanced information transmission in rat SA1 cutaneous mechanoreceptors via aperiodic stochastic resonance, J. Neurophysiol. 76 (1996) 642–645.

[299] J.J. Collins, T.T. Imhoff, P. Grigg, Noise-enhanced tactile sensation, Nature 383 (6603) (1996) 770.

[300] K.A. Richardson, T.T. Imhoff, P. Grigg, J.J. Collins, Using electrical noise to enhance the ability of humans to detect subthreshold mechanical cutaneous stimuli, Chaos 8 (3) (1998) 599–603.

[301] N.T. Dhruv, J.B. Niemi, J.D. Harry, L.A. Lipsitz, J.J. Collins, Enhancing tactile sensation in older adults with electrical noise stimulation, Neuroreport 13 (5) (2002) 115.

[302] J.J. Collins, A.A. Priplata, D.C. Gravelle, J. Nieme, J. Harry, L.A. Lipsitz, Noise-enhanced human sensorimotor function, IEEE Eng. Med. Biol. Mag. 22 (2) (2003) 76–83.

[303] L. Khaodhiar, J.B. Niemi, R. Earnest, C. Lima, J.D. Harry, A. Veves, Enhancing sensation in diabetic neuropathic foot with mechanical noise, Diabetes Care 26 (12) (2003) 3280–3283.

[304] A.A. Priplata, J.B. Niemi, J.D. Harry, L.A. Lipsitz, J.J. Collins, Vibrating insoles and balance control in elderly people, Lancet 362 (9390) (2003) 1123–1124.

[305] A. Priplata, J. Niemi, M. Salen, J. Harry, L.A. Lipsitz, J.J. Collins, Noise-enhanced human balance control, Phys. Rev. Lett. 89 (23) (2002) 238101.

[306] J. Collins, C. De Luca, A. Burrows, L. Lipsitz, Age-related changes in open-loop and closed-loop postural control mechanisms, Exp. Brain Res. 104 (3) (1995) 480–492.

[307] I. Hidaka, D. Nozaki, Y. Yamamoto, Functional stochastic resonance in the human brain: Noise induced sensitization of baroreflex system, Phys. Rev. Lett. 85 (17) (2000) 3740–3743.

[308] N. Huidobro, B. De la Torre-Valdovinos, A. Mendez, M. Treviño, O. Oscar Arias-Carrion, F. Chavez, R. Gutierrez, E. Manjarrez, Optogenetic noise-photostimulation on the brain increases somatosensory spike firing responses, Neurosci. Lett. 664 (2018) 51–57.

[309] O. Van der Groen, N. Wenderoth, Transcranial random noise stimulation of visual cortex: stochastic resonance enhances central mechanisms of perception, J. Neurosci. 36 (2016) 5289–5298.

[310] A. Constantin, A. Danyluk, a Brain-Computer Interface for the Classification of Motor Imagery, Williams College, 2007.

[311] V.A. Maksimenko, S.A. Kurkin, E.N. Pitsik, V.Y. Musatov, A.E. Runnova, T.Y. Efremova, A.E. Hramov, A.N. Pisarchik, Artificial neural network classification of motor-related EEG: An increase in classification accuracy by reducing signal complexity, Complexity 2018 (2018) 9385947.

[312] A.E. Hramov, V.A. Maksimenko, A.N. Pisarchik, Physical principles of brain-computer interfaces and their applications for rehabilitation, robotics and control of human brain states, Phys. Rep. 918 (2021) 1–133.

[313] F. Lotte, M. Congedo, A. Lécuyer, F. Lamarche, B. Arnaldi, A review of classification algorithms for EEG-based brain-computer interfaces, J. Neural Eng. 4 (2) (2007) R1.

[314] J. Long, J. Wang, T. Yu, An efficient framework for EEG analysis with application to hybrid brain computer interfaces based on motor imagery and P300, Comput. Intell. Neurosci. 2017 (2017) 1–6.

[315] R.A. Ramadan, A.V. Vasilakos, Brain computer interface: Control signals review, Neurocomputing 223 (2017) 26–44.

[316] A. Rakotomamonjy, V. Guigue, BCI competition III: dataset II- ensemble of SVMs for BCI P300 speller, IEEE Trans. Biomed. Eng. 55 (2007) 1147–1154.

[317] H. Cecotti, A. Graser, Convolutional neural networks for P300 detection with application to brain-computer interfaces, IEEE Trans. Pattern Anal. Mach. Intell. 33 (2011) 433–445.

[318] R. Sampanna, S. Mitaim, Noise benefits in the array of brain-computer interface classification systems, Inform. Med. Unlocked 12 (2018) 88–97.

[319] J. Xie, G. Xu, J. Wang, S. Zhang, F. Zhang, Y. Li, Addition of visual noise boosts evoked potential-based brain-computer interface, Sci. Rep. 4 (2014) 49534.

[320] J. Xie, G. Xu, X. Zhao, M. Li, J. Wang, C. Han, et al., Enhanced plasticity of human evoked potentials by visual noise during the intervention of steady-state stimulation based brain-computer interface, Front. Neurorobot. 12 (2018) 82.

[321] J. Xie, G. Xu, A. Luo, M. Li, X. Zhao, C. Han, et al., The role of visual noise in influencing mental load and fatigue in a steady-state motion visual evoked potential-based brain-computer interface, Sensors 17 (2017) 1873.

[322] S. Zhang, X. Gao, The effect of visual stimuli noise and fatigue on steady-state visual evoked potentials, J. Neural. Eng. 16 (2019) 056023.

[323] Z. Işcan, V.V. Nikulin, Steady state visual evoked potential (SSVEP) based brain-computer interface (BCI) performance under different perturbations, PLoS ONE 13 (1) (2018) e0191673.
[324] A.N. Pisarchik, U. Feudel, Control of multistability, Phys. Rep. 540 (2014) 167–218.
[325] J. Ma, Q. Gao, Two types of coherence resonance in an intracellular calcium oscillation system, Chem. Phys. 495 (2017) 29–34.
[326] X. Song, H. Wang, Y. Chen, Coherence resonance in an autaptic Hodgkin–Huxley neuron with time delay, Nonlinear Dynam. 94 (1) (2018) 141–150.
[327] A.N. Pisarchik, R. Jaimes-Reátegui, Deterministic coherence resonance in coupled chaotic oscillators with frequency mismatch, Phys. Rev. E 92 (2015) 141–150.
[328] A.N. Pisarchik, I. Bashkirtseva, L. Ryashko, Chaos can imply periodicity in coupled oscillators, Europhys. Lett. 117 (4) (2017) 40005.
[329] L.S. Tsimring, A. Pikovsky, Noise-induced dynamics in bistable systems with delay, Phys. Rev. Lett. 87 (2001) 250602.
[330] B. Lindner, L. Schimansky-Geier, Coherence and stochastic resonance in a two-state system, Phys. Rev. E 61 (6) (2000) 6103–6110.
[331] J.D. Pelletier, Coherence resonance in ice ages, Geograph. Res. 108 (D20) (2003) 4645.
[332] Y. Jin, H. Hu, Coherence and stochastic resonance in a delayed bistable system, Physica A 382 (2007) 423–429.
[333] L. Haitao, Q. Weiyang, L. Chunbo, D. Wangzheng, Z. Zhiyong, Dynamics and coherence resonance of tri-stable energy harvesting system, Smart Mater. Struct. 25 (1) (2016) 015001.
[334] P. Xu, Y. Jin, Coherence and stochastic resonance in a second-order asymmetric tri-stable system with memory effects, Chaos Solitons Fractals 138 (14) (2020) 109857.
[335] Y. Kato, H. Nakao, Quantum coherence resonance, New J. Phys. 23 (2021) 043018.
[336] S. Walter, A. Nunnenkamp, C. Bruder, Quantum synchronization of a driven self-sustained oscillator, Phys. Rev. Lett. 112 (2014) 094102.
[337] Y. Kato, N. Yamamoto, H. Nakao, Semiclassical phase reduction theory for quantum synchronization, Phys. Rev. Rev. 1 (2019) 033012.